Numerical Investigation of Long-term Instability in Solution Growth of SiC Crystal

Yifan Dang

Supervisor: Prof. Toru Ujihara

Department of Materials Process Engineering,
Nagoya University

This dissertation is submitted for the degree of
Doctor of Engineering

Graduate School of Engineering July 2022

Abstract

SiC grown by solution growth method has proven superior in crystal quality, but the mass production is still hindered by relatively low yield. The accurate description, understanding, and control of the unsteady phenomena in the growth system are essential to achieving a longer stable growth time and larger crystal thickness. This dissertation aims to numerically investigate the instabilities during long-term growth and provide engineering solutions.

Firstly, a 2D global CFD model was built to simulate the evolution of crucible configuration due to crystal growth, crucible dissolution, and polycrystal precipitation. This model could estimate the maximum available growth time for a given control recipe. A machine learning-based optimization system was subsequently constructed to optimize an adaptive control recipe, which corresponds to a thicker crystal with flatter growth front and longer available growth time.

Secondly, the evaporation and reaction of aluminum were simulated to study the instability of solution chemical composition during long-term growth. The detailed transport path of aluminum in the growth system was determined by thermodynamic calculation. The constructed model could predict the evolution of aluminum concentration inside the solution. Moreover, an improved geometric design was proposed to suppress evaporation and better preserve the aluminum in the solution during growth. The effect of the improved design was demonstrated both numerically and experimentally.

Finally, a simulation model was built that can predict the evolution of macrostep morphology on the entire crystal surface under the given control parameters. This model could be applied to investigate the effect of macroscopic control parameters on the step morphology, and the simulation results were validated by the experiments. Most importantly, through this model, a more sophisticated control pattern was designed and improved. The improved control pattern could result in uniform step morphology on the entire crystal surface, as well as freely-controlled step bunching level during the long-term growth process.

Contents

1. Introduction

1.1 Background

Today, global warming is an approaching threat to human society and global ecology, and is considered related to the greenhouse gases emitted from human activities. To reduce CO_2 emission and save energy, one of the most important tasks is to increase the utilization efficiency of electric power, or in the other words, reduce electricity waste.

From the electric power generation to end users' utilization, the electric power is undertaken regulation and conversions, including AC-DC, voltage, current, and frequency conversion, to better fit the load requirement of various electronic devices. However, about 26% of energy is lost in this delivery and conversion process [1]. The devices that achieve these conversions are called power devices. Silicon (Si), known as the most famous semiconductor material owing to its high crystal quality and economic efficiency, has acted as the main material for power devices ever since first being applied in thyristors in 1956. In the 1980s, the rapid progress of Si-based power devices, namely, GTOs (Gate Turn-off Thyristor), light-triggered thyristors, MOSFETs (Metal-Oxide Semiconductor Effect Transistor), IGBTs (Insulated Gate Bipolar Transistor), etc. enabled to meet various conversion power needs from small to large capacity. Since the 1990s, the research on power devices has focused on improving performance by introducing the LSI (Large-Scale Integration) microfabrication technology. However, the conventional Si-based power devices are gradually reaching their ultimate in low-loss and high-speed performance, limited by the physical properties and fabrication technologies. Since the Si technology is too mature for any potential revolutionary improvement, a new semiconductor material might be the solution to satisfy the increasing needs of high-temperature, high-power, and high-frequency application in a harsh environment.

Among the candidates, Silicon Carbide (SiC) is considered the most promising material for next-generation power devices due to its outstanding material properties. Compared with Si, 4H-SiC (one of the SiC polytypes) exhibits approximately 3 times higher bandgap, 10 times higher breakdown field, 2.7 times higher electron saturated drift velocity, and 3 times higher thermal conductivity [2], which enable SiC-based power devices to work under high temperature, high voltage, and high frequency with better conversion efficiency, smaller size, and simpler cooling system.

In 2015, a SiC-based inverter was installed in a 1000 series Odakyu electric train and was verified to achieve an 80% reduction in size and weight of the power module as well as a 40% reduction in power consumption compared with the conventional train

equipped with Si-based power devices [3]. In 2018, Tesla Corporation applied SiC-based inverter in their Model3 series electric vehicles, as the first high-lass automobile manufacturer to integrate a full SiC power module in the product, and this innovation led to less inverter weight and size, more space for streamlining design and more available range [4]. Moreover, the superiority of SiC devices was reported in other application fields like power distribution network [5], electric aircraft [6], wireless power transfer [7], and solar power system [8]. Due to these remarkable performances and the development of relevant technology, the power SiC market grew rapidly, which was 541 million dollars in 2019, and is expected to reach more than 2.5 billion dollars in 2025 [9].

However, regardless of the strong market demand and outstanding performance, two factors are limiting the competitiveness of the SiC industry. The first is the cost, where one 6-inch SiC wafer costs about 1000 dollars, while it costs less than 40 dollars for an 8-inch Si wafer. The other factor is the relatively low yield of the SiC crystal: only 40-50% of the grown SiC crystal can be utilized for further processing due to the quality problem, while it is about 85% for Si crystal. To address these two issues, the SiC crystal growth method should be focused on and improved.

1.2 Growth methods of SiC crystal

The history that humans knew, understood, and grew SiC crystal is not short. In 1824, Bertelius [10] firstly proposed that a silicon-carbon bond might in fact exist in nature. In 1892, Acheson invented a method to mass-produce SiC powder by heating the mixture of silica and coke to more than 2500 °C [11]. This so-called “the Acheson method” is the basis of SiC powder manufacturing nowadays, which is widely utilized for grinding abrasives. However, the SiC crystal yielded through this method cannot be applied in electronic fields due to impurity contamination, poor crystallinity, and small size. In 1955, a sublimation method, also known as the “Lely method” [12], was proposed and could produce SiC crystal with relatively high purity for the electronic application. However, this method was still limited by the crystal size and difficulty of controlling the polytype due to the nature of spontaneous nucleation. Although dramatic progress has been made in growth method and process ever since, nowadays quality and production efficiency are still two factors that hinder the mass-production of SiC crystal. To address these two problems, three mainstream growth techniques are under discussion, namely, the physical vapor transport (PVT) method, the hot temperature chemical vapor deposition (HTCVD) method, and the top-seeded solution growth (TSSG).

1.2.1 PVT method

Improved based on the Lely method, the PVT method is also known as the seeded sublimation method, and has been investigated since 1978 [13]. The schematic diagram

of this growth method is shown in Fig. 1.1. The polycrystalline SiC powder placed at the bottom of the crucible is heated up to around 2500 °C, and will decompose into vapor components (including Si, Si_2C, Si_2C, etc.) under the high temperature and low pressure. These vapors are then transported upward to the seed crystal under the effects of both diffusion and convection. To guarantee the convection, the growth system is normally filled with an inert gas like Ar with 50-5000 Pa in pressure. At the surface of seed crystal, which is manually controlled as 50-100 °C cooler than the bottom, the vapors re-crystallize into SiC following the crystal orientation and polytype of the seed crystal. The typical growth rate is 0.1-2 mm/h [14-17]. Compared with the Lely method, the application of the seed crystal can suppress spontaneous nucleation and significantly improve the crystal size.

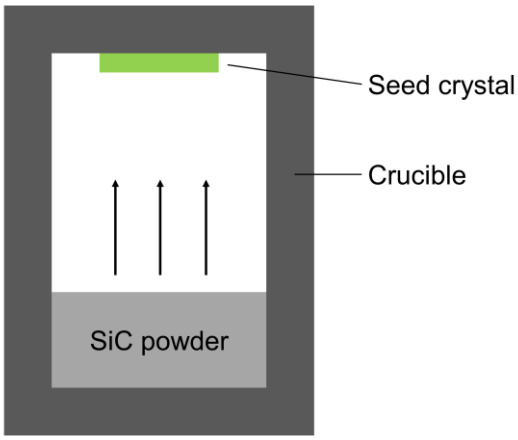

Figure 1.1 Schematic of growing SiC by the PVT method.

Owing to its relatively low cost and simple growth process, the PVT method has attracted remarkable research efforts and is the only method achieving commercial production of SiC crystal so far. Nowadays the diameter of commercial SiC wafers from the PVT method is 6-inch, while the 8-inch wafer sample has been developed and exhibited. Nevertheless, the drawbacks of PVT methods are non-neglectable.

1. Since the growth furnace is a close system, several unstable factors including deposition on the area other than the seed crystal and changing of C/Si ratio in the source material may influence the growth condition and crystal quality during long-term growth;

2. Due to the high growth temperature and the growth condition away from thermodynamic equilibrium, the defects densities including threading screw dislocation (TSD), thread edge dislocation (TED), basal plane dislocation (BPD), and micropipe in SiC crystal yielded by the PVT method are still at a high level, which significantly deteriorate the performance of power devices;

3. The diameter enlargement is difficult since the crystal mainly grows in the vertical direction. The development of larger-diameter crystals usually takes numerous efforts in both time and money;

4. The growth of the p-type crystals is difficult since the normal p-type dopants like aluminum (Al) and boron (B) are volatile under high temperature and low pressure required by the PVT method. Therefore, the current commercial SiC products are mainly in n-type or semi-insulated type.

1.2.2 HTCVD method

As a potential alternative of the PVT method, the HTCVD method was proposed resembling the chemical vapor deposition (CVD) technique, the schematic of which is shown in Fig. 1.2. Unlike the PVT method, the growth system is open where SiH_4 and C_3H_8 are streamed into the chamber as Si source and C source, respectively. By precisely controlling the vertical temperature distribution (normally more than 2000 °C) in the chamber, the two gases react with each other and form a "SiC cluster cloud" which will further decompose into the same gaseous species as the PVT method and transport upward for crystallization. Compared with the PVT method, this method can continuously feed the source material, precisely control the C/Si ratio, and achieve p-type doping. Through HTCVD method, a growth rate of 0.3-0.6 mm/h was reported along with a high purity level [18-20]. However, the high cost for source gases and high requirement of control techniques are the two limitations of this method.

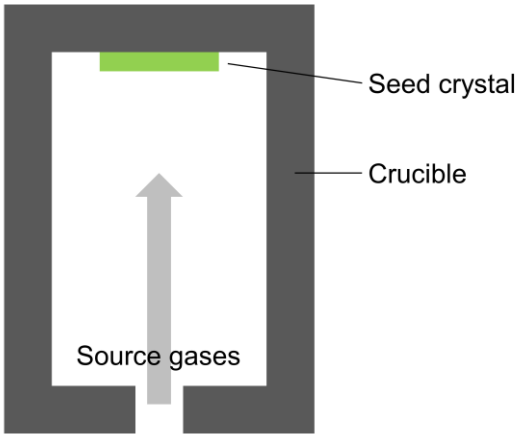

Figure 1.2 Schematic of growing SiC by HTCVD method.

1.2.3 TSSG method

Growing directly from the liquid phase of the crystal is the most common and mature route to obtaining high-quality crystal because the growth condition is close to the thermodynamic equilibrium [21]. Unfortunately, this concept is not feasible for SiC since the stoichiometric SiC melt only exists, theoretically, at more than 3200 °C and

10^5 bar. Even if this extreme condition can be realized somedays, this high temperature will greatly narrow the differences in formation enthalpy of different polytypes, and therefore make it impossible to control the polytype stability during growth. To use a non-stoichiometric Si-C solution is not a good idea either, since the C solubility in pure Si melt is low (0.17 at% at 1800 °C) and will result in a low growth rate (less than 10 μm/h). Therefore, although being investigated as early as the 1960s, the route of growing SiC crystal from the liquid phase was gradually surpassed by the PVT method.

Since the 21st century, this route has again attracted attention, owing to the advance in material science research. Although the growth rate of up to 200 μm/h was reported using pure Si as the solvent under 2000 °C and 150 bar [22], it is the discovery of several additives in the solution that with no doubt enhanced the feasibility of growing SiC crystal from the liquid in a reasonable condition. These additives significantly increase the C solubility in solution, including Fe, Cr, Sc, Tb, Ti, etc. [23-27].

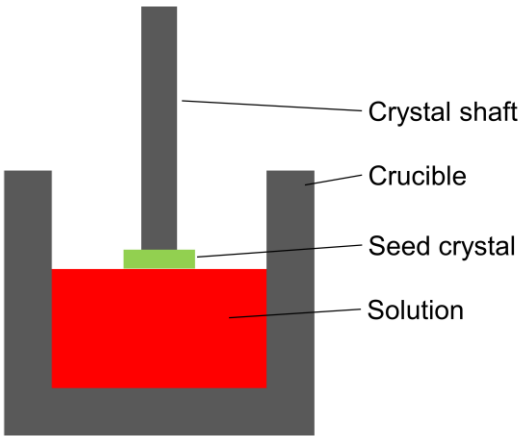

Figure 1.3 Schematic of growing SiC by TSSG method.

Among the several liquid phase SiC crystal growth methods [22, 28, 29], the top-seeded solution growth (TSSG) method, adapted from Czochralski (Cz) method, is especially suitable for obtaining large-size SiC bulk crystals and being applied in mass-production. The schematic of the TSSG reactor is illustrated in Fig. 1.3. The graphite crucible acts not only as the container, but also as the heat and carbon source for the solution. The crucible wall is directly heated to about 1800 °C by the induction coil, where the carbon dissolves into the solvent due to high temperature and local undersaturation. The carbon is then transported under both convection and diffusion effects to the seed crystal in the center, where the temperature is designed relatively low and the carbon becomes supersaturated. This supersaturation provides the driven force for the crystallization of SiC at the surface of the seed crystal.

Compared with other methods, the TSSG method has the following advantages.

1. TSSG method can yield SiC crystals with high quality due to two aspects. On one hand, fewer defects are generated during the process. This can be attributed to: I. the growth condition is closer to the thermodynamic equilibrium [22] owing to lower crystallization latent heat and lower supersaturation; II. the growth temperature is low, which avoids the occurrence of high thermal stress while cooling to room temperature. Furthermore, the intrinsic defects in the seed crystal can even be reduced or removed during the solution growth. TSDs and TEDs were reported to be converted into BPDs during growth and finally extruded outside the crystal [30-34]. Likewise, micropipe, which is a killer defect, can also be filled and become completely invisible [35, 36];
2. The cost of the TSSG method is low owing to the lower requirement of the growth system and lower cost of high-purity raw material (mainly Si);
3. Diameter enlargement can be easily achieved by controlling the height of the meniscus [27, 37, 38], resembling the shoulder process in the Cz method. Recently, our group reported the diameter expansion from 6-inch to 6.5-inch [39], which is the largest SiC crystal grown from the TSSG method up to date;
4. TSSG method can yield p-type SiC crystal by adding Al into the solution [40, 41], since the evaporation of Al is not so strong under relatively low temperature and high pressure, unlike the PVT method.

Despite these advantages, the TSSG method is still not preferred by the industry due to relatively low production efficiency, namely the crystal thickness. For the PVT method, the average thickness is about 30 mm for the 6-inch crystal. The same value was achieved only by a 1-inch crystal grown from the TSSG method [42], while the maximum thickness reported for the 6-inch crystal was only 4 mm [39], which indicates a very low yield ratio between the product and raw materials. To enhance the competitiveness of the TSSG method and make it prevalent, increasing the crystal thickness is the critical target. The crystal thickness is determined by two factors: growth rate and available growth time. For the former one, numerous efforts have been made in the last decade to increase the growth rate to up to 2 mm/h by improving the solution composition [23-27, 43], system configuration [44-47], and controlling method [48-50]. However, too high growth rate corresponds to large supersaturation and is far from thermodynamic equilibrium, which may negatively influence the polytype stability and step stability. Therefore, the ideal growth mode is to maintain a stable growth condition for as long time as possible, which defines the “available growth time”. Unfortunately, increasing the available growth time has rarely been discussed in previous studies, due to the incapability to in-situ monitor the ongoing growth process and thusly lack of understanding of the long-term instabilities which directly limit the available growth time.

1.3 Long-term instabilities in TSSG method

The growth furnace for the TSSG method is a closed system, and therefore it is intrinsically unstable where the physical and chemical reactions proceed unidirectionally and the growth condition evolves irreversibly. Among the several unstable factors, crucible configuration change, solute/solvent evaporation, and step morphology evolution directly affect the growth condition and deviate it from the well-designed initial condition.

1.3.1 Configuration change of crucible

Fig. 1.4 (a) shows the schematic of the carbon transport path inside the solution, which is initiated by the dissolution of carbon from the graphite crucible wall due to the undersaturated condition. The dissolved carbon is transported to the surface of the seed crystal and the bottom of the crucible via convection and diffusion effects. The single crystal grows on the seed crystal with the same orientation, while polycrystals freely precipitate at the crucible bottom through spontaneous nucleation. These factors result in unsteady changes in the configuration inside the crucible, a practical example of which can be found in fig. 1.4 (b).

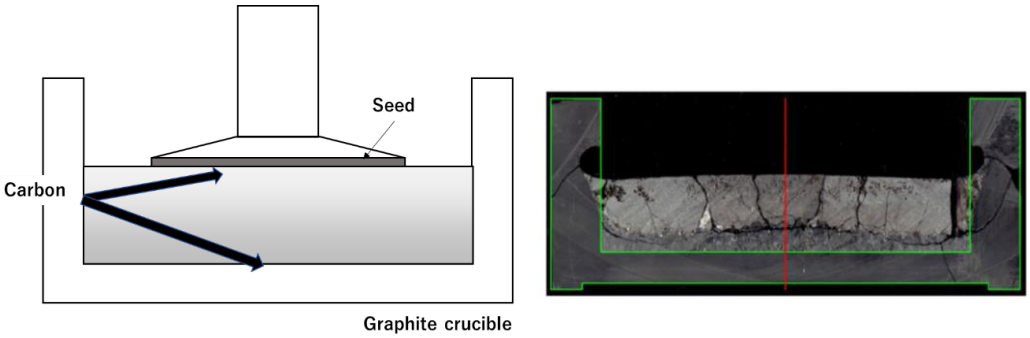

(a) (b)

Figure 1.4 (a) Schematic of carbon transport in crucible, and (b) crucible configuration after 30 h growth.

The relevant studies are few but insightful. Liu et al. conducted a numerical simulation and reported that the uneven shape change of the single crystal affected the local flow pattern, which altered the growth rate distribution on the crystal surface and made the fluctuation of the crystal front more and more evident as the growth proceeded [51]. Mukaiyama et al. also conducted the numerical simulation and demonstrated that the shape change of the crucible significantly influenced the flow pattern, temperature, and growth rate [52]. According to their result, the maximum temperature inside the solution increased by more than 100 °C and the growth rate doubled over merely 6 hours of growth. These large variations make the growth deviate

from the merit of the TSSG method, which is close to equilibrium, and may result in low crystal quality. Besides the quality problem, these unsteady changes in crucible configuration may cause safety problems as well. The over-dissolution of the crucible wall may lead to an increasing risk of cracking under high-speed rotation of the crucible, and the consequent leakage of high-temperature solution would be disastrous. Moreover, the heavy precipitation of polycrystals can lead to a collision with the growing and rotating single crystal and cause mechanical damage. Therefore, controlling and suppressing the crucible configuration change is vital for increasing available growth time.

1.3.2 Composition change of solution

Besides the physical effects caused by the crucible configuration change, the chemical effects caused by solution composition change limit the available growth time as well. Along with the long-term growth in the closed TSSG system, the solution tends inevitably towards the drought of Si due to the continuous consumption but lack of supply, while the C ceaselessly dissolves from the graphite crucible. This composition change will consequently lead to the termination of SiC growth once the solution composition departs from SiC saturation to carbide or graphite saturation [53]. To deal with this potential problem, several methods have been proposed to compensate for the Si loss when precipitating into SiC crystal, such as using SiC included crucible or directly using SiC ceramics as a source material [53, 54]. However, these methods will increase the cost of source material, and more importantly, they could not compensate for the loss of Si through evaporation. Since the growth temperature is about 500 °C higher than the melting point of Si and normally the chamber is with atmosphere pressure, the evaporation effect becomes non-negligible, especially for long-term growth.

In addition, some materials other than Si are added to the solution for purposes including increasing C solubility for higher growth rate, decreasing interface energy for lower 2D nucleation possibility, enhancing repulsive interaction between steps for less step bunching, etc. Among them, some additives are volatile, especially in the extremely high-temperature environment, and the continuous evaporation or reaction loss of a certain solute during long-term growth may make the solution deviate from its predetermined and well-designed composition. Despite the small amount of these volatile additives, the subtle change in their concentration inside the solution may significantly alter the chemical environment for the growth interface. For example, it has been reported that 1% more Al in the solution could significantly improve the crystal surface morphology and polytype stability [40]. Al in solution acts as both surface stabilizer and p-type dopant, but is easy to evaporate and react with graphite components. It can be imagined that the continuous loss of additives like Al may degrade

the crystal quality and result in inhomogeneous doping. Moreover, the large amount of evaporation may contaminate the furnace chamber and reduce the lifetime of components made from carbon like the thermal insulator.

Therefore, the solution composition change during long-term growth is worth investigating, and the possible methods to suppress this unsteady change are crucial to prolonging the available growth time. Unfortunately, relevant study regarding the solution growth of SiC crystal has never been reported in literature, to the best of our knowledge.

1.3.3 Morphology change of macrosteps

Unlike the previous two factors, which are affected by the physical and chemical environment in the macroscopic growth system, the third unsteady factor occurs on a smaller scale and involves the essence of crystal growth.

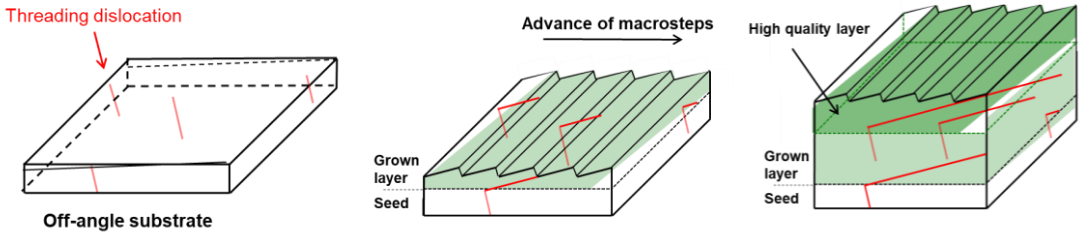

(a) (b) (c)

Figure 1.5 Schematic of dislocation conversion process. (a) The native TDs in the substrate; (b) Deflection of TDs' propagation direction due to macrostep advancing; (c) Formation of TD-free layer.

As introduced in section 1.2, one of the advantages of the TSSG method is the capability to convert and eliminate the native dislocations inside the seed crystal and yield grown crystal with high quality. The mechanism of this dislocation conversion is depicted in Fig. 1.5. Threading dislocations (TDs), common dislocations in SiC crystal, propagate along the *c*-axis, which is also the crystal growth direction in most cases. Therefore, these dislocations would permanently reside and propagate in the grown crystal if not interfered with (Fig. 1.5 (a)). A method named "repeated *a*-face" (RAF) was once proposed by repeatedly switching the growth orientation in *a*-face using the seed crystals sliced in the perpendicular direction of the previous grown crystals [55]. This method was examined through the PVT method to effectively reduce the dislocations in the SiC single crystal by 2 to 3 orders of magnitude. However, since the new seed is sliced perpendicularly from the grown crystal, this method requires the grown layer thickness to be with the same scale as the seed crystal diameter, which is almost impossible for large size crystal like 6-inch. Fortunately, in recent studies of SiC solution growth it was uncovered that by applying growth slightly deviated from the [0001] direction, also

known as off-axis growth, macrosteps formed on the crystal surface could convert TDs into defects on the basal planes (Fig. 1.5 (b)) owing to the image force from macrostep edge [33, 56]. These defects propagate no longer into the subsequent grown layer, and will finally be extruded outside of the crystal (Fig. 1.5 (c)). Once all the native dislocations are converted, an ultra-high-quality crystal can be obtained [34]. Compared with the RAF method, this approach is more feasible for large-size crystals, where the formation of macrosteps is the key to achieving the conversion of TDs during growth. Moreover, higher and steeper macrosteps were reported to be preferable for higher conversion rate [32, 57, 58].

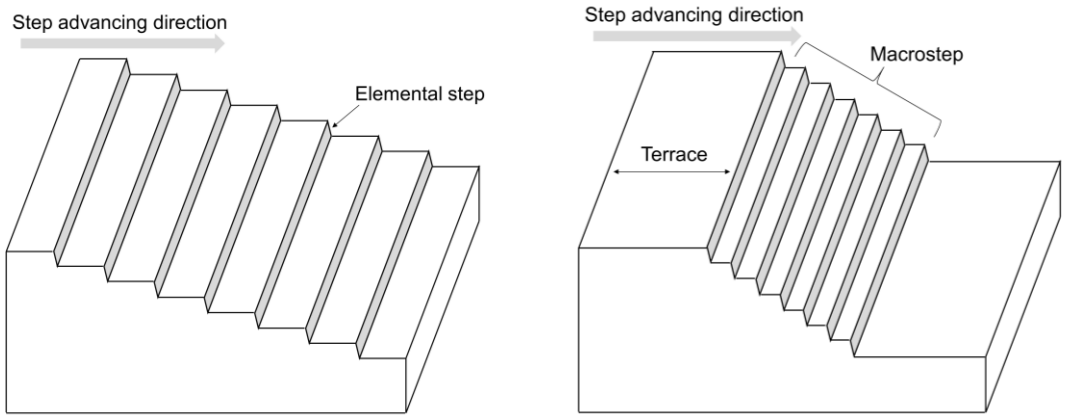

(a) (b)

Figure 1.6 (a) Equally spaced elemental step train; (b) Macrostep caused by step bunching

The formation of macrosteps is one of the unique features of the TSSG method, and the schematic is plotted in Fig. 1.6. Since the diffusion coefficient of the growth unit, namely C, in the TSSG method is about 10^6 times lower than that in the PVT method [22], the growth is a transport-limited process and is therefore unstable. In the initial stage of growth, the elemental steps are equally spaced and move forward with the same velocity (Fig. 1.6 (a)). If the position of one elemental step *N* is advanced a little more by some perturbation, the velocities of both step *N* and its front neighbor *N+1* decrease due to the competition for the growth unit, while the behind neighbor *N-1* accelerates. The behind step will then join the plodding pair of *N* and *N+1*, and further decrease their velocities by intensifying the local competition of the growth unit. This initial perturbation will set off a chain reaction and finally, a huge step bunch appears and slowly advances (Fig. 1.6 (b)). This step bunch is also known as the foregoing “macrostep”.

Like the two sides of the same coin, macrosteps with a reasonable height bring the benefit of defects conversion, but over-developed macrosteps may cause mainly 3 troubles.

1. In the case of impurity doping, the impurity-incorporation rate differs between step and terrace (the distance between two neighbor steps). If the step is too high and turns into a macrostep, the difference in impurity incorporation may be amplified to a macro-scale level. This was confirmed by the observation of growth striations in the cross-section view, following the moving traces of macrosteps [59-61]. The growth striations with different colors imply inhomogeneous impurity distribution, which negatively affects the crystal quality;

2. The generation of macrostep normally leaves a wide terrace behind (as shown in Fig. 1.6(b)), where the local supersaturation is high due to a lack of competition for growth units. Once the supersaturation exceeds a critical value, step-flow-growth mode no longer dominates and 2D nucleation occurs on the terrace. The 2D nucleation will collide with the following steps causing new step bunching, and may alter the poly-type inherited from the seed;

3. Most importantly, the over-developed macrosteps can result in the inclusion of solvent into the crystal, which is one of the most intractable problems for solution growth of SiC crystal. Fig. 1.7 illustrates the formation of two types of inclusion caused by macrostep. In the first case, the advance velocity becomes height-dependent on one macrostep due to the difficulty of the solute reaching the bottom area when the macrostep is too high. As the growth proceeds, the macrostep will form an overhanging structure (Fig. 1.7 (a)), and eventually include the solvent inside. In the second case, when the macrostep becomes too high, the Thomson-Gibbs effect is no longer able to keep the straightness of the step edge, which will lose stability and bend into cellular structure due to some tiny perturbation (Fig. 1.7 (b)). Likewise, the solute cannot be transported into the deep of the valley, resulting in the stagnation of growth and the inclusion of the solvent. The formation of inclusion significantly deteriorates the crystal quality by not only reducing the available area on the wafer, but also generating new dislocations when the included Si solvent solidifies and expands in a closed volume.

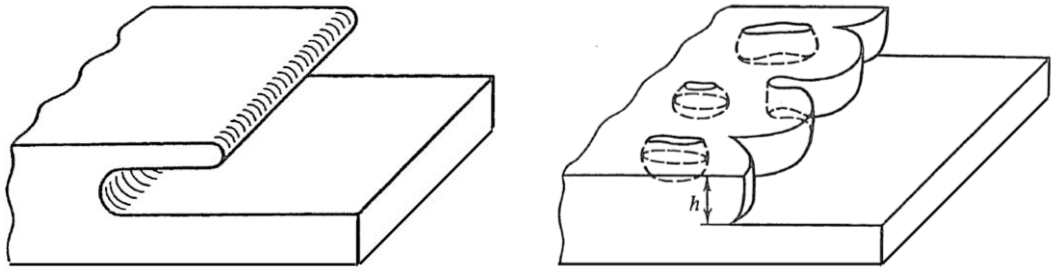

(a) (b)

Figure 1.7 Two types of inclusion caused by (a) overhanging of macrostep, and (b) wandering of macrostep [62]

In summary, the development of macrosteps is the third unsteady factor during long-term growth. To achieve the crystal with a high defect conversion rate but low inclusion density and high poly-type stability, the macrosteps on the whole crystal surface should be controlled to achieve a certain height but further bunching should be suppressed. Previous studies have demonstrated that the macrostep behavior is sensitive to the local flow direction, where the flow opposite to the step advancing direction suppresses the step-bunching, and *vice versa* [63-66]. However, how to apply this theory to practical crystal growth and freely control the step morphology on the entire crystal surface remains unexplored.

1.4 Numerical modeling and relevant studies

According to the foregoing description, the unsteady behaviors of the crucible configuration, solution composition, and crystal surface morphology should be well understood, to better control the crystal growth process for a more stable growth condition and longer available growth time. However, since the TSSG furnace is a closed system under extremely high temperature, it is almost impossible to directly access these information without disturbing the ongoing experiment. Furthermore, the information provided by the ex-situ observation after the experiment is very limited, which may only reflect the final state and hinder us from obtaining the mapping relationship between the crystal quality and multiple controlling parameters. Therefore, numerical methods are preferable in the present dissertation to investigate the long-term instabilities in SiC solution growth. Although the experimental studies are indispensable and their contribution can never be overlooked, numerical models reveal more details from various perspectives regarding the spatial distribution and temporal evolution of the physicochemical parameters. Besides, numerical models are normally more time-saving and economical than experiments, and therefore are more suitable to be applied for engineering purposes like parameter study and new design verification. Moreover, some up-to-date numerical models involving machine learning present superiority in instant data prediction and show promise for real-time optimization of crystal growth. The numerical models utilized in this dissertation and their relevant studies in crystal growth are introduced in the following sections.

1.4.1 Modeling of flow, heat, and mass transfer

Crystal growth is a phase change process, driven by the chemical potential difference between the fluid (ambient) phase and solid (crystal) phase. This chemical potential difference can be expressed as the vapor pressure difference of source gas for growth from the gas phase, while it is the concentration difference of solute for growth from solution, and the temperature difference for growth from melt. Therefore, transport of

heat or species from source to growth interface is the key element of the crystal growth process, where fluid flow plays a dominant role and has been the continuous focus in the growth of large and high-quality single crystals [67-71].

The mechanism of fluid flows is not complicated, following the basic rules of Newton's law of motion, which can be written as:

$$m\vec{a} = \vec{F} \quad \text{(Eq. 1-1)}$$

where m denotes the mass of a rigid body, $\vec{a}$ the acceleration, $\vec{F}$ the net force being applied on the body. If we replace the rigid body with an infinitesimal-size fluid dollop, the equation above can be re-expressed as:

$$\rho\frac{D\vec{v}}{Dt} = -\nabla P + \mu\nabla^2\vec{v} + \vec{F}_b \quad \text{(Eq. 1-2)}$$

where ρ is the density of the fluid, $\frac{D\vec{v}}{Dt}$ is the total derivative of velocity with respect to time, and the terms on the right-hand side are pressure force, viscous force, and body forces, per unit volume respectively. Since ρ and μ (viscosity) are material properties, and P (pressure) is interrelated with $\vec{v}$ (velocity), this equation indicates that when the given external body forces are applied to the bulk fluid, the velocity distribution can be accordingly derived.

Once the velocity is known, the transport of both heat and species can be described and solved in resembling forms:

$$\rho C_p\frac{\partial T}{\partial t} + \rho C_p\vec{v}\cdot\nabla T = k\nabla^2\phi + S_h \quad \text{(Eq. 1-3)}$$

$$\frac{\partial C}{\partial t} + \vec{v}\cdot\nabla C = D\nabla^2 C + S_s \quad \text{(Eq. 1-4)}$$

where C_p denotes the heat capacity, T the temperature, k the thermal conductivity, S_h the heat source, C the concentration of a certain species, D the diffusion coefficient, and S_s the species source, respectively.

With the equations above, it seems that the crystal growth furnace is now an open book, where one can capture every detail, both spatially and temporally. However, this dream has not been realized yet, due to the following three reasons: 1. Regardless of their seemingly compact appearance, these partial differential equations can hardly be solved mathematically and the exact solutions only exist in some oversimplified situations; 2. The inner structures of the furnace are normally complex, consisting of various components with non-regular shapes and different material properties, which further adds difficulty in solving the equations; 3. The flows in most crystal growth systems, especially the TSSG system, are governed by various forces whose interaction and cooperation are complicated to predict. Fig. 1.8 illustrates the four typical convection patterns in the crystal growth system, governed respectively by buoyancy,

centrifugal force, Marangoni force, and electromagnetic force. Details of these forces and their effects on crystal growth can be accessed in literature [72, 73].

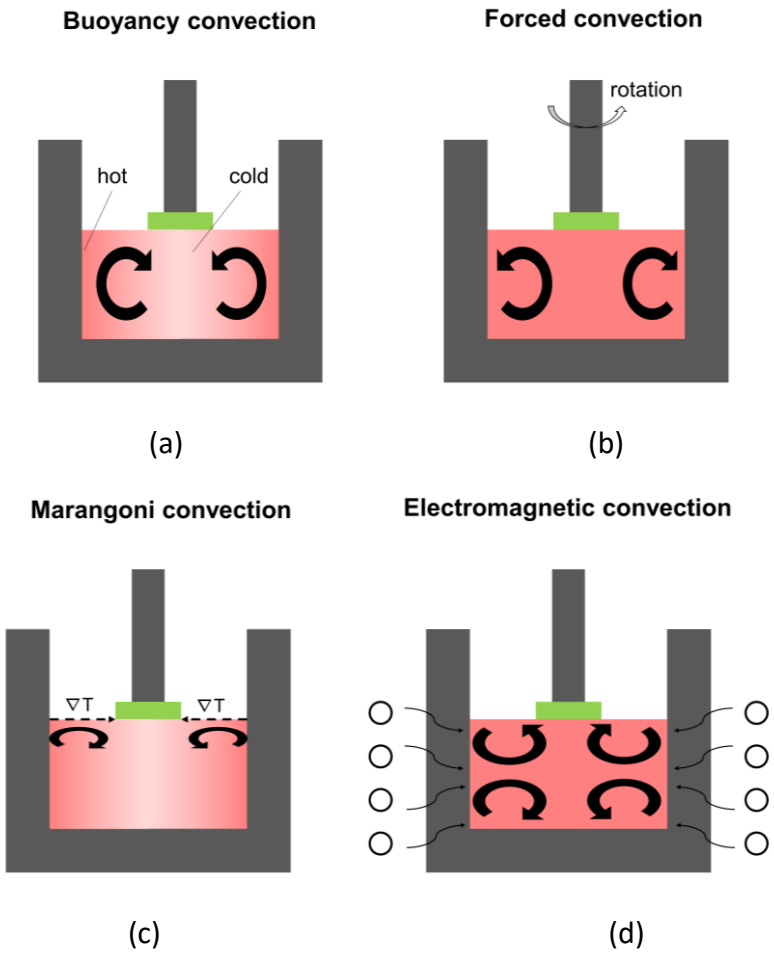

Figure 1.8 Four typical convection patterns contributed by (a) buoyancy force, (b) centrifugal force, (c) Marangoni force, and (d) electromagnetic force.

Thanks to the development of the computational fluid dynamics (CFD) technique, the potential and advantages of computer simulation have been widely discussed in the field of crystal growth in the past several decades, and nowadays it has already become the best complement to experimental crystal growth research. The computer simulation numerically solves the governing equations shown in Eq. 1-2~1-4. By separating the continuous domain into sufficiently small discrete sub-domains (also known as “mesh” or “grid”), the partial differential equations can be approximately discretized into linear forms, and the accurate solution will be approached through the computer iterations. The CFD modeling can deal with complex geometric shapes and multi-physics processes including fluid flow, heat transfer, mass transfer, electromagnetic induction, and chemical reactions in the crystal growth system, which provides a more straightforward perspective on macroscopic crystal growth

phenomena.

In the field of SiC solution growth, numerical studies utilizing CFD modeling have contributed considerably to enriching people's understanding of flow, heat, and mass transfer in the growth system. Through the comprehensive studies regarding the multiple forces in the solution, it was illuminated that buoyancy and Lorentz force are the two dominant factors that define the global flow pattern, whereas the Marangoni force causes instability locally near the crystal edge [47, 72, 74-78]. To achieve ideal temperature distribution near the crystal, the effects of system configuration were investigated, including hot zone [79-81], crucible [51, 72, 82], shafts [83], and meniscus height [37]. To enhance C transport in solution, which directly determines the growth rate and interface uniformity, numerous approaches were proposed via numerical investigation including high-speed rotation of the seed crystal [50], accelerated crucible rotation technique (ACRT) [84], advanced magnetic fields [85, 86], and some subtle but sophisticated apparatus which can freely manipulate the convective flow [44, 47, 87]. Most of these proposals were examined in experiments, and the results further proved the effectiveness of CFD modeling.

1.4.2 Modeling of step motion

Although the CFD modeling can provide comprehensive information regarding the distribution of macroscopic physical quantities in the system, it might be incapable if one investigates closer to the crystal surface. In conventional CFD modeling, the boundary condition for C transport on the crystal surface is normally simplified as the value of equilibrium C concentration, which assumes a "normal growth mode" as shown in Fig. 1.9(a), where the crystal surface is rough and offers kink sites with sufficient density, and therefore the C incorporation into the crystal is position-independent. This growth mode occurs usually in the cases like metals growing from their liquid phase where the temperature is higher than the roughness transition temperature [88]. In the case of solution growth of SiC, however, it normally follows the "step-flow growth mode" shown in Fig. 1.9(b), where the solute atoms may preferentially be incorporated at the kink sites on the steps, other than the terrace. These steps are provided by either the native steps on the seed crystal due to the off-axis cutting or the spiral growth center. The continuous C incorporation into the step results in the advance of the step front, which is also referred to as "step motion".

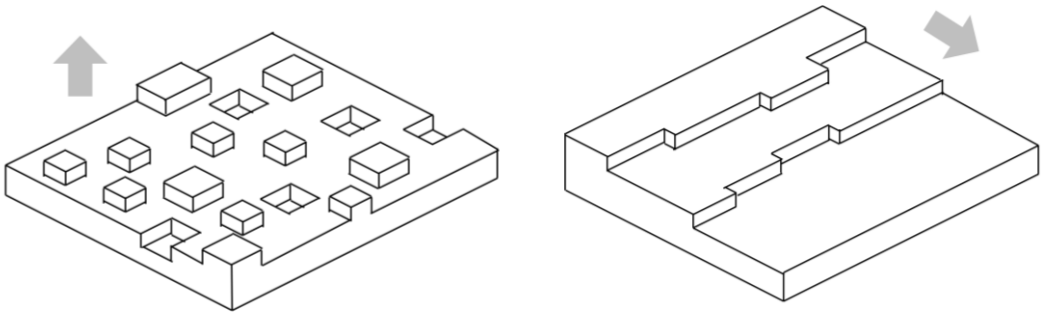

(a) (b)

Figure 1.9 Schematics of (a) normal growth, and (b) step-flow growth. The arrow indicates the growth unit stacking direction.

Chernov introduced a volume diffusion model to describe this phenomenon in solution growth [89], assuming that the incorporated adatoms directly diffuse from the ambient phase. The step advancing velocity in this model can be expressed as

$$v_{st} = K_{st}(C - C_{eq})V \quad \text{(Eq. 1-5)}$$

where K_{st} is the step kinetic coefficient defined by the incorporation rate of growth units near the step. C is the growth unit concentration near the step, while C_{eq} is the equilibrium (saturated) concentration of the growth unit determined by the local temperature. V denotes the volume of a growth unit. This surface kinetic model can be utilized to depict the motion of a single step and the interaction among multiple steps. Lin et al., who firstly coupled this model with bulk transportation (Eq. 1-4) to study the dynamic behavior of steps in solution growth, demonstrated that step density and terrace width could change in response to nutrient concentration on a large scale [90]. Vekilov et al. addressed the instability of dynamical interaction of transport and kinetics, where a step bunch triggers a cascade of new step bunches through the microscopic interfacial supersaturation distribution [91]. Kwon et al. included also the surface diffusion phenomenon into the surface kinetic model, which extended the applicability of the model in various solution growth systems [92]. Inaba et al. reported the effects of several parameters on the formation of step bunching, including solution flow direction, solution flow rate, and repulsion strength between steps [93, 94]. Regarding the solution growth of SiC, Liu et al. recently employed this model to study the instability of steps motion under different solution properties, and accordingly proposed a criterion for designing the solution composition [95].

Since the elemental step is on atom-scale and separately tracing each step on the whole crystal surface is computationally unaffordable, the previous studies focused mainly on 2D, local and transitory simulation. Although they uncovered important and general features of step development, further improvement is required to connect the

3D step morphology on the whole surface with macroscopic controlling parameters, to provide a more direct guide to the practical crystal growth experiment.

1.4.3 Machine learning models

The foregoing two numerical models can, to some extent, precisely describe the transport phenomena in bulk solution and the step kinetics on the crystal surface, and therefore enrich the understanding of the growth process. Nevertheless, in an engineering context, the rich understanding is only a necessary but not sufficient condition to yield an ideal crystal, since there is a tradeoff between the high crystal quality and high growth rate. A suitable growth condition is required to achieve a balance. The growth condition is determined by various controlling parameters that interact and cooperate non-linearly, making it complicated to analyze the tendency and discover the optimal combination. In the past, industrial development and optimization were mainly based on experience and trial experiments, which were time-consuming and the process was therefore slow. For reference, it took about 40 years to enlarge the diameter of an industrial mono-crystal silicon ingot from 1 to 12-inch. Although the emerging CFD simulation can act as a powerful and time-saving alternative to experiment, the data acquisition time is still considerable, especially in cases with complex geometric structures and harsh situations. The former factor results in a larger number of meshes to capture the configurational features, while the latter requires more elaborate mathematic models to describe the turbulence or radiation. Therefore, high-speed acquisition of accurate data is essential to accelerate crystal growth development.

The advent of the machine learning technique has brought this goal closer to fruition. Machine learning, a subarea of artificial intelligence (AI), is a mathematic tool to obtain knowledge regarding the mapping relationship directly between the inputs and outputs, and is particularly suitable for complex and non-linear situations like process parameters optimization and automation of manufacturing.

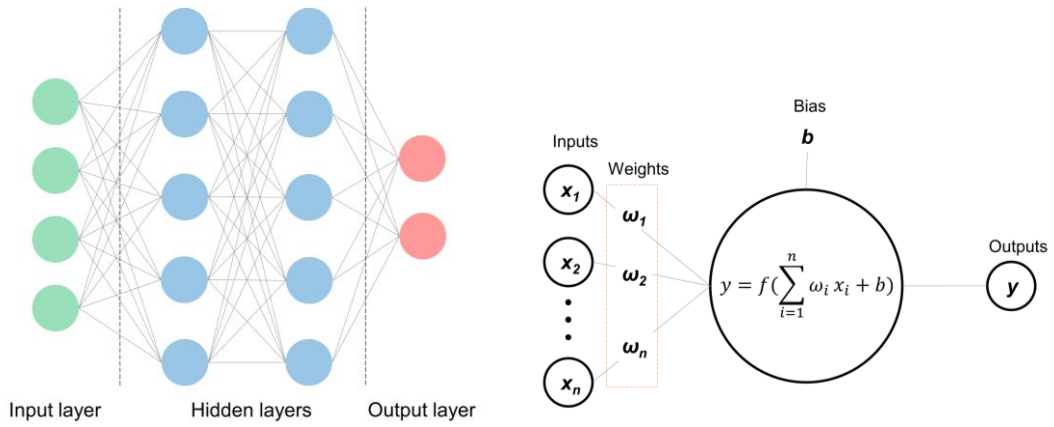

(a) (b)

Figure 1.10 (a) Typical architecture of a neural network, and (b) schematic of a neuron.

The artificial neural network (ANN) and its derivatives are by far the most widespread machine learning techniques. The artificial neural network is a computing system inspired by the biological neural networks that constitute animal brains, and is likewise powerful in correlating multiple variables and detecting non-linear dependence [96]. As shown in Fig. 1.10(a), a typical ANN consists of three layers, namely the input layer, hidden layer, and output layer. The whole network receives external inputs in the first (input) layer, processes the data in the intermediate (hidden) layer, and provides corresponding output in the last (output) layer. Every layer is an organization of artificial neurons, each of which acts as an independent computation unit to process the inputs and give the output (Fig. 1.10(b)). The most common output operation for the *j*-th neuron in the hidden or output layer can be expressed as

$$O_j = f(\sum_{i=0}^{n} \omega_{ji} \cdot x_i + b_j) \quad \text{(Eq. 1-6)}$$

where O_j denotes the output of this neuron, x_i the input received from the output of the *i*-th neuron in the preceding layer, ω_{ji} the weight of this connection, b_j the bias, and f the activation function to strengthen the capability to detect non-linear relationships. The most common activation function is the so-called “logistic sigmoidal function”, which has the form as

$$f(a) = \frac{1}{1-e^{-a}} \quad \text{(Eq. 1-7)}$$

Sets of prepared external data including inputs and outputs are used to “train” the ANN, according to which the ANN adjusts the weight ω_{ji} and bias b_j of each neuron, to minimize the error between the outputs given by ANN and the actual outputs. Through sufficient iterations, a well-trained ANN can learn the features of the data sets and instantly predict the output of a given input in the same feature domain.

In the field of SiC solution growth, the application of machine learning models has received increasing attention since 2018. Due to the lack of sufficient data directly from crystal growth experiments, machine learning models learned from the pre-calculated CFD results and then act as an alternative to instantly yield the prediction. Tsunooka et al. developed an ANN using 800 data samples prepared by CFD simulation [97]. In this model, the inputs were the controlling and configurational parameters, while the outputs were the velocity, temperature, and supersaturation distribution in the whole solution domain. It was demonstrated that the machine learning model could achieve high accuracy (correlation coefficient higher than 0.95) and extremely high-speed prediction (10^7 times faster than CFD simulation). Yu et al. subsequently applied this

model to design the hot zone configuration inside the chamber for a 6-inch growth system, and various possible solutions were yielded which led to the optimal growth condition [98]. Wang et al. adapted a reinforcement learning model to dynamically exchange data with CFD, to control the electromagnetic field and achieve a higher and more uniform growth rate [99]. Horiuchi et al. and Takehara et al. respectively combined the machine learning models with the adjoint method and Bayesian optimization to predict a preferred melt flow pattern which would lead to uniform growth rate distribution [100, 101]. Moreover, by using a convolutional neural network (CNN), the regional sensitivity of the flow pattern to the controlling parameter was analyzed and consequently a special focus could be implemented on the most sensitive area [102].

Although being proven to be efficient and effective in predicting the SiC solution growth, it should be noted that machine learning models do not replace the CFD simulation. Instead, they act as the extension of CFD simulation to accelerate the optimization process. Therefore, constructing an accurate CFD model to provide reliable training data is the premise of the application of machine learning.

1.5 Objective and contents of this thesis

As described above, the TSSG method exhibited great potential to yield high-quality SiC bulk crystals, which is essential for the next-generation semiconductor devices being applied in high-power, high-frequency, and high-temperature conditions. To achieve commercialization of this method, the production efficiency, determined by growth rate and available growth time, should be further improved. The growth rate is influenced by the growth condition such as temperature, solution composition, and solution flow field, while the available growth time is mainly limited by the unsteady factors during the long-term growth which make the growth deviate from the initially well-designed condition. The previous studies have addressed considerable discussion on increasing the growth rate, but the exploration regarding the unsteady factors and how to prolong the available growth time remains rare.

The previous studies suggested numerical simulation as a powerful tool to investigate the temporal and spatial details in the growth system, which is almost impossible to be experimentally observed due to the hostile environment. Therefore, the objective of the present dissertation is to numerically model the long-term solution growth of SiC, reproduce the multiple unsteady phenomena in virtual space, and accordingly conduct further improvement or optimization for a longer and more stable growth process.

The structure and detailed contents are as follows:

1. In chapter 1, the background, related studies, and the objective of this dissertation are introduced.

2. In chapter 2, a global numerical model is built to simulate the configurational change of the crucible during the long-term solution growth. The evolution of thermal, flow, and chemical fields under an original fixed controlling recipe is investigated, and the maximum available growth time is accordingly estimated. Then, machine learning-based optimization is conducted to yield a time-dependent recipe that is expected to consistently maintain the optimal growth condition. Moreover, the effectiveness of transfer learning is examined to further improve optimization efficiency.

3. In chapter 3, a global numerical model is built to simulate the change of solution composition, especially the Al concentration, due to chemical reaction and evaporation. The transport path of Al in the growth system is studied, and a structural design is proposed to suppress the Al loss in solution during long-term growth.

4. In chapter 4, a numerical model is built to simulate the evolution of macrosteps morphology on the entire crystal surface. The effects of several macroscopic controlling parameters on the crystal surface morphology are investigated. Improved control patterns are proposed to reduce local step-bunching and achieve homogeneous surface morphology. The simulated results are validated by experiments.

5. In chapter 5, the results of this dissertation are concluded.

Furthermore, in Appendix A, the training process, performance, and limitation of transfer learning in predicting the unsteady growth process are introduced. In Appendix B, a tentative discussion is made to investigate the role of turbulence in the solution growth of SiC, from two aspects.

References

[1] J. Conti, P. Holtberg, J. Diefenderfer, A. LaRose, J. T. Turnure, L. Westfall. *International Energy Outlook 2016 With Projections to 2040.* United States: N. p., 2016. Web. doi:10.2172/1296780.

[2] T. Kimoto, J. Cooper. *Fundamentals of Silicon Carbide Technology: Growth, Characterization, Devices, and Applications.* Wiley, 2014.

[3] Mitsubishi Electric (http://www.mitsubishielectric.co.jp/news/2015/0622-a_zoom_01.html).

[4] L. Gear. “Tesla’s Innovative Power Electronics: The Silicon Carbide Inverter” 2021.

[5] S. Madhusoodhanan, A. Tripathi, D. Patel, K. Mainali, A. Kadavelugu, S. Hazra, S. Bhattachary. *IEEE Trans. Ind. Appl.* 2015, 51, 3343-3360.

[6] B. Sarlioglu, C. Morris. *IEEE Trans. Transport. Elecrific.* 2015, 1, 54-64.

[7] M. Shamseh, I. Yuzurihara, A. Kawamura. *IEEE Trans. Power Electron.* 2016, 31, 6787-6791.

[8] B. Burger, D. Kranzer. *13th European Conference on Power Electronics and Applications* 2009, 1-13.

[9] Yole Developpement. “Power SiC 2020: Materials, Devices and Applications” 2020.

[10] J. Berzelius. *Annalen der Physik* 1824, 77, 169-230.

[11] A. Acheson. *British Patent* 1892, No. 17: 911.

[12] J.A. Lely. *Ber. Deut. Keram. Ges.* 1955, 32, 229.

[13] Y.M. Tairov, V. Tsvetkov. *J. Cryst. Growth* 1978, 43, 209-212.

[14] D.L. Barrett, J.P. McHugh, H.M. Hobgood, R.H. Hopkins, P.G. McMullin, R.C. Clarke, W.J. Choyke. *J. Cryst. Growth* 1993, 128, 358-362.

[15] H. Li, X.L. Chen, D.Q. Ni, X. Wu. *J. Cryst. Growth* 2003, 258, 100-105.

[16] H. Li, X.L. Chen, D.Q. Ni, X. Wu. *Diam. Relat. Mater.* 2004, 13, 151-156.

[17] N. Ohtani, T. Fujimoto, M. Katsuno, T. Aigo, H. Yashiro. *J. Cryst. Growth* 2002, 237-239, 1180-1186.

[18] A. Ellison, B. Magnusson, B. Sundqvist, G. Poxina, J.P. Bergman, E. Janzen. *Mater. Sci. Forum* 2004, 457, 9-14.

[19] Y. Kitou, E. Makino, K. Ikeda, M. Nagakubo, S. Onda. *Mater. Sci. Forum* 2006, 527, 107-110.

[20] N. Hoshino, I. Kamata, Y. Tokuda, E. Makino, N. Sugiyama, J. Kojima. *Appl. Phys. Express* 2014, 7, 065502.

[21] G.B. Stringfellow. *J. Cryst. Growth* 1991, 115, 1-4.

[22] D.H. Hofmann, M.H. Muller. *Mater. Sci. Eng. B* 1999, 61-62, 29-39.

[23] Y.M. Tairov, N.S. Peev, N.A. Smirnova, A.A. Kalnin. *Cryst. Res. Tech.* 1986, 21, 1509-1515.

[24] M. Syvajarvi, R. Yakimova, E. Janzen. *J. Electrochem. Soc.* 1999, 146, 1565-1569.

[25] K. Kusunoki, S. Munetoh, K. Kamei, M. Hasebe, T. Ujihara, K. Nakajima. *Mater. Sci. Forum* 2004, 457-460, 123-126.

[26] T. Yoshikawa, S. Kawanishi, T. Tanaka. *Jpn. J. Appl. Phys.* 2010, 49, 051302.

[27] H. Daikoku, M. Kado, H. Sakamoto, H. Suzuki, T. Bessho, K. Kusunoki, N. Yashiro, N. Okada, K. Moriguchi, K. Kamei. *Mater. Sci. Forum* 2012, 717-720, 61-64.

[28] M. Syvajarvi, R. Yakimova, H.H. Radamson, N.T. Son, Q. Wahab, I.G. Ivanov, E. Janzen. *J. Cryst. Growth* 1999, 197, 147-154.

[29] M. Soueidan, G. Ferro, B. Nsouli, F. Cauwet, L. Mollet, C. Jacquier, G. Younes, Y. Monteil. *J. Cryst. Growth* 2006, 293, 433-437.

[30] Y. Yamamoto, S. Harada, K. Seki, A. Horio, T. Mistuhashi, D. Koike, M. Tagawa, T. Ujihara. *Appl. Phys. Express* 2014, 7, 065501.

[31] H. Tsuchida, R. Takanashi, I. Kamata, N. Hoshino, E. Makino, J. Kojima. *J. Cryst. Growth* 2014, 402, 260-266.

[32] S. Xiao, S. Harada, K. Murayama, M. Tagawa, T. Ujihara. *Cryst. Growth Des.* 2016, 16, 6436-6439.

[33] Y. Yamamoto, S. Harada, K. Seki, A. Horio, T. Mitsuhashi, T. Ujihara. *Appl. Phys. Express* 2012, 5, 115501.

[34] K. Murayama, T. Hori, S. Harada, S. Xiao, M. Tagawa, T. Ujihara. *J. Cryst. Growth* 2017, 468, 874-878.

[35] M.N. Khan, S. Nishizawa, K. Arai. *J. Cryst, Growth* 2003, 254, 137-143.

[36] O. Filip, B. Epelbaum, M. Bickermann, A. Winnacker. *J. Cryst. Growth* 2004, 271, 142-150.

[37] K. Kusunoki, K. Kamei, N. Okada, K. Moriguchi, H. Kaido, H. Daikoku, M. Kado, K. Danno, H. Sakamoto, T. Bessho, T. Ujihara. *Mater. Sci. Forum* 2014, 778-780, 79-82.

[38] K. Danno, S. Yamaguchi, H. Kimoto, K. Sato, T. Bessho. *Mater. Sci. Forum* 2016, 858, 19-22.

[39] C. Zhu, W. Yu, K. Suzuki, Y. Dang, T. Furusho, S. Harada, M. Tagawa, T. Ujihara. *13th European Conference on Silicon Carbide and Related Materials (ECSCRM2020)* 2021.

[40] N. Komatsu, T. Mitani, Y. Hayashi, T. Kato, S. Harada, T. Ujihara, H. Okumura. *J. Cryst. Growth* 2017, 458, 37-43.

[41] T. Shirai, K. Danno, A. Seki, H. Sakamoto, T. Bessho. *Mater. Sci. Forum* 2014, 778-780, 75-78.

[42] H. Daikoku, M. Kado, A. Seki, K. Sato, T. Bessho, K. Kusunoki, H. Kaidou, Y. Kishida, K. Moriguchi, K. Kamei. *Cryst. Growth Des.* 2016, 16, 1256-1260.

[43] M. Kado, H. Daikoku, H. Sakamoto, H. Suzuki, T. Bessho, N. Yashiro, K. Kusunoki, N. Okada, K. Moriguchi, K. Kamei. *Mater. Sci. Forum* 2013, 740-742, 73-76.

[44] K. Kusunoki, N. Okada, K. Kamei, K. Moriguchi, H. Daikoku, M. Kado, H. Sakamoto, T. Bessho, T. Ujihara. *J. Cryst. Growth* 2014, 395, 68-73.

[45] Y. Kim, S. Choi, Y. Shin, S. Jeong, M. Lee, C. Lee, J. Choi, M. Park, Y. Jang, W. Lee. *Mater. Sci. Forum* 2018, 924, 47-50.

[46] T. Horiuchi, L. Wang, A. Sekimoto, Y. Okano, T. Yamamoto, T. Ujihara, S. Dost. *Cryst. Res. Technol.* 2019, 54, 1900014.

[47] M. Ha, Y. Yu, Y. Shin, S. Bae, M. Lee, C. Kim, S. Jeong. *RSC Adv.* 2019, 9, 26327.

[48] F. Mercier, S. Nishizawa. *Jpn. J, Appl. Phys.* 2011, 50, 035603.

[49] J. Lefebure, J. Dedulle, T. Ouisse, D. Chaussende. *Cryst. Growth Des.* 2012, 12, 909-913.

[50] T. Umezaki, D. Koike, S. Harada, T. Ujihara. *Jpn. J. Appl. Phys.* 2016, 55, 125601.

[51] B. Liu, Y. Yu, X. Tang, B. Gao. *J. Cryst. Growth* 2019, 527, 125248.

[52] Y. Mukaiyama, M. Iizuka, A. Vorob'ev, V. Kalaev. *J. Cryst. Growth* 2017, 475, 178-185.

[53] S. Kawanishi, H. Daikoku, H. Shibata, T. Yoshikawa. *J. Cryst. Growth* 2021, 576, 126382.

[54] K. Suzuki, T. Taishi. *Jpn. J. Appl. Phys.* 2020, 59, 025504.

[55] D. Nakamura, I. Gunjishima, S. Yamaguchi, T. Ito, A. Okamoto, H. Kondo, S. Onda, K. Takatori. *Nature* 2004, 430, 1009-1012.

[56] S. Ha, P. Mieszkowski, M. Skowronski, L.B. Rowland. *J. Cryst. Growth* 2002, 244, 257-266.

[57] S. Harada, Y. Yamamoto, K. Seki, A. Horio, T. Mitsuhashi, M. Tagawa, T. Ujihara. *APL Mater.* 2013, 1, 022109.

[58] X. Liu, C. Zhu, S. Harada, M. Tagawa, T. Ujihara. *CrystEngComm* 2019, 21, 7260-7065.

[59] E. Bauser, H.P. Strunk. *J. Cryst. Growth* 1984, 69, 561-580.

[60] T. Nishinaga, C. Sasaoka, K. Pak. *Jpn. J. Appl. Phys.* 1989, 28, 836-840.

[61] T. Nishinaga. *Cryst. Res. Technol.* 2013, 48, 200-207.

[62] A.A. Chernov. *Modern Crystallography III*, Springer, 1984.

[63] A.A. Chernov. *J. Cryst. Growth* 1992, 118, 333-347.

[64] A.A Chernov, S.R. Coriell, B.T. Murray. *J. Cryst. Growth* 1993, 132, 405-413.

[65] S.R. Coriell, B.T. Murray, A.A. Chernov, G.B. McFadden. *J. Cryst. Growth* 1996, 169, 773-785.

[66] C. Zhu, S. Harada, K. Seki, H. Zhang, H. Niinomi, M. Tagawa, T. Ujihara. *Cryst. Growth Des.* 2013, 13, 3691-3696.

[67] K. Kakimoto, B. Gao. *Handbook of Crystal Growth, second ed.*, Elsevier, Boston, 2015, 845-870.

[68] T. Tsukada. *Handbook of Crystal Growth, second ed.*, Elsevier, Boston, 2015, 871-907.

[69] D. Vizman. *Handbook of Crystal Growth, second ed.*, Elsevier, Boston, 2015, 909-950.

[70] P. Capper, E. Zharikov. *Handbook of Crystal Growth, second ed.*, Elsevier, Boston, 2015, 951-993.

[71] J.J. Derby. *Prog. Cryst. Growth Charact. Mater.* 2016, 62, 286-301.

[72] F. Mercier, J. Dedulle, D. Chaussende, M. Pons. *J. Cryst. Growth* 2010, 312, 155-163.

[73] K. Ariyawong. *Doctoral dissertation*. Grenoble Alpes University 2015.

[74] T. Yamamoto, Y. Okano, T. Ujihara, S. Dost. *J. Cryst. Growth* 2017, 470, 75-88.

[75] K. Ariyawong, J. Dedulle, D. Chaussende. *Mater. Sci. Forum* 2014, 778-780, 71-74.

[76] F. Mercier, S. Nishizawa. *J. Cryst. Growth* 2011, 318, 385-388.

[77] T. Yamamoto, N. Adkar, Y. Okano, T. Ujihara, S. Dost. *J. Cryst. Growth* 2017, 474, 50-54.

[78] L. Wang, T. Horiguchi, A. Sekimoto, Y. Okano, T. Ujihara, S. Dost. *J. Cryst. Growth* 2019, 520, 72-81.

[79] M. Ha, Y. Shin, M. Lee, C. Kim, S. Jeong. *Phys. Status Solidi. A* 2018, 215, 1701017.

[80] M. Ha, Y. Shin, S. Bae, S. Park, S. Jeong. *J. Korean Ceram. Soc.* 2019, 56, 589-595.

[81] T. Park, Y. Shin, M. Ha, S. Bae, Y. Lim, S. Jeong. *J. Korean Inst. Electr. Electron. Mater. Eng.* 2019, 32, 522-527.

[82] Y. Kim, S. Choi, Y. Shin, S. Jeong, M. Lee, C. Lee, J. Choi, M. Park, Y. Jang, W. Lee. *Mater. Sci. Forum* 2018, 924, 47-50.

[83] K. Fujii, K. Takei, M. Aoshima, N. Senguttuvan, M. Hiratani, T. Ujihara, Y. Matsumoto, T. Kato, K. Kurashige, H. Okumura. *Mater. Sci. Forum* 2015, 821-823, 35-38.

[84] K. Kusunoki, K. Kamei, N. Okada, N. Yashiro, A. Yauchi, T. Ujihara, K. Nakajima. *Mater. Sci. Forum* 2006, 527-529, 119-122.

[85] L. Wang, T. Horiguchi, A. Sekimoto, Y. Okano, T. Ujihara, S. Dost. *J. Cryst. Growth* 2018, 498, 140-147.

[86] M. Ha, L. Lich, Y. Shin, S. Bae, M. Lee, S. Jeong. *Materials* 2020, 13, 651.

[87] K. Kurashige, M. Aoshima, K. Takei, K. Fujii, M. Hiratani, N. Senguttuvan, T. Kato, T. Ujihara, Y. Matsumoto, H. Okumura. *Mater. Sci. Forum* 2015, 821-823, 22-25.

[88] X. Liu, P. Bennema. *J. Cryst. Growth* 1994, 139, 179-189.

[89] A.A. Chernov. *Sov. Phys. Usp.* 1961, 4, 116-148.

[90] H. Lin, P.G. Vekilov, F. Rosenberger. *J. Cryst. Growth* 1996, 158, 552-559.

[91] P.G. Vekilov, H. Lin, F. Rosenberger. *Phys. Rev. E* 1997, 55, 3202-3214.

[92] Y. Kwon, J.J. Derby. *J. Cryst. Growth* 2001, 230, 328-335.

[93] M. Inaba, M. Sato. *J. Phys. Soc. Jpn.* 2011, 80, 074606.

[94] M. Inaba, M. Sato. *J. Phys. Soc. Jpn.* 2012, 81, 064601.

[95] X. Liu, Y. Dang, K. Suzuki, C. Zhu, W. Yu, S. Harada, M. Tagawa, T. Ujihara. *J. Cryst. Growth* 2022, 578, 126425.

[96] N. Dropka, M. Holena. *Crystals* 2020, 10, 663.

[97] Y. Tsunooka, N. Kokubo, G. Hatasa, S. Harada, M. Tagawa, T. Ujihara. *CrystEngComm* 2018, 20, 6546.

[98] W. Yu, C. Zhu, Y. Tsunooka, W. Huang, Y. Dang, K. Kutsukake, S. Harada, M. Tagawa, T. Ujihara. *CrystEngComm* 2021, 23, 2695-2702.

[99] L. Wang, A. Sekimoto, Y. Takehara, Y. Okano, T. Ujihara, S. Dost. *Crystals* 2020, 10, 791.

[100] T. Horiuchi, L. Wang, A. Sekimoto, Y. Okano, T. Ujihara, S. Dost. *J. Cryst. Growth* 2019, 517, 59-63.

[101] Y. Takehara, A. Sekimoto, Y. Okano, T. Ujihara, S. Dost. *J. Cryst. Growth* 2020, 532, 125437.

[102] Y. Takehara, A. Sekimoto, Y. Okano, T. Ujihara, S. Dost. *J. Therm. Sci. Technol.* 2021, 16, JTST0009.

2. Configurational instability of crucible and machine learning-based optimization

2.1 Introduction

In solution growth of SiC, the graphite crucible is employed as the container, heat source, and carbon source. This ingenious multi-function design greatly simplifies the system structure, and brings the TSSG method advantage in cost. On the other hand, however, the local dissolution and precipitation of carbon slowly but continuously alter the crucible shape, and make the growth deviate from the initially designed condition on a long-term scale. A method that can predict the dynamic changes of the growing system and adjust the control parameters accordingly is therefore required to consistently maintain the most suitable growth conditions. A dynamic controlling method like this is also desired for the growth of other crystals. Previous studies on growth recipe design and optimization have investigated inverse modeling algorithms to optimize the control parameters for a multi-timestep process [1-5]. Although successful in some specific cases, inverse modeling is not suitable for non-linear and multi-objective problems, thereby limiting its more general application. A few studies have also applied a genetic algorithm (GA) combined with CFD simulation for multi-variable process optimization [6, 7], but the whole growth process was divided into a very small number of timesteps (~3) due to the difficulties in obtaining large amounts of data to support the stochastic search of the GA. Generally speaking, recipes with a small number of timesteps may not adequately capture the dynamic characteristics of long-term growth, and consequently may not yield the “most optimal” result. Therefore, real-time prediction and optimization with a shorter timestep length are preferred, but this will greatly increase the required amount of data for the optimization algorithm. Computational fluid dynamics (CFD) simulation is a powerful research tool for exploring the extreme environment inside the crystal growth system through virtual space. However, crystal growth is a complex multi-physics process that requires time-consuming coupled calculations of fluid flow, heat transfer, mass transport, and magnetic field. Despite the advantages of modern computational power, the time cost of CFD simulations to provide sufficient data for the optimization algorithm remains too

high. Therefore, a method that offers high-speed data acquisition, for multi-timestep and even real-time optimization, is essential for crystal growth processing in both research and industry. The advent of machine learning technology has brought this goal closer to fruition. A well-trained machine learning model can learn the direct non-linear mapping relationship between specific input and output parameters for instant predictions. Machine learning has already been employed widely in the field of crystal growth as an alternative to CFD simulations, particularly for the optimization of growth conditions [7-11]. The solution growth of SiC crystals is a suitable example to discuss the effect of dynamic optimization and control because unsteady changes in the shape of the crystal and crucible surfaces during long-term growth affect the thermal, flow, and carbon concentration fields inside the solution. Numerous studies have been conducted over the last decade to increase the size and growth rate of SiC crystals in solution growth, but all of them have focused on improving or optimizing the initial steady state alone. The importance of long-term dynamic control has not yet been discussed in previous reports. It is considered that, even though a growth recipe with fixed control parameters is well-designed for the initial state, it may become non-optimal for the conditions after tens of hours, due to the unsteady changes. Instead, adaptive control for long-term SiC solution growth should be implemented to always maintain optimal growth conditions.

To address the problem and fulfill the requirement above, this chapter consists of the following contents.

1. A two-dimensional (2D) global numerical model is developed to investigate the evolution of unsteady factors during long-term solution growth of SiC crystal, and an original recipe with fixed control parameters is examined and the maximum available growth time is estimated;

2. A machine learning-based optimization is coupled with the simulation model to design a time-dependent recipe with a 100-timestep sequence to facilitate the growth of larger and flatter single crystals and to prolong available growth time;

3. A transfer learning method is applied to further improve the optimization efficiency and achieve real-time optimization.

2.2 Description of the numerical model

The configuration of the solution growth system for a 3-inch SiC crystal is shown in Fig. 2.1. Radiofrequency (RF) heating coils with a frequency of 3 kHz are used to heat and stir the solution. The temperature at the monitoring point is measured using a thermocouple and the heating power is adjusted to achieve the desired temperature. The furnace is filled with helium gas at a fixed pressure of 1 atm. The initial diameter and height of the solution are 120 and 30 mm, respectively, while the thickness of the

crucible side wall is 15 mm. The rod and crucible are able to move rotationally and vertically in an independent manner. The vertical distance between the crucible bottom and coil bottom is referred to as "the crucible position (ΔH)".

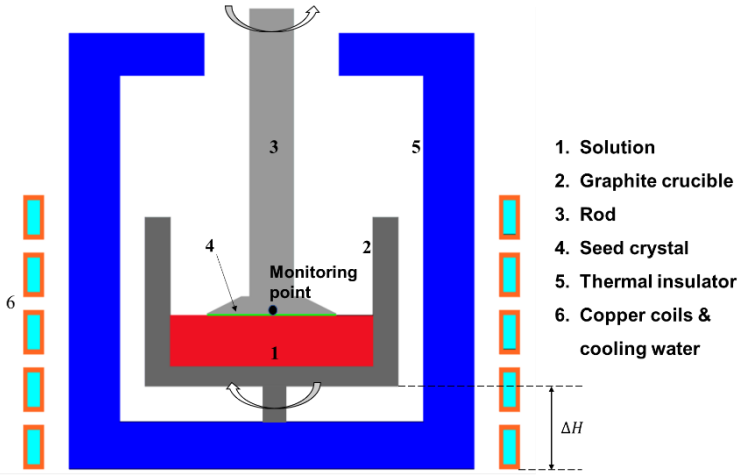

Fig. 2.1. Simplified configuration of a SiC crystal solution growth system

2.2.1 Assumptions and governing equations

A 2D global model is built to simulate the heat transfer and mass transport throughout the crystal growth process. For simplicity, several assumptions are made, namely, (1) the furnace is axisymmetric; (2) all radiative surfaces are diffuse gray; (3) the solution is incompressible and the Boussinesq approximation is obeyed; (4) the helium gas in the furnace is ideal and transparent, and it meets the low Mach number approximation; (5) the carbon concentration inside the solution is low enough to neglect solute convection; and (6) the SiC crystal growth is a slow and nearly thermodynamic equilibrium process, where each timestep can be considered as a steady state. Under these assumptions, the differential equations governing the fluid flow, heat transfer, and mass transport in the solution are given as follows:

$$\nabla \cdot (\rho \vec{u}) = 0 \qquad \text{(Eq. 2-1)}$$

$$\rho \vec{u} \cdot \nabla \vec{u} = -\nabla P + \mu \nabla^2 \vec{u} + (\rho - \rho_0)\vec{g} + \vec{F}_E \qquad \text{(Eq. 2-2)}$$

$$C_p \rho \vec{u} \cdot \nabla T = \nabla \cdot (\lambda \nabla T) + S_{RF} \qquad \text{(Eq. 2-3)}$$

$$\rho \vec{u} \cdot \nabla \omega = D \nabla^2 \omega \qquad \text{(Eq. 2-4)}$$

where ρ is the density, $\vec{u}$ is the velocity, P is the pressure, μ is the viscosity, ρ_0 is the reference density, $\vec{g}$ is the gravitational acceleration, $\vec{F}_E$ is the Lorentz force, C_p is the specific heat capacity, T is the temperature, λ is the thermal conductivity, S_{RF} is the inducted heat source, ω is the mass fraction of carbon, and D is the diffusivity of carbon

in solution. $\vec{F}_E$ and S_{RF} are determined by the electromagnetic field, which is calculated by:

$$\frac{\partial}{\partial r}\left(\frac{1}{r}\frac{\partial C_e}{\partial r}\right)+\frac{\partial}{\partial z}\left(\frac{1}{r}\frac{\partial C_e}{\partial z}\right)=\begin{cases}-\mu_e J_0 & \text{in the coil}\\ \frac{\mu_e\sigma_e\omega}{r}S_e & \text{in the conductor}\\ 0 & \text{in the non}-\text{condcutor}\end{cases} \quad \text{(Eq. 2-5)}$$

$$\frac{\partial}{\partial r}\left(\frac{1}{r}\frac{\partial S_e}{\partial r}\right)+\frac{\partial}{\partial z}\left(\frac{1}{r}\frac{\partial S_e}{\partial z}\right)=\begin{cases}0 & \text{in the coil}\\ -\frac{\mu_e\sigma_e\omega}{r}C_e & \text{in the conductor}\\ 0 & \text{in the non}-\text{condcutor}\end{cases} \quad \text{(Eq. 2-6)}$$

where C_e is the in-phase and S_e is the out-of-phase amplitudes of the magnetic stream function, r is the radial coordinate, z is the axial coordinate, μ_e is the magnetic permeability, J_0 is the peak value of electric current, and σ_e is the electrical conductivity. Accordingly, $\vec{F}_E$ and S_{RF} can be expressed as:

$$\vec{F}_E=\frac{\omega}{2\pi}\int_0^{\frac{2\pi}{\omega}}\vec{J}\times\vec{B}\,dt=\frac{\sigma_e\omega}{2r^2}\left(C_e\frac{\partial S_e}{\partial r}-S_e\frac{\partial C_e}{\partial r},0,C_e\frac{\partial S_e}{\partial z}-S_e\frac{\partial C_e}{\partial z}\right) \quad \text{(Eq. 2-7)}$$

$$S_{RF}=\frac{\omega}{2\pi}\int_0^{\frac{2\pi}{\omega}}\frac{{J_0}^2}{\sigma_e}\,dt=\frac{\sigma_e\omega}{2r^2}\left({C_e}^2+{S_e}^2\right) \quad \text{(Eq. 2-8)}$$

where $\vec{J}$ is the current density and $\vec{B}$ is the static magnetic field.

The differential equations above are solved numerically using the FVM (finite volume method) in CGSim commercial software [12]. The latent heat generated on the crystallization front is neglected because the growth rate is low (~0.1 mm/h). The physical properties of the Si-Cr solvent used in calculating the electric, thermal, flow, mass fields, as well as the free surface shape [13], are listed below.

Table 2.1 Physical properties of solvent used in the modeling [14-16]

Property	Value	Unit
Thermal conductivity (λ)	$-68.28+5.40\times10^{-2}T$	$W/(m\cdot K)$
Density (ρ)	$5199-0.55T$	kg/m^3
Heat capacity (C_p)	1196	$J/(kg\cdot K)$
Viscosity (μ)	$1.27\times10^{-3}\exp(1982/T)$	$Pa\cdot s$
Surface tension (σ)	$1.20-1.23\times10^{-4}T$	N/m
Electrical conductivity (σ_e)	$2.21\times10^{6}-2.80\times10^{9}/T$	S/m
Diffusion coefficient (D)	$7.55\times10^{-8}\exp(-1100/T)$	m^2/s
Contact angle (θ_s)	18	°

2.2.2 Boundary conditions for unsteady factors

The transport path of carbon in solution is initiated by the dissolution of carbon from the graphite crucible wall due to the undersaturated conditions as shown in Fig. 1.4(a). The dissolved carbon is transported to the surface of the seed crystal and the bottom of the crucible via the effects of both convection and diffusion. A single crystal grows on the seed crystal with the same orientation, while polycrystals freely form at the crucible bottom. These factors resulted in unsteady changes in the configuration inside the crucible.

SiC crystal growth.

The equilibrium mass fraction of carbon, ω_{eq}, is set as the boundary condition for carbon transport at the crystal–solution interface. The value of ω_{eq} is positively associated with the temperature. By elaborately controlling a relatively lower temperature at the single crystal surface, the carbon mass fraction at this interface is higher than the local ω_{eq}. This supersaturated carbon provides the driven force for single SiC crystallization, guided by the seed crystal. The temperature dependence of carbon solubility in the Si–Cr-based solution was determined by data assimilation using machine learning from a previous study [15]:

$$\omega_{eq} = exp(3.924 - 19255/T) \quad \text{(Eq. 2-9)}$$

The growth rate of the SiC crystal is determined by considering the carbon flux normal to the crystal surface. The carbon flux J can be calculated as

$$J = D\nabla\omega \cdot \vec{n} \quad \text{(Eq. 2-10)}$$

where $\vec{n}$ is the unit normal vector of the local crystal surface. Consequently, the growth rate V_g is obtained as

$$V_g = J\frac{M_{SiC}}{M_C\rho_{SiC}} \quad \text{(Eq. 2-11)}$$

and the displacement of the crystal $\Delta l_{crystal}$, can be expressed as

$$\Delta l_{crystal} = V_g\Delta t \quad \text{(Eq. 2-12)}$$

where M_{SiC} is the molecular weight of SiC, M_C is the molecular weight of carbon, ρ_{SiC} is the density of the SiC single crystal, and Δt is the assumed timestep length for unsteady changes. The displacement obtained from Eq. 2-12 for a specific timestep is used to update the geometrical shape of the crystal surface for the subsequent time step.

Graphite crucible dissolution.

Same as the crystal–solution interface, ω_{eq} is set as the boundary condition at the crucible–solution interface. The solution–crucible interface typically exhibits the highest

temperature in the solution domain, as well as an undersaturated condition where the local carbon mass fraction is below the local ω_{eq}. The undersaturation results in the dissolution of graphite crucible with a dissolution rate V_d, expressed based on the carbon flux normal to the crucible–solution interface, J, as

$$V_d = J/\rho_C \quad \text{(Eq. 2-13)}$$

Similarly, the displacement of the crucible wall, $\Delta l_{crucible}$, can be obtained as

$$\Delta l_{crucible} = V_d \Delta t \quad \text{(Eq. 2-14)}$$

The shape change of the crucible wall strongly influences the temperature distribution and convection pattern inside the solution, thereby affecting the stability. Moreover, the dissolution of the crucible wall leads to an increasing risk of cracking under high-speed rotation of the crucible, thereby limiting the maximum available growth time. Therefore, the crucible dissolution must be controlled.

SiC polycrystal precipitation.

Polycrystals often precipitate within the solution in high supersaturation areas other than the seed crystal [17, 18], such as at the crucible bottom (see Fig. 1.4(b)). Polycrystals grow from spontaneous nucleation and do not follow a specific crystal orientation. Therefore, the movement of polycrystals surface is faster than that of the single crystal [19]. Moreover, polycrystals comprise many solvent inclusions that also accelerate the precipitation but make it difficult to simulate. The exact composition and precipitation process of SiC polycrystals have not been previously reported. Therefore, this study makes two assumptions, namely (1) the polycrystals and the single crystal have the same material properties in CFD simulation, and (2) the precipitation rate of the polycrystals, V_h, is proportional to the growth rate of the single crystal. V_h is assumed to be expressed as

$$V_h = \alpha J \frac{M_{SiC}}{M_C \rho_{SiC}} \quad \text{(Eq. 2-15)}$$

where α is a constant with a value of 1.9 based on the fitting of experimental data.

The formation of polycrystals enhances the downward heat dissipation due to their higher thermal conductivity than graphite crucible and will influence the thermal field. Moreover, the heavy precipitation of polycrystals during long-term growth can lead to the collision with the growing single crystal and cause severe damage. Therefore, the precipitation of polycrystals limits the maximum available growth time and should be suppressed.

2.3 Simulation of the long-term growth with a fixed recipe

An original recipe with fixed parameters has been used in previous experiments, and successfully yielded a 3-inch SiC crystal with 1.5 mm thickness after 15 h growth. As shown in Fig. 2.2, the smooth surface morphology suggests a suitable growth condition achieved by the original recipe, at least in the first 15 h. This recipe involved heating of the monitoring point to 2213 K at the beginning of the crystal growth process. Once this temperature was achieved, the heating power and other control parameters were fixed until the end of growth. The detailed values of the controlling parameters can be found in Table 2.2.

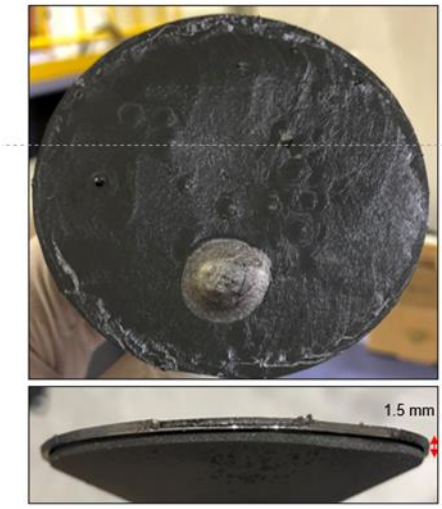

Fig. 2.2 Crystal grown under the original fixed recipe

Table 2.2 Control parameters in the original recipe

Parameters	Value
Heating power, P (kW)	7.5
Crucible position, ΔH (mm)	70
Rod rotation speed, ω_{rod} (rpm)	50
Crucible rotation speed, $\omega_{crucible}$ (rpm)	0

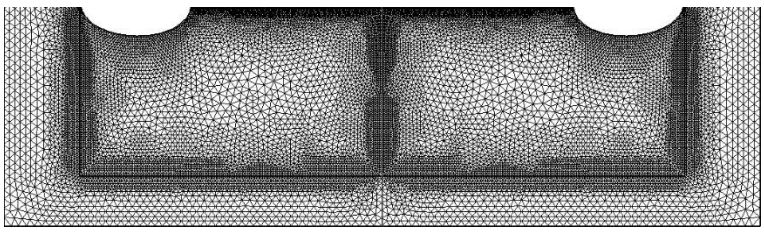

(a) Mesh structure at 0 h

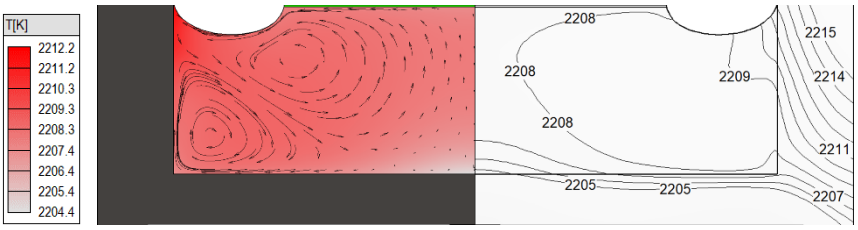

(b) Thermal and flow fields at 0 h

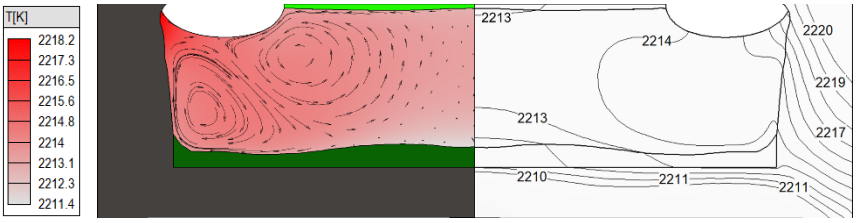

(c) Thermal and flow fields at 10 h

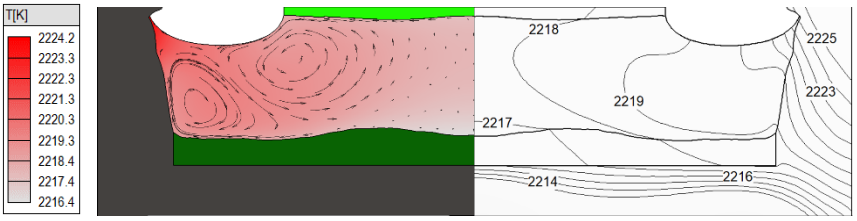

(d) Thermal and flow fields at 20 h

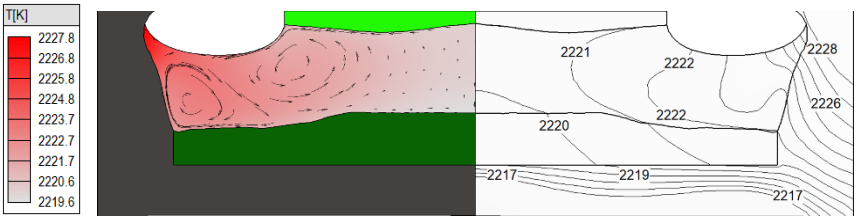

(e) Thermal and flow fields at 30 h

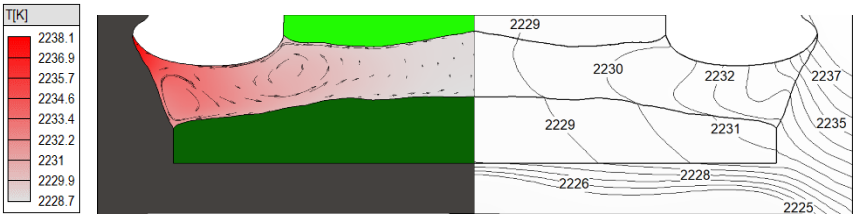

(f) Thermal and flow fields at 40 h

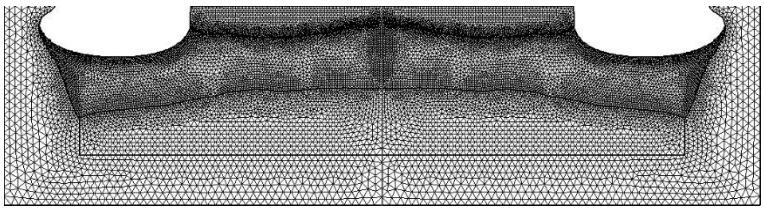

(g) Mesh structure at 40 h

Fig. 2.3 Evolution of thermal and flow fields inside the crucible (b-f), as well as the mesh structure (a,g). Red, light green, dark green, and dark gray represent the solution, single crystal, polycrystals, and crucible, respectively.

The numerical model introduced in the last section is then conducted to investigate the capability of this original fixed recipe for long-term growth. The evolution of the temperature and velocity fields inside the solution domain in a total 50 h growth process is shown in Fig. 2.3, which revealed three trends. Firstly, the maximum temperature inside the solution increases with time. This can be explained that a thinner crucible wall due to dissolution has weaker electromagnetic shielding effect on the solution, and therefore more Joule heat is inducted inside the solution. Consequently, the maximum temperature of the solution increased by 26 K after 50 h. Secondly, although the maximum temperature inside the solution increases, the single crystal surface becomes colder relative to the crucible wall. This is attributed to the enhanced downward heat dissipation due to the polycrystals precipitating at the bottom of the crucible. This increases the supersaturation near the crystal surface, thereby accelerating the crystal growth. Thirdly, the convection in the solution is strong at the beginning of the crystal growth process, which plays an important role in heat transfer and carbon transport. However, the convection is weakened due to the decrease in the solution volume as the growth proceeded, which hinders heat and carbon transport to the center of the crystal surface. This may cause non-uniformity in the growth rate on the crystal surface. These trends indicate the instability caused by configuration change inside the solution during long-term growth.

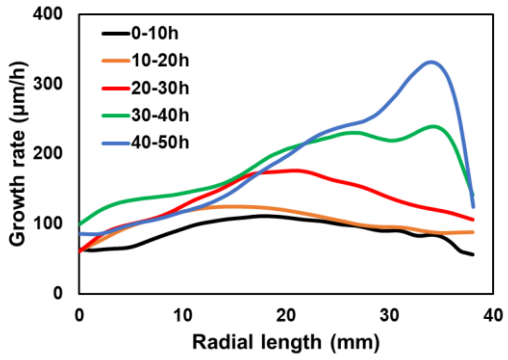

(a)

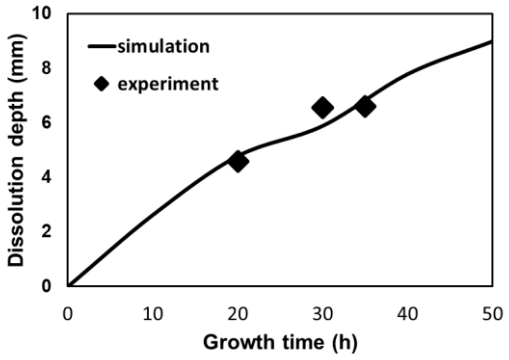

(b)

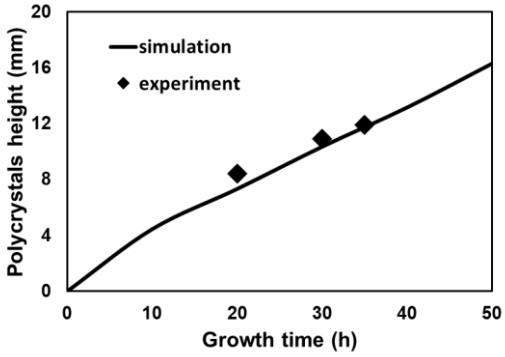

(c)

Fig. 2.4 Evolution of the (a) crystal growth rate, (b) maximum crucible dissolution depth, and (c) maximum height of the polycrystals under the fixed recipe.

The time variation is evaluated on the three most important surfaces, namely the single crystal growth front, crucible wall, and polycrystal surface (Fig. 2.4). At the beginning of the growth process, the growth rate is relatively uniform across the crystal surface (Fig. 2.4(a)). However, both the maximum value and non-uniformity of the growth rate increase as the growth proceeds, where the highest growth rate area gradually moves towards the edge. After 50 h growth, the growth rate becomes very non-uniform, where the maximum value is more than triple the minimum value. As for the maximum dissolution depth of the crucible wall (Fig. 2.4(b)) and the maximum height of polycrystals (Fig. 2.4(c)), they both linearly correlate to the growth time, and correspond well with the experimental data, which proves the reliability of the numerical model. After 50 h growth (will be shown later in Fig. 2.11), the average thickness of the single crystal is 7.23 mm, but quality issues (e.g., polytypes and inclusions) may arise locally due to the high and non-uniform growth rate in the late period. The maximum dissolution depth of the crucible wall reaches ~9 mm after 50 h, which is 60% of the original thickness and indicates a high risk to crack. The maximum height of the polycrystals is ~17 mm after 50 h, where the distance between the single crystal and polycrystals is only ~5 mm. Continuing the growth will lead to collision between the rotating rod and the polycrystals in the next 10 h. Therefore, the maximum available growth time for this recipe is limited to ~50 h.

Overall, the original recipe with fixed control parameters is not capable of long-term solution growth due to instability issues and will limit the available growth time. Although higher initial solution height and thicker crucible wall may prolong the available growth time, they will increase the cost and cause other problems (e.g., turbulent flow). Therefore, the recipe should be adaptively and time-dependently designed to maintain suitable growth conditions and prolong the available growth time.

2.4 Optimization of a time-dependent recipe

The target of this section is to yield a time-dependent control recipe with a 100-time step sequence for the 50 h ($\Delta t = 0.5\ h$) growth process, to compare with the result in sec. 2.3. The whole optimization system consists of 3 parts: the CFD model to provide reliable training data, a machine learning model to fast predict the unsteady changes, and an optimization algorithm to locate the optimal condition. Details of the operation are introduced as follows.

2.4.1 Construction of machine learning model

As described in sec. 2.1, the main difficulty of process optimization is the high-speed acquisition of enough data to support the stochastic search of the optimization algorithm. Due to its superior ability in feature detection and fast response, the machine learning prediction model is employed in this study, to serve as an extension of CFD simulation and supply data to the optimization algorithm.

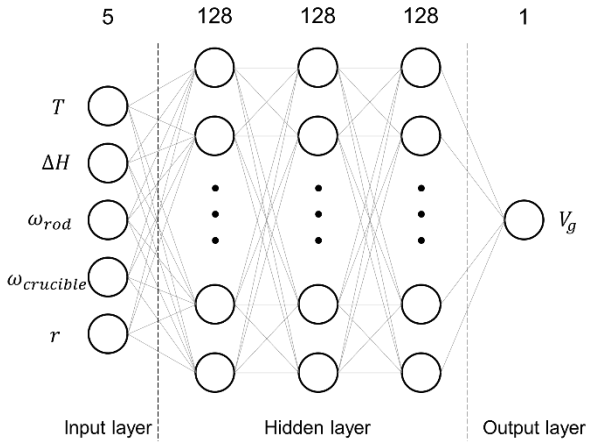

Fig. 2.5 Structure of the neural network for predicting the single crystal growth rate

In the present study, there are four main control parameters in the SiC solution growth system, namely the temperature at the monitoring point, the crucible position, the rotation speed of the crucible, and the rotation speed of the seed crystal. Here we dynamically control the temperature instead of the heating power to obtain a more stable thermal condition during the growth process. To explore the direct relationship between these control parameters and the three unsteady changes, three machine learning prediction models based on neural networks are independently constructed in each timestep. The input data for the neural networks includes the values of the four control parameters, as well as the coordinates of each grid point on the single crystal (150 points), crucible (60 points), or polycrystal surface (120 points) expressed as *r* in the radial direction or *z* in the vertical direction. The output is the growth rate or dissolution rate or precipitation rate at each point on each surface. The architecture of the neural network that predicts the single crystal growth rate is shown in Fig. 2.5 as an example. The network has 3 hidden layers and 128 neurons in each layer, determined by Optuna [20], a hyperparameter optimization framework. A sigmoid activation function is used, and the weights and bias are optimized using Adam [21], a method for stochastic optimization. The training data ranges for all timesteps are listed in Table 3.2. In each timestep, 120 steady-state CFD simulations with random control parameter combinations are conducted, and the relevant information for all points on the three

surfaces is extracted and prepared as training data. An additional 20 CFD simulations are prepared as test data to validate the prediction models.

Table 3.2 Training data ranges for machine learning

Parameters	Lower limit	Upper limit
Temperature, T (K)	2073	2273
Crucible position, ΔH (mm)	50	150
Rod rotation speed, ω_{rod} (rpm)	-50	50
Crucible rotation speed, $\omega_{crucible}$ (rpm)	-20	20

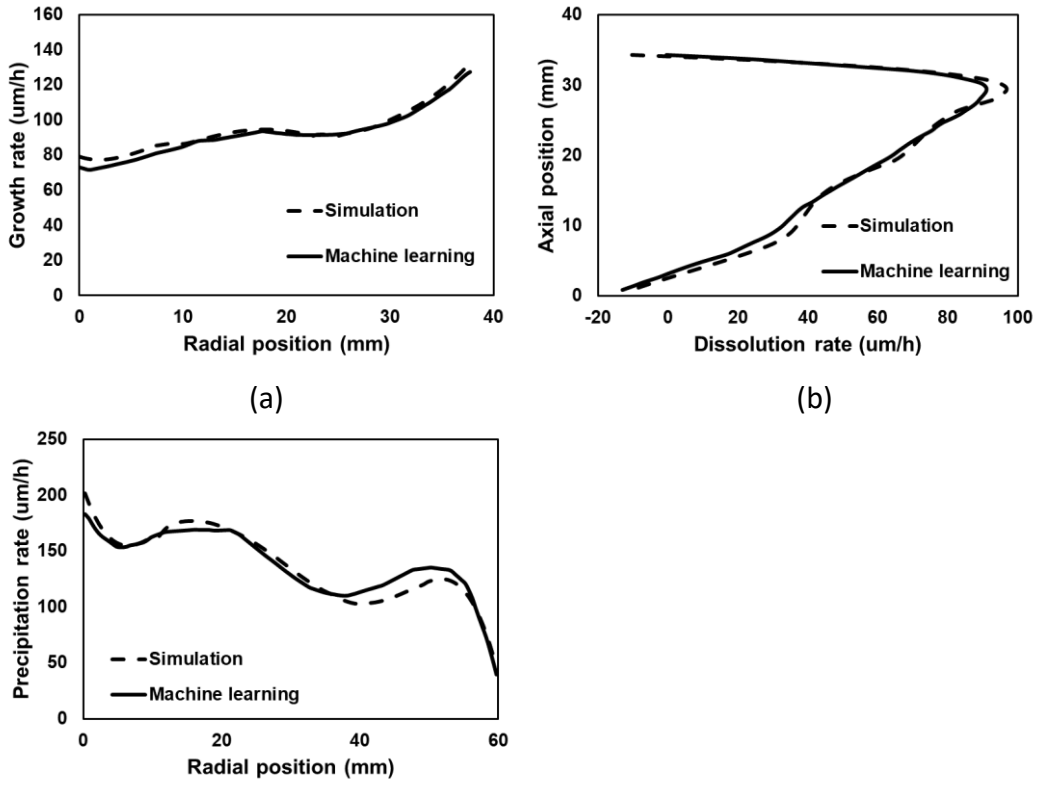

Fig. 2.6 Distribution of the (a) growth rate on the crystal surface, (b) dissolution rate on the crucible wall, and (c) precipitation rate of the polycrystals on the bottom of the crucible based on the CFD simulation and machine learning models, respectively. Note that the *y*-axis in (b) represents the vertical position on the crucible wall.

The performance of machine learning models in timestep 1 is shown in Fig. 2.6, as an example to illustrate the effectiveness of machine learning. For the crystal growth rate, crucible dissolution rate, and polycrystal precipitation rate, the machine learning prediction results match well with the simulation results. The correlation coefficients for

the test datasets are higher than 0.95 for all machine learning models across all 100 timesteps, thereby demonstrating their accuracy.

2.4.2 Optimization process

The operational flow of the adaptive control method is shown in Fig. 2.7. The well-trained machine learning models serve as data suppliers for the optimization algorithm to determine the most suitable combination of control parameters for the environment for each timestep. Non-dominated sorting genetic algorithm II (NSGA-II) is selected as the optimization algorithm in this study, due to its superior ability to solve multi-objective problems [22]. The objectives representing the optimal growth conditions are (1) maximizing the average crystal growth rate to enhance the production efficiency; (2) minimizing the standard deviation of the crystal growth rate to obtain a uniform crystal surface; and (3 & 4) minimizing the maximum crucible dissolution rate and polycrystal precipitation rate for a longer growth time and more stable growth conditions. Among all candidates suggested by NSGA-II, the individual with the best performance for all four objectives is selected as the optimal conditions for each timestep. The geometric model is then updated according to the unsteady changes under this optimal condition, and the above process is repeated for the subsequent timestep until the end of the process.

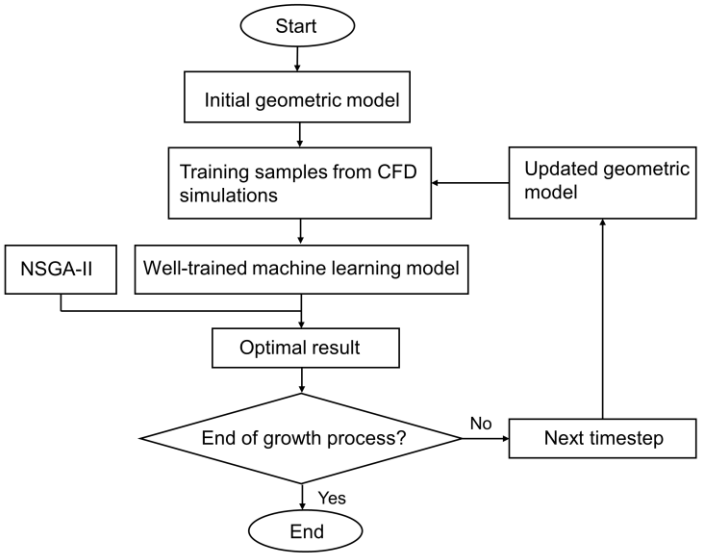

Fig. 2.7 Operation flow of the optimization process

It is worth mentioning that for the whole 100 timestep process, approximately 4×10^6 sets of inputs and outputs are required by NSGA-II due to the stochastic nature of the algorithm. It takes more than 1600 years to generate this dataset by experiments through one TSSG furnace. By CFD simulations alone, it still requires approximately four

years of CPU time with the state-of-art computational power used in this study. However, this value is only ~100 h to prepare all the training data to construct the machine learning models in 100 timesteps with acceptable accuracy, while the well-trained machine learning models cost almost no time to do the prediction and supply data to NSGA-II. This demonstrates the high efficiency of the utilization of machine learning models, and the potential for real-time optimization in the future.

2.4.3 Optimized time-dependent recipe

The times-dependent control parameters for the 100 timestep process suggested by the optimization algorithm are compared to the original fixed control parameters (Fig. 2.8). Several trends can be observed, namely, (1) the crucible position initially increases, and then remains high; (2) the temperature at the monitoring point remains at the lower limit of the data range during the entire growth process; (3) the seed crystal initially rotates at a high speed, and gradually slows down; and (4) the rotation speed of the crucible increases, especially in the late period. These trends indicate the dynamic feature of the optimized control recipe.

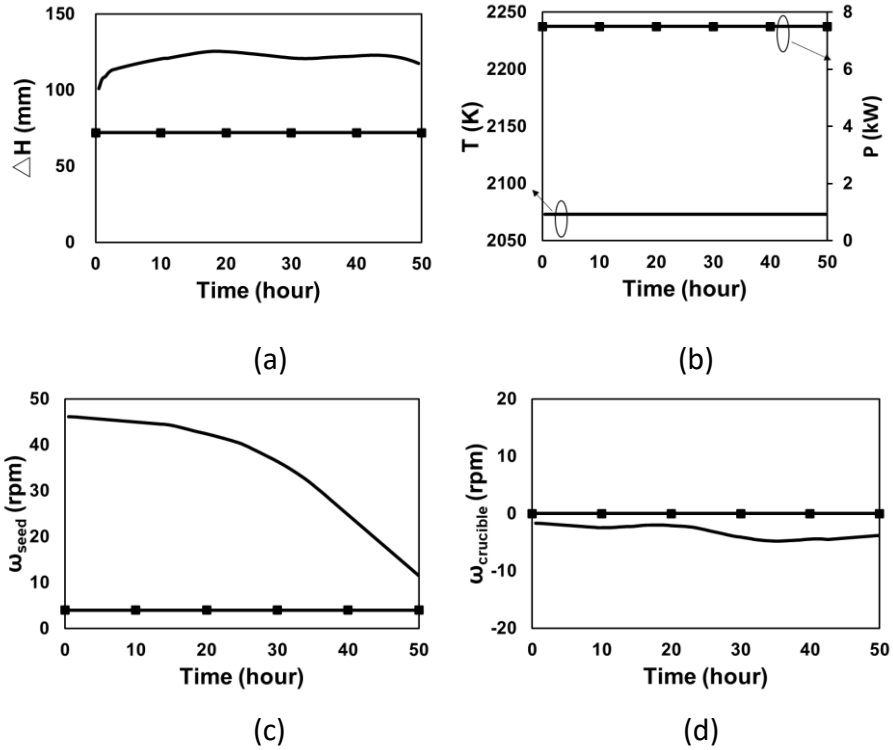

Fig. 2.8 Comparison of the control parameters in the fixed recipe and the adaptive recipe, namely the (a) crucible position, (b) temperature of the monitoring point, (c) rotation speed of the seed crystal, and (d) rotation speed of the crucible.

The evolution of the temperature and flow fields under the optimized recipe is plotted in Fig. 2.9, where the effective suppression of both crucible dissolution and polycrystal precipitation is achieved owing to the dynamic and adaptive control. Specifically, there is a smaller change in the maximum temperature of the solution ($T_{max\_solution}$). Moreover, the values of the maximum temperature difference between the single crystal and crucible wall ($\Delta T_{cry/cru}$), the temperature difference between the center and edge of the crystal surface ($\Delta T_{crystal}$), and the carbon mass fraction difference between the center and edge of the crystal surface ($\Delta\omega_{crystal}$) are smaller compared with those of the fixed control growth process. This is indicative of more stable and preferable growth conditions. Detailed values of these parameters are listed in Table 2.3.

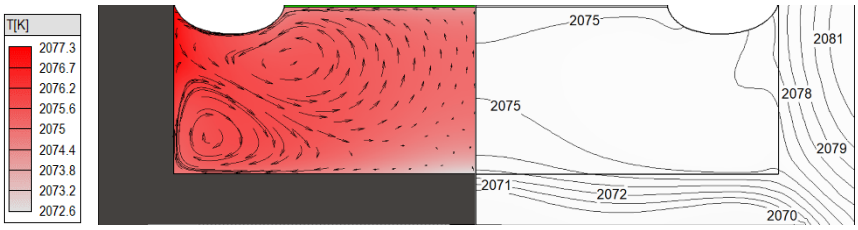

(a) Thermal and flow fields at 0 h

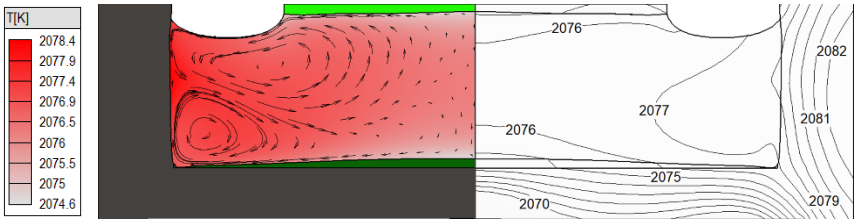

(b) Thermal and flow fields at 10 h

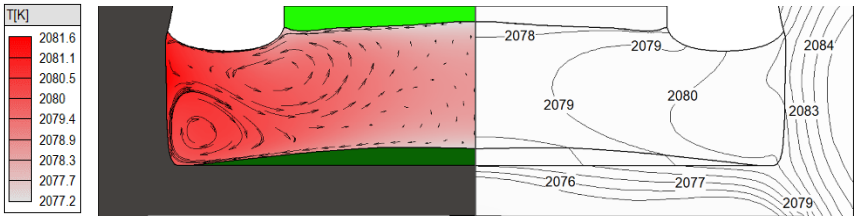

(c) Thermal and flow fields at 20 h

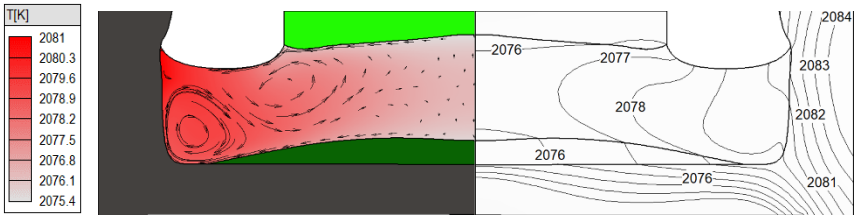

(d) Thermal and flow fields at 30 h

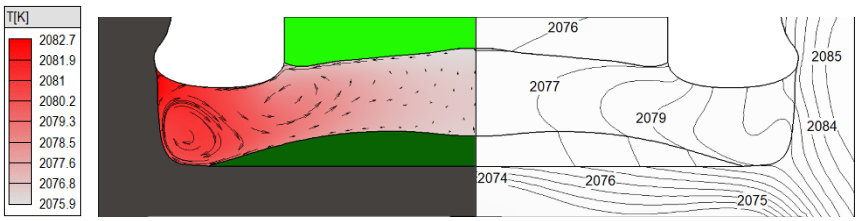

(e) Thermal and flow fields at 40 h

Fig. 2.9 Evolution of the thermal and velocity field in the solution domain under the adaptive recipe.

Table 2.3 Parameters during 50 h growth under the fixed and adaptive recipes

Time	$T_{max\_solution}$ (K)		$\Delta T_{cry/cru}$ (K)		$\Delta T_{crystal}$ (K)		$\Delta\omega_{crystal}$ ($\times10^{-5}$)	
	Fixed	Adaptive	Fixed	Adaptive	Fixed	Adaptive	Fixed	Adaptive
0 h	2212.2	2077.3	4.4	3.2	0.5	0.3	1.2	0.8
10 h	2218.2	2078.4	5.4	3.6	0.6	0.4	1.9	1.0
20 h	2224.2	2081.6	6.6	4.4	0.7	0.6	2.3	1.3
30 h	2227.8	2081.0	7.6	5.6	0.8	0.8	2.8	1.7
40 h	2238.1	2082.7	9.2	6.8	0.9	0.9	3.0	1.9

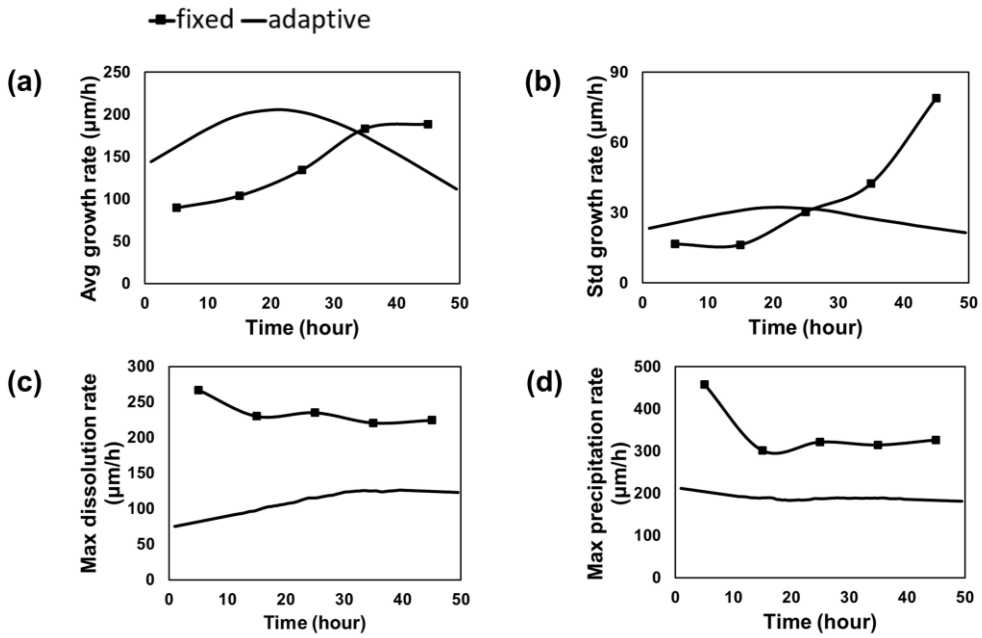

Fig. 2.10 (a) Average single crystal growth rate, (b) standard deviation of the single crystal growth rate, (c) maximum crucible dissolution rate, and (d) maximum polycrystals precipitation rate during the 50 h growth process.

To further illustrate the effectiveness of the optimization, the evolution of the four objectives, namely, average crystal growth rate, standard deviation of the crystal growth

rate, maximum crucible dissolution rate, and polycrystals precipitation rate during the entire growth process is evaluated in Fig. 2.10. For the growth under the fixed recipe, the average crystal growth rate increases with time, but is accompanied by an almost exponential increase in standard deviation. This represents that the growth is out of control in the late period. Conversely, the crystal growth rate under the adaptive recipe exhibits a high average value at the beginning and a low standard deviation in the later periods. Besides, the adaptive recipe also allows for a much lower crucible dissolution rate and polycrystals precipitation rate.

Finally, the solution domain configurations of the two recipes are compared after 50 h in Fig. 2.11. The adaptive recipe can yield a ~30% thicker crystal (average thickness = 9.27 mm) with a flatter surface compared to the fixed recipe, as well as ~50% less crucible dissolution (maximum depth = 4.82 mm) and ~50% less polycrystal precipitation (maximum height = 8.28 mm). It is estimated that 50% more growth time (25 h) with stable and safe growth conditions is available. Overall, adjusting the growth recipe to adapt to the unsteady environmental changes during long-term growth offers superior control of the growth process and allows for higher production efficiency, better surface flatness, and longer available growth time.

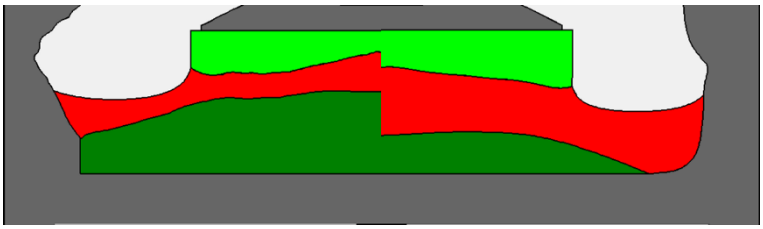

Fig. 2.11 Solution domain configuration after 50 h under the fixed (left) and adaptive (right) recipes. Red, light green, dark green, and dark gray represent the solution, single crystal, polycrystals, and crucible, respectively.

2.5 Discussion on improving optimization efficiency

Although the optimization system proposed in the last section has proven its effectiveness in yielding a time-dependent control recipe, the time-consuming process of making enough training data for machine learning still limits the optimization efficiency and its wider application. It takes about 100 h CPU time for the whole process to prepare sufficient training data for the optimization of a 50-hour growth sequence. Since the ultimate target of this study is to construct a “digital twin” of the practical experiment and achieve real-time control and optimization, the efficiency of the foregoing system should be further improved by reducing the training data number, but meanwhile keep the high accuracy of machine learning. However, there seems to be a tradeoff between the training data size and model accuracy, because previous material

informatics studies have unambiguously demonstrated that with less training data set it will be more difficult for the machine learning model to detect the pattern and make accurate prediction [23-25].

Thanks to the development of machine learning technology, a method named transfer learning might be the solution to this dilemma. As the last part of this chapter, the present section examines the feasibility of applying transfer learning to the established system to further improve the optimization efficiency. Detailed performance regarding the effects of training data number and multi-step stability is discussed as follows. The determination of transfer method, training process, and the limit of transfer learning are introduced in Appendix A.

2.5.1 Transfer learning

As introduced previously, the artificial neural network detects the features of the dataset by adjusting the weights and bias between neurons in the network. Normally, a neural network is trained from an initial condition with given or random values of weights and bias (also referred to as “training from scratch”), and the required training data amount is positively correlated to the complexity of the dataset and the total number of neurons. For the datasets from two problems sharing sufficient similarities, their respective well-trained neural networks also have similar weights and bias distribution. Based on these facts, the concept of transfer learning was proposed [26, 27], which is to deploy the information from a well-trained network (source model) into a new one (transferred model) dealing with the similar problem, to offset the decrease of training data amount.

This approach works by firstly training a neural network model on the source domain with sufficient training data size and then, as the name suggests, transferring the architecture and parameters of the source model into a related target domain and slightly adjusting the model with the new training data set. If the two domains share sufficiently similar features, this transfer can simplify the pattern detection process in the target domain and keep the high accuracy even with small data set. Two commonly applied procedures for neural transfer learning, namely the frozen featurizer and fine tuning, were considered [28, 29]. The source neural network with L layers can be represented as an Lth-order composite function tandemly arranged from input g_1 to output layer g_L:

$$Y_s = f_s(X) = (g_L \circ g_{L-1} \dots \circ g_1)(X) \quad \text{(Eq. 2-16)}$$

where Y and X are respectively the output and input of the model. It is generally considered that the shallow layers in the network tend to capture more general features, whereas the deep layers are more likely to capture specific features. Therefore, instead

of training the neural network from a random initial condition (training from scratch), the frozen featurizer method freezes the network variables in the shallower layers as a feature extractor, $\phi(X) = (g_K \circ g_{K-1} \dots \circ g_1)(X)$ with $K < L$, and conducts supervised learning on only the remaining layers to obtain a transferred model $Y_t = f_t(\phi(X))$. The fine tuning approach does not fix any layers from the source model, but instead treats the source model as the initial condition and then fine tunes the network variables at a small learning rate. This method updates the model to better fit the new task while preserving domain-invariant knowledge.

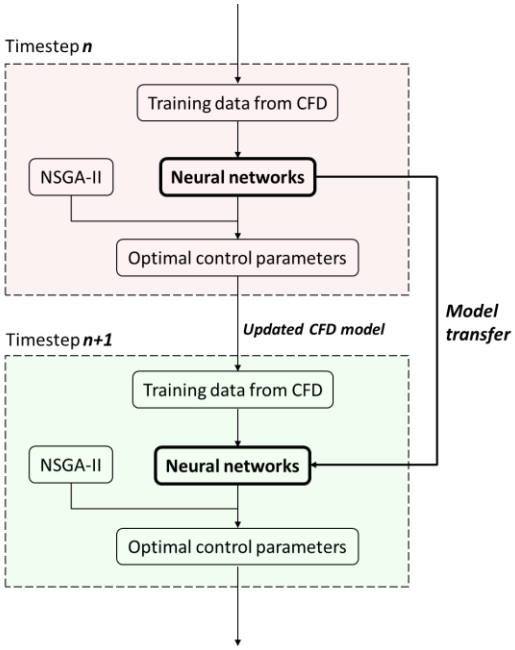

Fig. 2.12. Process flow of transfer learning and optimization of unsteady growth sequence

The strategy of transfer learning has been recently applied in the field of material informatics and has proven its effectiveness in predicting material properties [28, 30, 31], microstructure [32-34], and solar cell efficiency [35] from a small number of high-quality data. Therefore, it might be possible that transfer learning can be employed in our process design of unsteady crystal growth to save training data since the geometric evolutions between two consecutive timesteps are not significant and may not change the major features of input data representation. In the following sections, fine-tuning is selected as the only transfer method. The comparison between the performance of fine-tuning and frozen featurizer is described in detail in Appendix A. For fine-tuning, the learning rate is set as 0.0001, which is 100 times smaller than that when the source model is trained. “Early stopping” with patience of 10 iterations is used to avoid the influence of epoch number on different training cases, which will stop the training if the

validation error does not decrease in consecutive 10 iterations. The process flow of transfer learning and optimization of the unsteady growth sequence is shown in Fig. 2.12. In each timestep, instead of being constructed independently, the static neural networks inherit knowledge from the previous timestep, which enables the reduction of required training data from CFD simulation.

2.5.2 Performance of transfer learning on saving training data

The performances of the training-from-scratch model and the transferred model are then investigated under different training data amounts to further illustrate the superiority of the transfer learning model. The mean absolute error (MAE) of the output on the test set is selected to represent the performance of the model because it has the same unit as the output and can be evaluated more directly (the average growth rate in all data set is 206.0 μm/h, for reference). The data amount is expressed in a percentage form, which is the ratio of the number of training data cases to 140, the total number of data used to train the source model in timestep 1. As shown in Fig. 2.13, when using 100% amount of data, the new model and the transferred model both show relatively high accuracy and almost no difference in predicting the growth rate on the single crystal surface in the new timestep. However, when gradually decreasing the data amount, the trained-from-scratch model shows high sensitivity to the data amount and MAE increases almost exponentially along with the decrease of data. When the data size is less than 40%, the accuracy of the new model is already lower than directly using the source model from the initial timestep. The transferred model, in the contrast, remains high accuracy even with 20% amount of training data.

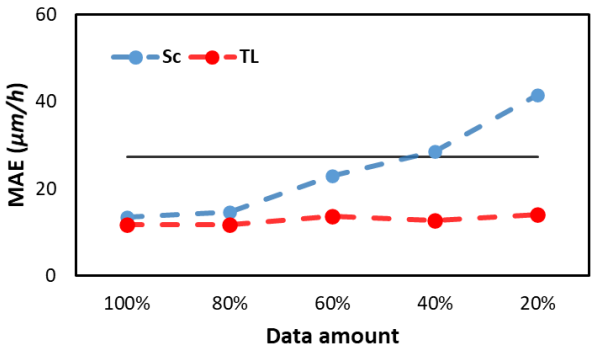

Fig. 2.13. Performance of transfer model and new model trained with different data amount. The solid black line is the MAE of directly applying the source model, as reference.

To further illustrate the effectiveness of transfer learning, the transferred models trained with only 20% amount of data are applied to predict the unsteady changes on

the three boundaries with a certain combination of control parameters. Note that this combination is not included in the training data set. The prediction results are compared with the performance of the new model trained with the same data amount. As shown in Fig. 2.14, for the growth rate of single crystal (Fig. 2.14(a)) and the precipitation rate of polycrystal at crucible bottom (Fig. 2.14(c)), the distributions predicted by transferred models show good agreements with the simulation result, while the predictions given by the new model can barely reproduce the approximate tendency, and cannot be used to supply data to the optimization algorithm in the subsequent process. In addition to proving the superiority of transferred models, an interesting result is observed when predicting the dissolution rate on the crucible wall (Fig. 2.14(b)). Beyond our expectation, the results given by the new model and the transferred model do not present as big a difference as shown on the other two boundaries. This can be explained that for the growth of the single crystal and the precipitation of polycrystal, they depend on the co-effect of both local temperature and overall solution flow pattern for carbon transport, while for the dissolution of crucible wall, it depends mainly on the local temperature, which may reduce the difficulty of feature detection.

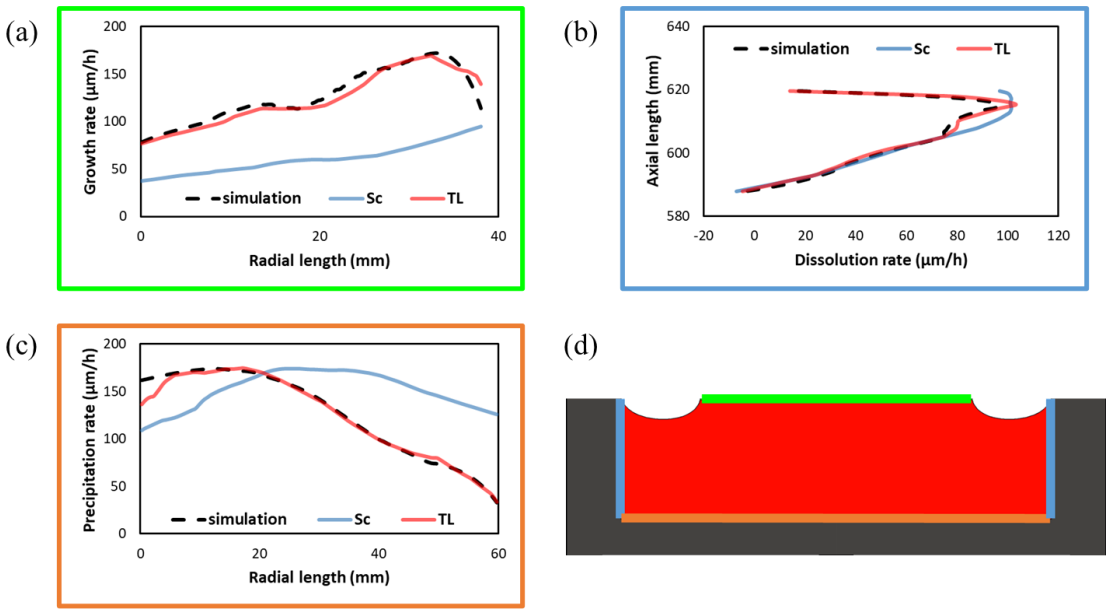

Fig. 2.14. Distribution of (a) growth rate on the crystal surface, (b) dissolution rate on the crucible wall, and (c) precipitation rate of polycrystals on the crucible bottom in the new timestep given by simulation, new model, and transfer model, respectively. (d) schematic diagram of the three boundaries.

To better understand why transfer learning can achieve high accuracy with a small amount of training data, the weight values of fully connected layers in the network are extracted. The difference in weights between the models trained with 100% data and

20% data is plotted in Fig. 2.15, for the cases of transfer learning and training-from-scratch, respectively. Here the difference is defined as $d_{i,j} = abs(\frac{w_{i,j}^{100\%} - w_{i,j}^{20\%}}{w_{i,j}^{100\%}})$, where $w_{i,j}$ denotes the weight of the node (*i*, *j*) in the layer, and the superscript tells whether the model is trained with 100% or 20% data. For transfer learning in Fig. 2.15 (a), the models trained with 20% and 100% have little difference in the first 3 layers, and the difference becomes non-negligible in the last layer. This indicates that the more general features stored in the shallower layers are successfully inherited from the source model without much modification, therefore the small amount of data can be utilized more efficiently to rectify almost only the last layer which stored more specific features of the new timestep and has simpler structure (128×1). On the contrary, the difference is considerable for every layer in the case of training a new model (Fig. 2.15(b)), indicating the incapability of using small data to train the whole model. This result explains the different performance between the transferred model and the new model in Fig. 2.13.

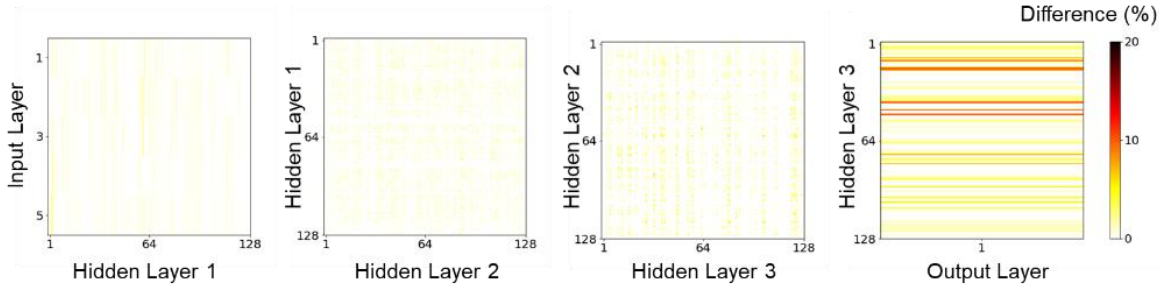

(a)

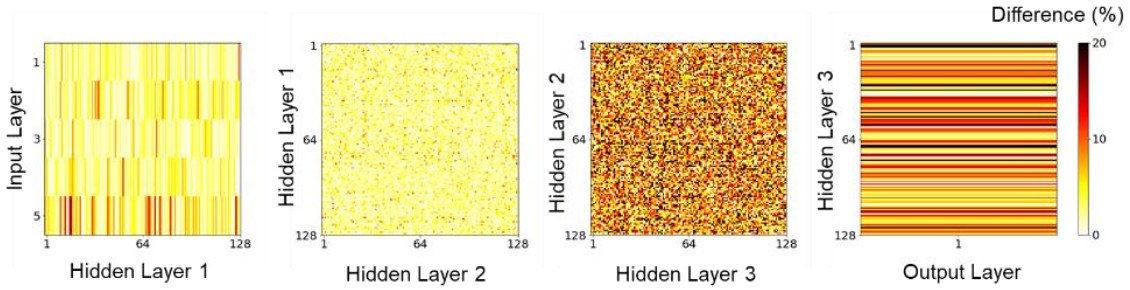

(b)

Fig. 2.15. Difference of weights in 4 fully connected layers between the models trained with 100% and 20% data: (a) transfer modes; (b) new models. The layers have 5 ×128, 128×128, 128×128, and 128×1 weights, respectively.

2.5.3 Stability of transfer learning through multiple timesteps

Sec. 2.5.2 has demonstrated that transfer learning can maintain high accuracy even with a small amount of data when predicting the unsteady changes in a new timestep. For practical application of adaptive process design, it is necessary to test the sustainability of this high accuracy in a multi-timestep sequence. For this purpose, 4 successive timesteps with Δt=1 h are proceeded and transferred models are trained with different data amounts in each timestep. For the transferred model trained with *n%* data in timestep *i*, it acts as the source model for the transfer training with *n%* data in timestep *i+1*. The timestep *i+1* is updated based on the optimal condition in timestep *i* yielded by the optimization algorithm. As shown in Fig. 2.16, the transferred model trained with 20% amount of data can maintain a relatively low MAE value regardless of the time evolution. This result implies that the high data efficiency can be stably transmitted through multiple timesteps, which proves the feasibility of the application of transfer learning in long-term adaptive process design. Interestingly, the values of MAE of the models trained with relatively more data (100% and 60%) can even gradually decrease. It can be explained that transfer learning inherits not only the knowledge learned in the previous time step, but also the inaccuracy, and is capable of further decreasing this inaccuracy when fed with relatively large amount of data. This result expands the application scope of transfer learning: when being applied with small amount of data, it can improve the efficiency and meanwhile keep the accuracy; when being applied with large amount of data (still no more than 100%), it can further improve the accuracy for the long-term prediction.

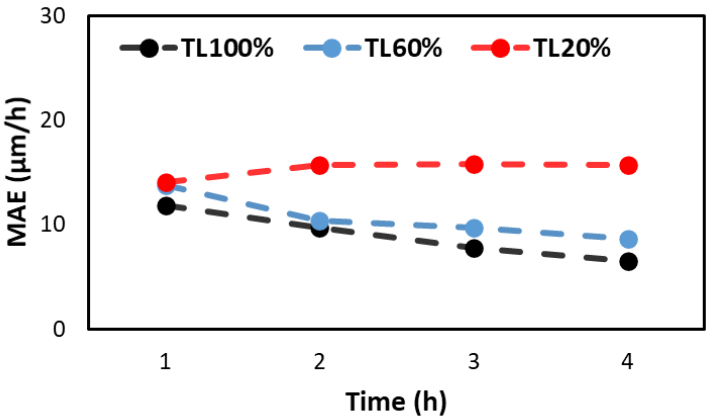

Fig. 2.16. Evolution of the performance of transfer models in multiple timesteps

2.6 Conclusions

In this study, the instability caused by configuration changes during long-term SiC solution growth was investigated. A quasi-unsteady 2D simulation model was constructed to depict the evolution of single SiC crystal growth, carbon crucible dissolution, and SiC polycrystal precipitation during long-term growth under a certain combination of controlling parameters. This model was initially applied to investigate the unsteady feature of an original recipe with fixed parameters. The maximum available growth time of this fixed recipe was limited to ~50 h due to the high polycrystal height, deep crucible dissolution, and non-uniform single crystal surface. Accordingly, a machine learning-based optimization system was proposed to design an optimal recipe with time-dependent parameters in a 100-timestep sequence. Machine learning models were trained by simulation data to instantly provide an accurate prediction of unsteady changes and were combined with an NSGA-II optimization algorithm to determine the optimal control parameters to maintain a high and uniform growth rate, low crucible dissolution rate, and low polycrystal precipitation rate in each timestep. Machine learning allowed for a 300-fold reduction in calculation time. The adaptive recipe yielded by optimization effectively suppressed crucible dissolution and polycrystal precipitation compared to the fixed recipe, thereby extending the available growth time by 50%. In addition, the adaptive recipe facilitated the growth of a 30% thicker single crystal with a flatter surface. These findings demonstrate the importance of dynamic adaptive control for long-term SiC solution growth and provide qualitative guidance for further practical experiments and production. Moreover, to further improve the optimization efficiency, a transfer learning strategy was introduced into the optimization system as a feasibility study. It was found that compared with the original training strategy, which is to train the machine learning model from scratch, the transferred model could achieve the same-level prediction accuracy, but with 80% less training data amount. The stability of this high efficiency was also examined in successive multiple timesteps, which demonstrated the capability of transfer learning in the optimization of the long-term SiC solution growth process.

References

[1] M. Metzger. *J. Cryst. Growth* 2001, 230, 210-216.

[2] M. Margulies, P. Witomski, T. Duffar. *J. Cryst. Growth* 2004, 266, 175-181.

[3] R. Backofen, A. Voigt, D. Wulff-Molder. *J. Cryst. Growth* 2005, 275, e349-e353.

[4] R. Backofen, A. Ribalta, A. Voigt, D.Wulff-Molder. *J. Compt. Appl. Math.* 2007, 203, 362-375.

[5] M.P. Bellmann, O. Patzold, M. Stelter, H.J. Moller. J. Cryst. Growth 2010, 312, 2175-2178.

[6] T. Fuhner, T. Jung. *J. Cryst. Growth* 2004, 266, 229-238.

[7] Y. Dang, L. Liu, Z. Li. *J. Cryst. Growth* 2019, 522, 195-203.

[8] Y. Tsunooka, N. Kokubo, G. Hatasa, S. Harada, M. Tagawa, T. Ujihara. *CrystEngComm* 2018, 20, 6546-6550.

[9] M. Asadian, S. Seyedein, M. Aboutalebi, A. Maroosi. J. Cryst. Growth 2009, 311, 342-348.

[10] N. Dropka, M. Holena, S, Ecklebe, C. Frank-Rotsch, J. Winkler. *J. Cryst. Growth* 2019, 521, 9-14.

[11] N. Dropka, M. Holena. *J. Cryst. Growth* 2017, 471, 53-61.

[12] CGSim, https://www.strsoft.co.jp/product/cgsim.html (2021).

[13] T. Yamamoto, Y. Okano, T. Ujihara, S. Dost. *J. Cryst. Growth* 2017, 470, 75-88.

[14] H. Daikoku, S. Kawanishi, T. Ishikawa, T. Yoshikawa. *J. Chem. Thermodynamics* 2021, 160, 106476.

[15] K. Ando, H. Lin, Y. Tsunooka, T. Narumi, C. Zhu, K. Kutsukake, S. Harada, K. Matsui, I. Takeuchi, Y. Koyama, Y. Kawajiri, M. Tagawa, T. Ujihara. *19th International Conference on Crystal Growth and Epitaxy (ICCGE-19)*, 2019.

[16] N. Komatsu, T. Mitani, Y. Hayashi, T. Kato, S. Harada, T. Ujihara, H. Okumura. *J. Cryst. Growth* 2017, 458, 37-43.

[17] M. Imade, Y. Hirabayashi, Y. Konishi, H. Ukegawa, N, Miyoshi, M. Yoshimura, T. Sasaki, Y. Kitaoka, Y. Mori. *Appl. Phys. Express* 2010, 3, 075501.

[18] Y. Hayashi, T. Mitani, N. Komatsu, T. Kato, H. Okumura. *J. Cryst. Growth* 2019, 523, 125151.

[19] A.S. Myerson. *Handbook of Industrial Crystallization*, Butterworth-Heinemann, 2nd ed., 2002, 141-148.

[20] Optuna, https://optuna.org/.

[21] D.P. Kingma, J.B. Adam. *International Conference on Learning Representations (ICLR)*, 2015.

[22] K. Deb, A. Pratap, S. Agarwal, T. Meyarivan. *IEEE Trans. Evol. Comput.* 2002, 6, 182-197.

[23] F.A. Faber, A. Lindmaa, O.A. von Lilienfeld, R. Armiento. *Phys. Rev. Lett.* 2016, 117, 135502.

[24] J. Schmidt, J. Shi, P. Borlido, L. Chen, S. Botti, M.A. Marques. *Chem. Mater.* 2017, 29, 5090-5103.

[25] J. Lee, A. Seko, K. Shitara, K. Nakayama, I. Tanaka. *Phys. Rev. B.* 2016, 93, 115104.

[26] K. Weiss, T.M. Khoshgoftaar, D. Wang. *J. of Big Data* 2016, 3, 1-40.

[27] C. Tan, F. sun, T. Kong, W. Zhang, C. Yang, C. Liu. *arXiv* 2018, https://arxiv.org/abs/1808.01974.
[28] H. Yamada, C. Liu, S. Wu, Y. Koyama, S. Ju, J. Shimoi, J. Morikawa, R. Yoshida. *ACS Cent. Sci.* 2019, 5, 1717-1730.
[29] J. Yosinski, J. Clune, Y. Bengio, H. Lipson. *Adv. Neural Inf. Process Syst.* 2014, 2, 3320-3328.
[30] R. Jalem, K. Kanamori, I. Takeuchi, M. Nakayama, H. Yamasaki, T. Saito. *Sci. Rep.* 2018, 8, 5845.
[31] D. Jha, K. Choudhary, F. Tavazza, W. Liao, A. Choudhary, C. Campbell, A. Agrawal. *Nat. Commun.* 2019, 10, 5316.
[32] H. Oda, S. Kiyohara, K. Tsuda, T. Mizoguchi. *J. Phys. Soc. Jpn.* 2017, 86, 123601.
[33] X. Li, Y. Zhang, H. Zhao, C. Burkhart, L.C. Brinson, W. Chen. *Sci. Rep.* 2018, 8, 13461.
[34] B. Ma, X. Wei, C. Liu, X. Ban, H. Huang, H. Wang, W. Xue, S. Wu, M. Gao, Q. Shen, M. Mukeshimana, A.O. Abuassba, H. Shen, Y. Su. *npj Comput. Mater.* 2020, 6, 125.
[35] M. Kaya, S. Hajimirza. *Sci. Rep.* 2019, 9, 5034.

3. Compositional instability of solution and improved design

3.1 Introduction

For TSSG of SiC crystal, several elements besides silicon (Si) are added to the solution to increase carbon solubility or improve crystal surface morphology. Among them, aluminum (Al) plays an important role, not only to serve as the dopant for p-type crystals, but also to increase the interfacial energy on the crystal/solution surface and thusly reduce the frequency of two-dimensional nucleation [1, 2]. It was reported that even 1% more Al concentration in solution may significantly improve the crystal surface morphology and polytype stability [3]. However, besides being incorporated into the grown crystal, Al may also be consumed by the evaporation during growth due to its high volatility or the reaction with the graphite crucible wall. It can be imagined that the continuous Al loss may increase the instability of the growth process and negatively affect the crystal quality. Excessive Al addition in the initial solution might be a compensation for this loss, but it will impede the growth of N-type SiC crystal and result in other problems like inhomogeneous doping or degradation of system components made from carbon. Therefore, the evaporation of Al and the subsequent reactions should be investigated and further suppressed to enhance the composition stability of the solution during long-term growth.

Not only in solution growth of SiC, the evaporation loss of the liquid phase is a common problem in crystal growth fields. For the growth of most compound semiconductor crystals, suitable chemical stoichiometry in the melt is one of the crucial factors to achieve a preferable growth condition [4]. In the liquid phase, some solutes are relatively more volatile than others, especially under the extremely high-temperature environment, and the continuous evaporation of a certain solute during the long-term growth may make the solution deviate from its predetermined and well-designed composition. It has been widely reported in literature that the evaporation of volatile solutes may result in problems like defects formation, inhomogeneous doping, and limited growth time [5-11]. Aiming at suppressing the evaporation and maintaining the stable solution composition, several methods have been proposed and proven to be effective, including increasing the vapor pressure of the volatile material in the gas phase via intentionally evaporation [12], sealing the crucible with encapsulant [13], elevating the atmosphere pressure [14, 15], changing the atmosphere composition [15-17], lowering down the growth temperature [18, 19], and continually feeding the volatile

material [19]. However, most of these methods cannot be generally applied due to the particularity of different growth systems, and some may increase the cost of the growth process. Moreover, almost all the previous studies focused on the effectiveness of suppression methods experimentally and qualitatively, while their quantitative effects on evaporation behavior remain unknown, which restricts further optimization.

To better understand the compositional instability of solution during long-term crystal growth of SiC, the present study proposes a numerical model of computational fluid dynamics (CFD) that simulates the detailed transport paths of a certain solute, and can therefore predict the concentration evolution over time. This model is employed to simulate the unsteady Al transport in a 3-inch SiC solution growth system. Accordingly, a facile and economical geometric structure design is proposed aiming at suppressing Al loss, and its effectiveness is examined both numerically and experimentally.

3.2 Description of the numerical model

3.2.1 Experimental setup

The solution growth experiment of a 3-inch SiC crystal is performed in a radiofrequency (RF) heating system with a frequency of 3 kHz (Fig. 3.1 (a)). A graphite crucible surrounded by thermal insulator acts as both container and carbon source of the solution with chemical compositions of $Si_{0.58}Cr_{0.4}Al_{0.02}$. The diameter and height of the solution are 60 mm and 30 mm, respectively. A 1◦ off-axis 4H-SiC seed with Si polarity is mounted on the tip of a graphite shaft and is dipped in the solution with a meniscus height of about 0.5 mm. The temperature near the center of the seed crystal is measured by a thermocouple inserted inside the graphite shaft, and is controlled and kept at 2173 K (1900 ◦C) during the growth process. The furnace is filled with helium gas and the pressure is maintained at 1 atm. The rotation pattern of seed and crucible is the same as the original fixed recipe in Chapter 2.

To suppress the Al evaporation loss, we propose a new structure with a graphite disk placed 60 mm above the solution, which is referred to as the “fin” (Fig. 3.1(b)). The thickness of the fin is 1 cm, while there is a 5 mm gap between the inner and outer fin for security consideration because the shaft and the crucible rotate independently. Two growth experiments, with and without fin structure, are conducted using the same growth condition. The step morphology and step height of grown crystals are observed and measured using 3CCD real color confocal microscope (Lasertec, OPTELICS H1200).

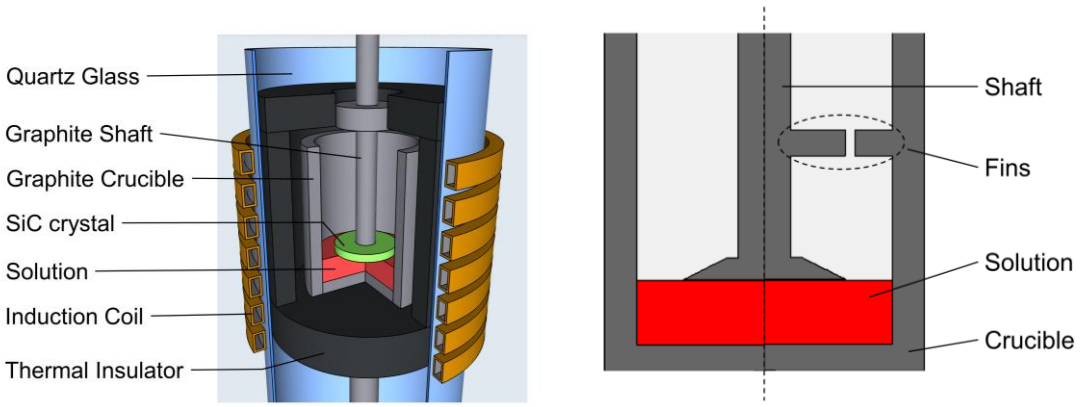

(a) (b)

Fig. 3.1. (a) Configuration of the original solution growth system and (b) schematic view inside the crucible (left: original structure; right: with fin structure).

3.2.2 CFD simulation

The numerical simulation of the mass transport of Al is performed in 2 sequential steps: (i) simulation of the global temperature and velocity field throughout the solution growth system; (ii) calculation of the transient mass concentration of Al under the effects of diffusion and convection in both liquid and gas phases, and constrained by the physical and chemical equilibriums at the reaction boundaries. The models used in the simulation are described below.

Model of fluid flow and heat transfer

The 2D steady global model built in the foregoing chapter is employed to simulate the fluid flow, and heat transfer inside the crystal growth system. Magnetic, flow and thermal fields are coupled and solved numerically by the finite volume method via CGSim commercial software. The structural layout and controlling parameters are the same as those in the experiments introduced previously. In this chapter, we mainly focus on the evolution of Al concentration, and thusly the unsteady changes of the crucible shape are not considered to simplify the problem.

Model of mass transport of Al

Based on the flow and thermal fields obtained above, the governing equation of Al transport in fluids can be expressed as:

$$\frac{\partial(\rho_{l,g}C_{l,g})}{\partial t} + \nabla \cdot (\rho_{l,g}C_{l,g}\vec{u}) = \nabla \cdot (\rho_{l,g}D_{l,g}\nabla C_{l,g}) \qquad \text{(Eq. 3-1)}$$

where ρ denotes the density, C the mole concentration of Al (mol/m^3), $\vec{u}$ the velocity and D the diffusion coefficient (m^2/s). The subscripts l and g represent the liquid and gas phases, respectively. The diffusion coefficient of Al in the solvent (D_l) can be obtained through the Stokes-Einstein equation:

$$D_l = \frac{k_B T}{6\pi\eta r} \quad \text{(Eq. 3-2)}$$

where k_B, T, η and r are Boltzmann's constant, temperature (K), dynamic viscosity (Pa · s), and radius of Al atom.

Similarly, the diffusion coefficient of Al in helium gas can be obtained through the Chapman-Enskog theory [20]:

$$D_g = \frac{1.859\times10^{-7}T^{3/2}\sqrt{\frac{1}{M_{He}}+\frac{1}{M_{Al}}}}{P(\frac{\sigma_{He}+\sigma_{Al}}{2})^2} \quad \text{(Eq. 3-3)}$$

where M denotes the molar mass (g/mol), P the atmosphere pressure (atm), and σ the particle diameter (Å). Values of parameters used in the calculation are listed in Table 3.1 [21].

Table 3.1 Parameters used in the calculation

Parameter	Value	Unit
Dynamic viscosity of solution, η	$1.266\times10^{-3}exp(1982/T)$	Pa s
Molar mass of He, M_{He}	4	g/mol
Molar mass of Al, M_{Al}	27	g/mol
Molecular diameter of He, σ_{He}	2.6	Å
Atomic diameter of Al, σ_{Al}	2.8	Å

The chemical and physical reactions are considered to probably occur on the three categories of surfaces, namely solution-crucible interface, solution free surface, and the gas-solid interface. Details of the boundary conditions are given below:

(i) At the interface between the solution and graphite crucible, the possibility exists that Al in the liquid phase reacts with carbon to form aluminum carbide. The equation of this reaction and the Gibbs free energy change at 1 atm can be expressed as [22]:

$$4Al\ (l) + 3C\ (s) \leftrightarrow Al_4C_3\ (s), \Delta G^0 \approx -2.42\times10^5 + 94.9T\ J/mol \quad \text{(Eq. 3-4)}$$

The equilibrium constant of the reaction can therefore be found from the free energy change in Eq. 3-4 as:

$$K = \frac{1}{a_{Al}{}^4} = e^{-\Delta G^0/RT} \quad \text{(Eq. 3-5)}$$

where a_{Al} is the atom fraction of Al in solution, and R is the ideal gas constant.

According to Eq. 3-4 and Eq. 3-5, the equilibrium mole fraction of Al at 2173 K is about 0.61, much larger than the real mole fraction of Al in our solution, which is 0.02. A similar conclusion was obtained in literature [23], where graphite crucible was capable

to hold Si-Al solution when the mole fraction of Al is below 0.12% at 1500 °C. Note that this critical concentration increases with temperature, as suggested by Eq. 3-4. Therefore, at the interface of solution and crucible, the forward reaction that consumes Al does not happen, and the Al flux on this boundary is accordingly considered as 0.

(ii) Along the solution-gas free surface, Al evaporates into the gas phase in the form of Al vapor. It is assumed that this reaction reaches an equilibrium state instantly and thusly the partial pressure of Al at the gas side of this boundary equals the saturated vapor pressure of Al on the liquid side. Given that Al concentration inside the solution is low enough to follow Henry's law, the evaporation process can be expressed as:

$$P_p = P^{0\prime} \quad \text{(Eq. 3-6 a)}$$

$$P_p = C_g RT \quad \text{(Eq. 3-6 b)}$$

$$P^{0\prime} = \frac{C_l}{C_{total}} P^0 \gamma \quad \text{(Eq. 3-6 c)}$$

and thusly the relationship between C_g and C_l can be expressed as:

$$C_g = C_l \frac{P^0 \gamma}{C_{total} RT} \quad \text{(Eq. 3-6 d)}$$

where P_p denotes the partial pressure of Al in the gas phase, $P^{0\prime}$ the saturated vapor pressure of the Al in solution, C_{total} the total mole concentration of all solution compositions and is assumed as a constant, P^0 the saturated vapor pressure (Pa) of pure Al, and γ the activity coefficient of Al, the value of which can be found as [24]:

$$logP^0 = -\frac{16380}{T} - logT + 14.445 \quad \text{(Eq. 3-7)}$$

$$log\gamma = -\frac{1570}{T} + 0.236 \quad \text{(Eq. 3-8)}$$

To complete Eq. 3-6 d which has 2 unknowns, the conservation equation of mass flux of Al through the boundary is added:

$$D_g \nabla C_g = D_l \nabla C_l \quad \text{(Eq. 3-9)}$$

(iii) At the solid-gas interface away from the solution area, vapor Al may deposit due to the oversaturated state, which is the main consumption of Al in this system. The boundary condition is given as a conditional form that whether the saturated state is achieved:

$$\begin{cases} C_g = \frac{P^{eq}}{RT}, \ C_g > \frac{P^{eq}}{RT} \\ \nabla C_g = 0, \ C_g \leq \frac{P^{eq}}{RT} \end{cases} \quad \text{(Eq. 3-10)}$$

where P^{eq} is the equilibrium pressure of Al vapor, and $\frac{P^{eq}}{RT}$ denotes the equilibrium concentration at the boundary.

There are two possibilities for this deposition: 1. the physical condensation of Al vapor turning into Al liquid on the cold solid surface, and 2. the chemical reaction of Al vapor with carbon on the graphite or carbon insulator surfaces, whose equation can be written as:

$$4Al(g) + 3C(s) \leftrightarrow Al_4C_3(s) \quad \text{(Eq. 3-11)}$$

To determine which reaction is easier to happen, the equilibrium pressures of both reactions are compared in Fig. 3.2. For the physical condensation, the equilibrium pressure of Al vapor is the same as the saturated vapor pressure of pure Al liquid (P^0), while the equilibrium pressure (Pa) of Eq. 3-11 was measured in literature [25]:

$$log_{10}P \approx -18000/T + 11.412 \quad \text{(Eq. 3-12)}$$

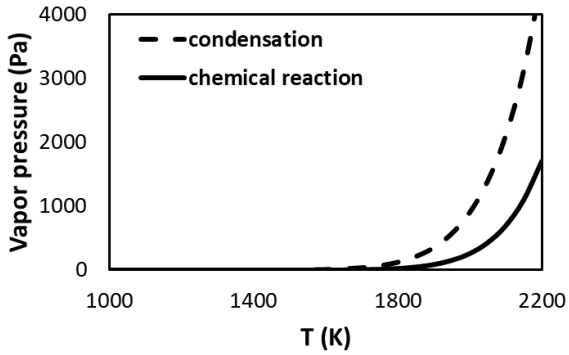

Fig. 3.2. Comparison of equilibrium vapor pressures of Al in the chemical reaction and the physical condensation.

According to Fig. 3.2, the chemical reaction in Eq. 3-11 has lower equilibrium vapor pressure and is therefore predominant compared with the condensation. The deposition material on the graphite surface after the experiment is collected and tested by x-ray Diffraction (XRD). The result shows that Al appeared only as the formation of aluminum carbide instead of elemental Al, which also validates this conclusion. Therefore, on the boundaries of graphite or insulator surfaces, P^{eq} in Eq. 3-10 is set as the equilibrium pressure of the chemical reaction instead of that of condensation.

The initial value of Al concentration in the solution (C_l) is given as 2026.98 mol/m^3 with a uniform distribution, while the initial value of Al concentration in gas (C_g) was 0. The evaporation loss of Si and Cr is not considered here because: 1. the saturated vapor pressures of Si and Cr are much lower compared with Al [24, 26], 2. the activity coefficients of Si and Cr are low in the Si-Cr based solution [27], 3. the reactions and

consumptions of Cr and Si vapors on solid graphite surface are weak, and 4. the crystal growth condition is less sensitive to the slight change of Si or Cr concentration. The incorporation of Al into the grown crystal is also neglected due to the low growth rate (~100 μm/h).

3.3 Results and discussion

3.3.1 Comparison of simulation results between the original and improved designs

When Al evaporates from the solution and reacts with the solid surfaces, the following steps may determine the overall loss rate of Al:

(i) transport of Al atoms in bulk solution to liquid/gas interface;

(ii) Evaporation of Al atoms through the liquid/gas interface into the gas phase;

(iii) Transport of Al atoms in the gas phase to the solid surface.

Among them, step (i) is not considered to be the rate-determining step for the overall Al loss, because the distribution of Al in the liquid phase is relatively uniform due to the strong stirring caused by electromagnetic force. For step (ii), the Al loss rate can be reduced by the strategies like decreasing the free surface area or the growth temperature. However, both two strategies may change the growth environment of SiC crystal and make it away from the initially designed growth condition. Therefore, improving step (iii) is the most effective and promising way to reduce the overall Al loss. In the present study, a "fin" structure is proposed, which is expected to suppress the transport of Al vapor in the gas phase and consequently decrease the amount of Al vapor that reaches the potential reacting solid surfaces. Meanwhile, because this "fin" structure is away from the solution domain, it is believed not to disturb the original thermal environment inside the solution.

To examine the effectiveness of this "fin" structure, steady state simulations of fluid flow and heat transfer are conducted for both the original and the improved cases. As shown in Fig. 3.3(a), the existence of the fin structure above the solution has little effect on the temperature distribution and flow pattern inside the solution domain, because the system is temperature-controlled and the solution is heated directly by the induction heat in the crucible wall and the solution itself. The maximum difference in temperature inside the solution between the two cases is less than 0.5 K, while the maximum difference in temperature on the crystal surface is about 0.2 K. These results indicate that the existence of fin structure has almost no influence on the growth environment of SiC crystal.

For the temperature distribution in the gas phase above the solution (Fig. 3.3(b)), the solid surfaces in the improved case with the fin structure (right) are slightly colder than those in the original case without the fin structure (left), especially for the graphite surfaces at the outlet of insulator where the temperature is about 40 K lower than those in the original case. It can be explained that the fin structure blocks the radiation path from the hot solution area to the cold surfaces away from the solution. An advantage brought by this effect is that the heating power consumed in the improved case (5.2 kW) is ~20% lower than that in the original case without the fin structure (6.7 kW). On the other hand, according to Eq. 3-12, lower temperature may decrease the equilibrium vapor pressure and reaction criterion, and consequently increase the Al consumption. In this aspect, it seems that the fin structure has a negative effect on preserving the Al and enhancing the composition stability of the solution.

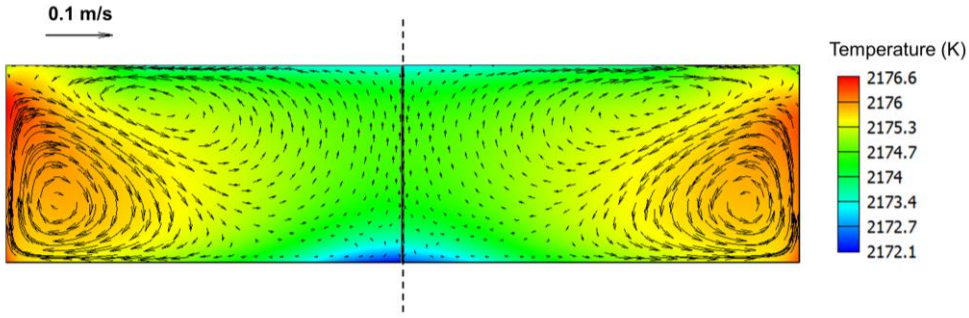

(a)

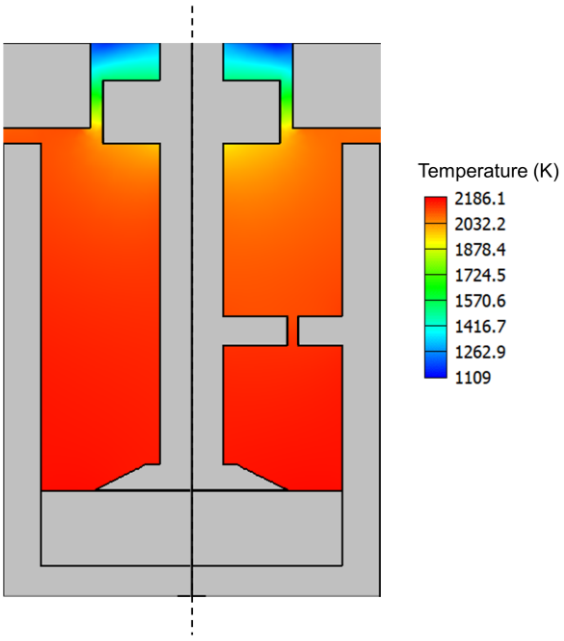

(b)

Fig. 3.3. Temperature distribution in (a) solution area and (b) gas area above the solution (left: without fin structure; right: with fin structure).

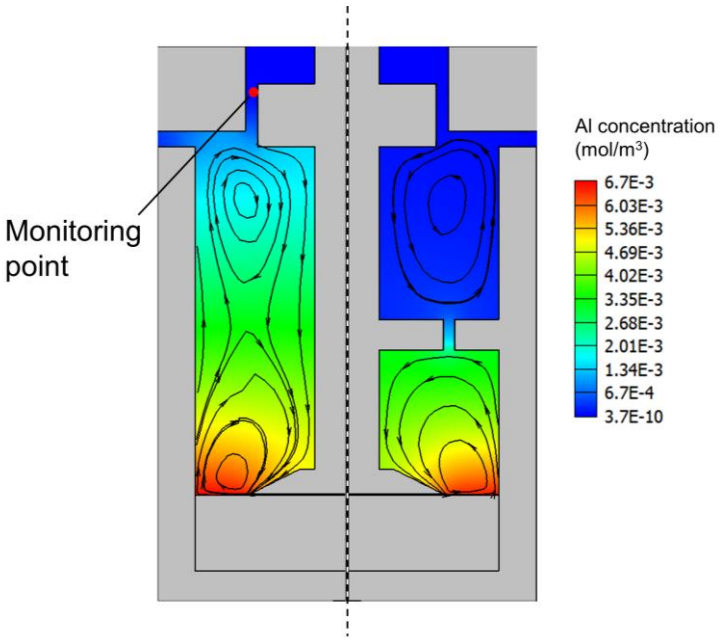

Fig. 3.4. Al vapor distribution in the gas area above the solution after 1 h growth (left: without fin structure; right: with fin structure).

However, for the distribution of Al concentration in the gas phase after 1 h growth (Fig. 3.4), the fin structure shows its superiority that most Al vapor is restricted inside the hot and narrow space between the solution surface and fins, while in the original case Al vapor with relatively high concentration can freely reach the cold graphite surfaces above. This can be explained that in the original case, a large vortex (with a velocity magnitude of 1×10^{-3} m/s) driven by the thermal buoyancy directly and continuously transports the Al vapor from the hot solution surface to the cold graphite surfaces. In the improved case, the fin structure breaks the large vortex into two independent vortexes with similar velocity magnitude, and this significantly reduces the transport of Al from the hot solution to the cold area above. To quantitatively describe the effect of the fin structure, temperature, equilibrium Al concentration, and Al concentration at one monitoring point (shown in Fig. 3.4) near the graphite surface after 1 h unsteady simulation are recorded and shown in Table 3.2. For the improved case with fin structure, although the equilibrium value is about 1.5 times lower than that in the original case due to lower temperature, the concentration of Al vapor is about 10 times lower. For the original case, the concentration of Al vapor at the monitoring point is higher than the equilibrium value at the corresponding temperature, and therefore the consumption of Al consistently occurred, which corresponded with the experiment

result that a large amount of Al_4C_3 deposits were observed at the same area. However, in the improved case with the fin structure, the reaction criterion is not reached at the monitoring point due to the low value of actual concentration, and deposits were seldom observed in practical experiments.

Table 3.2 Temperature, equilibrium concentration and concentration of Al at the monitoring point.

	Temperature (K)	C_{Al}^{eq} (mol/m^3)	C_{Al} (mol/m^3)
Without fin	1587.8	9.0×10^{-5}	1.2×10^{-4}
With fin	1564.8	6.2×10^{-5}	1.2×10^{-5}

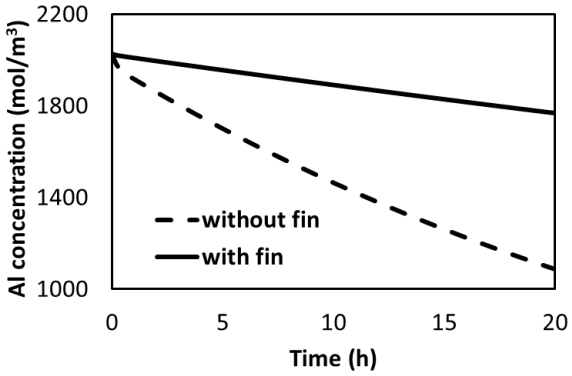

Fig. 3.5. Evolution of Al concentration at monitoring point in solution during 20 h growth.

Long-term unsteady simulations for the Al mass transport process are conducted and the evolutions of Al concentration at another monitoring point inside the solution (10 mm underneath the free surface) in 20 h are recorded as shown in Fig. 3.5. The evolutions of Al concentration in both cases exhibit an exponential decay pattern, but with different decay constants, which indicates the difference in Al consumption ability. After 20 h growth time, the Al concentration at the monitoring point in the improved case with the fin structure is about 1.7 times higher than that in the original case without the fin structure, while more than 70% Al loss is suppressed, which proves the effectiveness of the fin structure to preserve the composition in solution for long-term growth. If neglecting the loss of Si and Cr, after 20 h growth the Al mole fraction in solution in the improved case is about 1.7%, while it is about 1.0% in the original case. According to the previous study [2, 3], even 0.5% lower Al mole fraction in solution may influence the step morphology and poly-types stability on the crystal surface. Therefore, the addition of the fin structure is expected to improve the SiC crystal quality after a

long-time growth. It is worth mentioning that the fin structure has little effect on Al concentration uniformity along the crystal/liquid interface, which is uniform (relative difference between the center and edge is less than 0.1% regardless of the existence of the fin) due to strong stirring.

3.3.2 Comparison of experimental results between the original and improved design

Crystal growth experiments are conducted to validify the effect of the fin structure on the grown crystal. The growth time is 20 h, while the growth conditions in the two experiments are the same except for the existence of the fin structure. For the original case without the fin structure (Fig. 3.6(a)), several particles can be observed on the crystal surface. These particles are considered to adhere to the grown crystal surface after 3D spontaneous nucleation in the solvent due to high supersaturation [27]. The existence of these particles will result in quality problems like trench defects, poly-types and inclusions, and significantly interrupt the growth pattern of step-flow. However, for the improved case with the fin structure (Fig. 3.6(b)), the crystal surface is clear without the spontaneous nucleation particles, which indicates that step flow growth is dominant on the whole surface. It is worth mentioning that the gray circle area at the center of Fig. 3.6(b) is not a defect but the residual solution attached at the end of crystal growth when pulling the crystal up from the solution. Previous studies have proven that the addition of Al in the solution can increase the liquid/solid interfacial energy ($\sigma_{Solid-Liquid}$), and thusly suppress the frequency of spontaneous nucleation [1, 3]. Therefore, the difference in surface morphology shown in Fig. 3.6 is attributed to the difference in Al concentration in the solution after long-term growth.

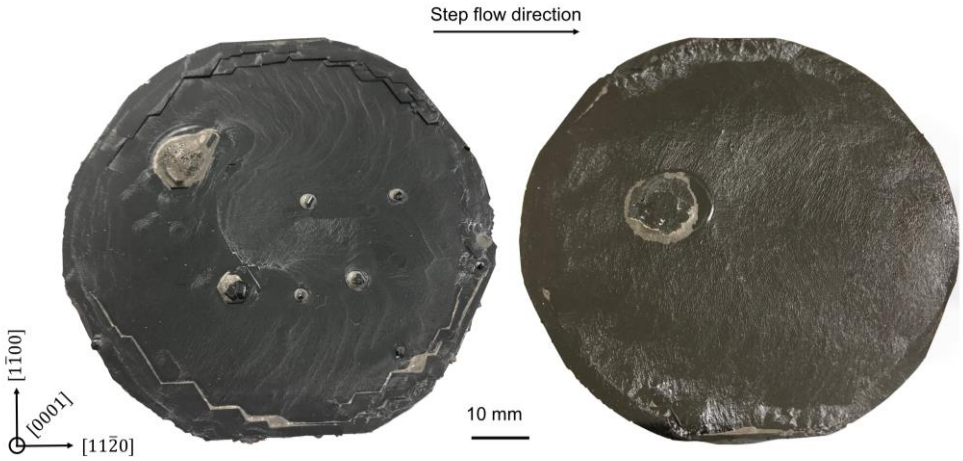

Fig. 3.6. Image of surface morphology of the grown crystals (left: without fin; right: with fin).

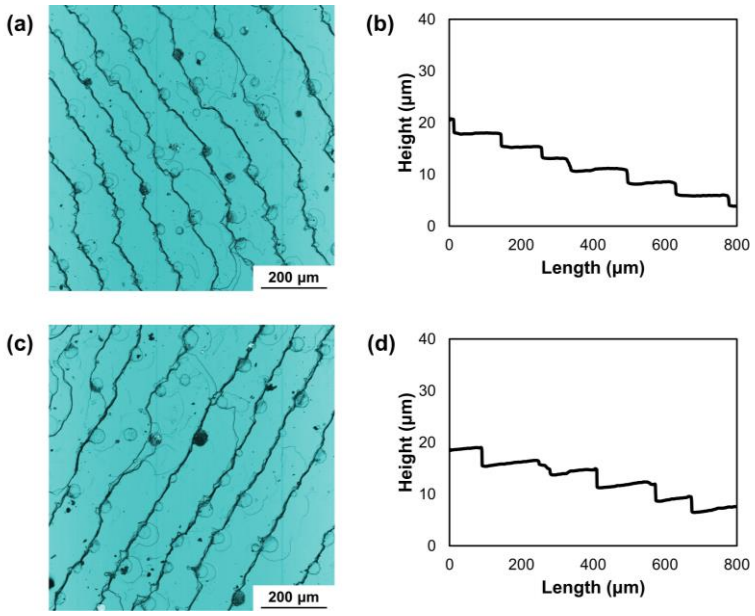

Fig. 3.7. Step morphology (left) and step height profiles (right) of the grown crystal in the original case without fin ((a), (b): upstream; (c), (d): downstream).

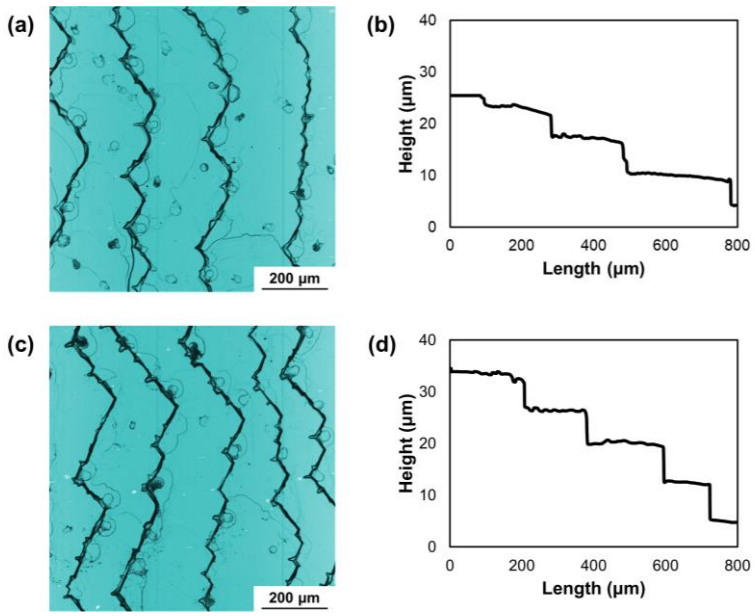

Fig. 3.8. Step morphology (left) and step height profile (right) of the grown crystal in the improved case with fin ((a), (b): upstream; (c), (d): downstream).

According to the previous study [28], the addition of Al in the solution can also enlarge the step height on the (0001) plane of SiC, and consequently enhance the TSD and TED conversion. In the original case without the fin structure (Fig. 3.7), the steps are relatively low with the average step height of around 2.4 μm in the upstream area and 2.2 μm in the downstream area. For the improved case with the fin structure (Fig. 3.8),

the crystal exhibits higher steps, with the average step height of around 5.3 μm in the upstream area and 7.3 μm in the downstream area, which are more than 2 times those in the original case. Since no significant change in growth rate is observed, the variation of Al concentration is believed as the only factor that causes this large difference in step height between the two crystals, which further proves the effectiveness of the fin structure to preserve Al in the solution.

According to the experiment results, the effect of the fin structure on preserving Al in solution and enhancing the composition stability can be validated, which is in accord with the simulation results shown in Section 3.3.1. By suppressing the Al loss, the crystal shows better surface morphology without spontaneous nucleation particles and higher steps which indicates higher crystal quality and higher defects conversion rate.

3.4 Conclusion

To investigate the long-term composition stability in solution growth of SiC, a numerical model is built to simulate the evaporation, transportation, and reaction of Al during the crystal growth process. By comparing the thermodynamic conditions, the chemical reaction of Al vapor on graphite surfaces is considered to be prior to the condensation of Al vapor, as the main consumption of the Al. To better preserve the Al in solution during long-term growth and enhance the composition stability, a so-called “fin” structure is proposed to suppress the evaporation. The simulation result shows that the existence of the fin structure has a slight effect on the thermal and flow condition for SiC crystal growth in the solution, but could significantly suppress the transport and consumption of Al vapor in the gas phase. By applying the fin structure, after 20 h growth, the Al concentration left in the solution is about 1.7 times higher than that in the original case without the fin structure. A bonus of this improved structure is that it can reduce the power consumption of the system by 20% due to the suppression of radiation heat dissipation.

The effect of the fin structure is subsequently validated in SiC solution growth experiments. Compared with the original case, the improved case with the fin structure can effectively eliminate the spontaneous nucleation particles and yield higher steps on the crystal surface, which is preferable for defects conversion and matched well with high-Al-addition features. The experimental results are in good accord with the simulation results and further prove the effectiveness of the fin structure.

The fin structure proposed in the present study provides a concept to suppress the evaporation from the solution and keep the composition stable, but is merely one of the potential strategies. A better approach and further optimization can be conducted in the future based on the numerical approach presented in this study.

References

[1] K. Suzuki, T. Taishi. *Jpn. J. Appl. Phys.* 2020, 59, 025504.

[2] H. Daikoku, S. Kawanishi, T. Yoshikawa. *Cryst. Growth Des.* 2018, 18, 3820-3826.

[3] N. Komatsu, T. Mitani, Y. Hayashi, T. Kato, S. Harada, T. Ujihara, H. Okumura. *J. Cryst. Growth* 2017, 458, 37-43.

[4] M. Razeghi. *Compound semiconductors and crystal growth techniques. Fundamental of Solid State Engineering, 2nd ed.* Springer, New York. 490.

[5] Z. Ye, M. Dong, Y. Yamashita. *J. Cryst. Growth* 2000, 211, 247-251.

[6] Y. Tomm, J.M. Ko, A. Yoshikawa, T. Fukuda. *Sol. Energy Mater. Sol. Cells* 2001, 66, 369-374.

[7] C. Chiang, J. Chen. *J. Cryst. Growth* 2006, 294, 323-329.

[8] G. Behr, W. Loser, D. Souptel, G. Fuchs, I. Mazilu, C. Cao, A. Kohler, L. Schultz, B. Buchner. *J. Cryst. Growth* 2008, 310, 2268-2276.

[9] Y. Bai, S. Xiao, C. Hu, T. Zhang, X. Meng, Q. Li, L. Yang, K. Wong, H. Chen, S. Yang. *Nano Energy* 2017, 34, 58-68.

[10] J.S. Haggerty, K.C. Wills, J.E. Sheehan. *Ceram. Eng. Sci. Proc.* 1991, 12, 1785-1801.

[11] H. Bei, E.P. George, G.M. Pharr. *Intermetallics* 2003, 11, 283-289.

[12] H. Xiao, T. Liang, M. Xu. *Small* 2019, 15, 1901767.

[13] X. Xu, X. Liang, M. Li, S. Solanki, T. Chong. *J. Cryst. Growth* 2008, 310, 1976-1980.

[14] C. Cao, W. Loser, G. Behr, R. Klingeler, N. Leps, H. Vinzelberg, B. Buchner. *J. Cryst. Growth* 2011, 318, 1009-1012.

[15] Z. Galazka, R. Uecker, K. Irmscher, M. Albrecht, D. Klimm, M. Pietsch, M. Brutzam, R. Bertram, S. Ganschow, R. Fornari. *Cryst. Res. Technol.* 2010, 45, 1229-1236.

[16] T. Kotani, J. Chen, H.L. Tuller. *J. Electroceram.* 1998, 2, 7-20.

[17] Y. Tomm, P. Reiche, D. Klimm, T. Fukuda. *J. Cryst. Growth* 2000, 220, 510-514.

[18] H. Di, W. Jiang, H. Sun, C. Zhao, F. Liao, Y. Zhao. *Thin Solid Films* 2021, 720, 138519.

[19] T. Karaki, M. Nakamoto, M. Adachi. *Jpn. J. Appl. Phys.* 2002, 41, 6997-6999.

[20] E.L. Cussler. *Diffusion: Mass Transfer in Fluid Systems, 2nd ed.*, Cambridge University Press, New York, 1997.

[21] H. Daikoku, S. Kawanishi, T. Ishikawa, T. Yoshikawa. *J. Chem. Thermodyn.* 2021, 160, 106476.

[22] G. Deffrennes, B. Gardiola, M. Allam, D. Chaussende, A. Pisch, J. Andrieux, R. Schmid-Fetzer, O. Dezellus. *Calphad* 2019, 66, 101648.

[23] A. Hoseinpur, J. Safarian. *Vacuum* 2020, 171, 108993.

[24] X. Peng, W. Dong, Y. Tan, D. Jiang. *Vacuum* 2011, 86, 471-475.

[25] G.H. Rinehart, R.G. Behrens. *J. Chem. Thermodyn.* 1980, 12, 205-215.

[26] D.R. Stull. *Ind. Eng. Chem.* 1947, 39, 517-540.

[27] Y. Hayashi, T. Mitani, N. Komatsu, T. Kato, H. Okumura. *J. Cryst. Growth* 2019, 523, 125151.

[28] S. Harada, Y. Yamamoto, S. Xiao, M. Tagawa, T. Ujihara. *Mater. Sci. Forum* 2014, 778-780, 67-70.

4. Morphology instability of macrosteps and improved control pattern

4.1 Introduction

As introduced in Chapter 1, the industrial mass production of large-size SiC crystals via the TSSG method is hindered mainly due to the high instability of steps on the growth front. During solution growth, the elemental steps on seed crystal normally bunch and form macrosteps with hundreds of nanometers or even several micrometers in height, due to 1. weak transport of solute in the solution and 2. inhomogeneous supersaturation distribution. The latter effect is especially significant when the size of the crystal increases. Although high and steep macrosteps are required to facilitate the threading dislocations (TDs) conversion and therefore eliminate the native microscopic defects from the seed crystal [1, 2], the over-developed macrosteps may introduce macroscopic defects like the inclusion of solvent and two-dimensional (2D) nucleation of polycrystals [3]. Therefore, an ideal condition, where the macrosteps are neither too low to fail the TDs conversion nor too high to induce inclusion and 2D nucleation, is required for solution growth of SiC. In other words, the process of step bunching is expected to be controllable. Aiming at this target, some researchers added additives into the solution which can alter the property of the crystal-liquid interface and therefore suppress step bunching. Among the various candidates, Al is the most famous which was proven to reduce macrostep height, maintain smooth step morphology and eliminate 2D nucleation. However, the added additives may be incorporated into the grown crystal, affecting the doping and purity level, or resulting in impurity-induced step bunching [4]. The other way of attempting tried to control the flow field inside the solution. It was demonstrated both experimentally and theoretically that the solution flow parallel to the step advancing direction enhances step bunching, while the anti-parallel one relieves step bunching [3, 5]. Based on this concept, Daikoku et al. achieved long-term stable growth using a concave on-axis seed crystal along with a solution flow pattern flowing from the center to the periphery of the crystal [6]. Nevertheless, the off-axis crystal is more favored because of its better performance in TDs conversion and higher utilization ratio in the later process [7], but is more difficult to be compatible with the flow pattern due to the nonaxisymmetric distribution of steps. Using a similar flow pattern to that in Daikoku's study, Liu et al. conducted growth on an off-axis seed crystal and obtained

inhomogeneous distribution of step morphology: low and smooth steps in the upstream area, accompanied by high and rough steps in the downstream area [8]. Therefore, a better flow pattern in the solution should be designed to achieve homogeneous macrosteps distribution with moderate height. The prerequisite of this is a more comprehensive understanding of the relationship between the macrosteps development on the whole crystal surface and the growth condition.

Due to the high cost and extreme environment of the real experiment, simulation has been employed as a powerful alternative to understand the solution growth process of SiC. According to their focuses, previous numerical investigations can be divided into two groups: thermal, flow and mass fields in the solution domain on the macroscale, and step kinetics on the crystal surface on micro- or mesoscale. The former provides exhaustive information in the environmental phase, but is too large-scale to reveal the step-related phenomena on the growth front. The latter one, in contrast, depicts the movement of elemental steps within a local area, but is too small-scale to connect with the real growth condition for a large-size crystal. Although both of them significantly enriched our understanding, a more direct simulation method that can predict the global step morphology on the crystal surface with a given experimental condition remains unexplored. This chapter marks a tentative step toward this simulation method, by combining the numerical models on different scales together. This simulation method can be applied to design and optimize a sophisticated control recipe, which corresponds to ideal step morphology after long-term growth. The effectiveness of this simulation method is examined by experimental results in various cases.

4.2 Method Description

The simulation method compromises three parts, namely: 1. a global 2D computational fluid dynamic (CFD) model to simulate the temperature, flow, and mass concentration fields in the entire growth system, 2. a local 3D CFD model to reveal the carbon transport in the thin layer near the crystal surface, and 3. a kinetic model to describe the movement of macrosteps coupled with the local carbon transport. Each part will be introduced in detail as follows.

4.2.1 Global 2D CFD simulation

A 2D global steady model is firstly built to calculate the distribution of flow velocity ($\vec{V}$), temperature (T), and carbon concentration (C) inside the furnace responding to the variation of controlling parameters. Magnetic, flow, thermal, and concentration fields in macroscope are coupled and calculated numerically by the finite volume method via CGSim commercial software.

The numerical model is constructed based on another growth system different from that used in the previous two chapters. Radiofrequency (RF) heating coils with a frequency of 30k Hz are used to heat up and stir the solution. The temperature at the back of the seed crystal is measured by a thermocouple and the heating power is accordingly adjusted to achieve the desired temperature. The furnace is filled with argon gas at a fixed pressure of 1 atm. The solution domain is 80 mm in diameter and 27 mm in height, with chemical compositions of $Si_{0.95}Ti_{0.05}$. The seed crystal, which is 40 mm in diameter (1.6-inch), is mounted on the upper graphite shaft. The crystal and crucible are able to move rotationally and vertically in an independent manner. There are mainly 4 operation parameters to control the growth condition, namely: growth temperature (at the monitoring point), crucible position, and rotation speeds for both crystal and crucible. Note that the crucible configuration and solution composition changes discussed in previous chapters are not considered here, due to: 1. shorter growth time and lower growth rate, and 2. lower volatility of Ti compared with Al.

In the CFD simulation, the material properties of pure silicon are employed instead of the $Si_{0.95}Ti_{0.05}$ solution, due to a lack of knowledge of the property of the latter one. It is believed that 5% titanium did not significantly change the property in bulk solution. Therefore, the equilibrium carbon concentration (mol/m^3) in pure silicon is set as the Dirichlet boundary condition for both the crystal-solution and crucible-solution interface, which can be expressed as [9]:

$$C_{eq} = \frac{\rho_{Si}}{M_{Si}} \frac{x_{C_{eq}}}{1-x_{C_{eq}}} \quad \text{(Eq. 4-1)}$$

$$x_{C_{eq}} = exp(6.249 - 24460/T) \quad \text{(Eq. 4-2)}$$

where ρ_{Si} denotes the density of liquid pure silicon, M_{Si} the molar weight of silicon, and $x_{C_{eq}}$ the saturated carbon molar fraction in the solution, T the temperature.

4.2.2 Local 3D CFD simulation

When investigating the step behavior on the crystal surface, the foregoing 2D global model becomes incapable due to 1. the step development on an off-axis crystal surface is not axisymmetric and shows strong three-dimensional feature; and 2. the meshes in the global model are coarse to precisely describe the solute transport near the crystal surface since the solute is preferentially absorbed by the steps rather than the terrace. Therefore, a local 3D CFD model is constructed as a transition between the 2D global simulation and the step kinetics, by simulating the carbon transport inside the boundary layer. The mesh number is approximately one million with 25 grids in Z direction (Fig. 4.1 (a)). Within the boundary layer, the flow velocity normal to the crystal surface can be neglected, and diffusion becomes the dominant form of carbon transport.

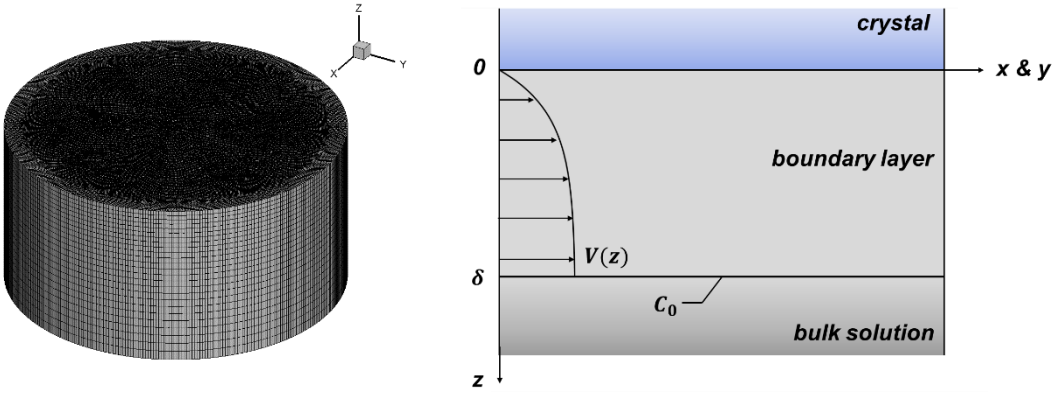

(a) (b)

Fig. 4.1. (a) Geometry and mesh of local simulation. Note that z and x&y directions are plotted in different scales; (2) Schematic of local simulation

For the 3D local model, the diameter of the calculation domain is in accordance with the crystal diameter, while the height is the thickness of the diffusion boundary layer. According to the Burton-Prim-Slichter equation [10], the boundary layer thickness δ is independent of radial position and can be determined by:

$$\delta = 1.6D^{1/3}\nu^{1/6}\omega^{-1/2} \quad \text{(Eq. 4-3)}$$

where D is the diffusion coefficient, ν the kinematic viscosity, and ω the angular velocity of crystal rotation. Unlike the global 2D CFD model, only the unsteady diffusion equation (Eq. 4-4) is solved inside the boundary layer to save calculation resource.

$$\frac{\partial C}{\partial t} + \vec{V} \cdot \nabla C = D\nabla^2 C \quad \text{(Eq. 4-4)}$$

With the flow velocity in the normal direction being 0, the flow velocity parallel to the crystal surface is given by [5]:

$$\vec{V}(z) = \vec{V}_0[1 - \exp(-\frac{4.6z}{\delta})] \quad \text{(Eq. 4-5)}$$

where z denotes the verticle distance from the crystal surface, and $\vec{V}_0$ is the flow velocity in bulk solution, the distribution of which can be obtained from the global CFD simulation. When z equals δ, $V(z)$ equals $0.99V_0$, which matches with the definition of the boundary layer. The schematic is shown in Fig. 4.1(b).

For the boundary away from the crystal surface (lower boundary in Fig. 4.1(b)), the distribution of carbon concentration (C_0) is extracted from the global CFD model at the corresponding position, and is set as the Dirichlet boundary condition. For the crystal surface (upper boundary in Fig. 4.1(b)), the carbon concentration is given in the form of

the Robin boundary condition, which is coupled with the step kinetics and will be introduced in the following section.

4.2.3 Surface kinetics model

Given that the height of an elemental 4H-SiC step (*h*) is 0.3 nm, the width of the terrace between two neighbor steps for a 1°off vicinal surface is approximately 17 nm. Therefore, more than 2 million elemental steps exist on the initial vicinal face for a 1.6-inch seed crystal. The required computation resource is unaffordable when one tries to trace the behavior of each step responding to the carbon transport in the boundary layer. Since the focus of this study is the distribution of macrostep morphology on the whole crystal surface, it is assumed that in the observation scale (~1 mm), N neighbor elemental steps move in the same manner and can be considered as an aggregation (macrostep). Therefore, the problem could be simplified and in the present study 100 equidistant macrosteps are aligned as the initial condition ($N \approx 20{,}000$). The distance Δx between two neighbor steps is 0.4 mm. Each step is discretized into equidistant nodes with the interval Δy =0.4 mm, and each node represents a step section (Fig. 4.2).

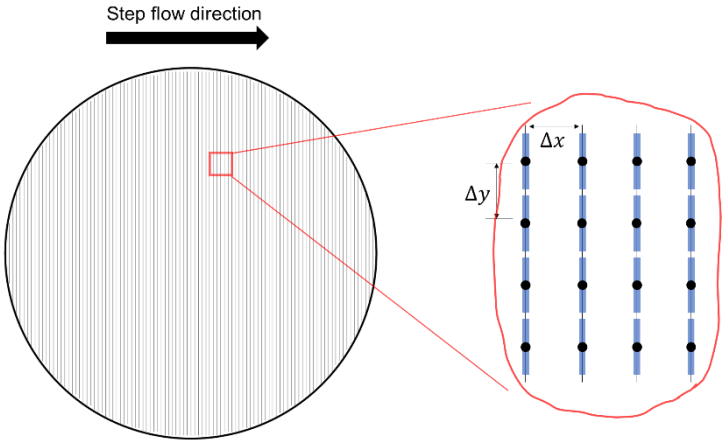

Fig. 4.2. Schematic of the surface kinetics model

A step flow growth mode is assumed in this calculation, indicating the solute would be incorporated into the crystal only through the step other than the terrace. The step distribution on the crystal surface therefore determines the boundary condition of the local CFD model [5]:

$$\begin{cases} On\ step\colon D\dfrac{\partial C}{\partial z} = NK_{st}\left(C - C_{eq}\right) \\ On\ terrace\colon D\dfrac{\partial C}{\partial z} = 0 \end{cases} \qquad \text{(Eq. 4-6)}$$

where K_{st} is the step kinetic coefficient, which is the crucial parameter in this calculation. Since K_{st} can hardly be measured directly, the value used in this study is roughly

estimated according to the vertical growth rate, off-axis angle, and simulated supersaturation [11]. Eq. 4-6 can be interpreted as that the amount of solute absorbed by the steps is proportional to the local supersaturation, while no solute is consumed by the terrace.

Once the carbon distribution is determined, a step's velocity (V_{st}) can be calculated from the local carbon concentration, with υ_c being the molar volume of the crystal [12]:

$$V_{st} = K_{st}\upsilon_c(C - C_{eq}) \quad \text{(Eq. 4-7)}$$

The direction of the step velocity is assumed to be perpendicular to the step segments. The value of C_{eq} is not only temperature-dependent, but also determined by both the effects of local curvature and the distance from neighbor steps. The former can be found in the famous equation of Thomson-Gibbs, describing a natural straightening effect of a curved step due to surface tension [12]:

$$C_{eq}(r) = C_{eq}^0 \exp(\frac{\varkappa N h^2}{rkT}) \quad \text{(Eq. 4-8)}$$

where r is the local radius of curvature of a step, C_{eq}^0 the original equilibrium concentration (shown in Eq. 4-1), $\varkappa$ the specific edge energy of the step, and k the Boltzmann constant. Likewise, if two steps are close enough, the repulsive force will prevent the rear step from passing over (overhang). This effect can be expressed as [13, 14]:

$$C_{eq}(d) \approx C_{eq}^0(1 - \frac{\partial U(d)}{\partial d}\frac{Nh^2}{kT}) \quad \text{(Eq. 4-9 a)}$$

$$U(d) = \frac{2(1-\sigma^2)}{\pi E} N(\beta h)^2 \frac{1}{d^2} \quad \text{(Eq. 4-9 b)}$$

where d is the distance between two neighbor steps, U the potential energy on the vicinal face, σ the Poisson's ratio, E Young's modulus, and β the step stiffness. Here the value of β is assumed to be the same as step energy.

In the practical off-axis crystal growth, new steps are controlled to originate from TSDs at the very upstream area, and the generation rate is positively associated with the local supersaturation. To reproduce this phenomenon in the simulation, the position of the upmost step is monitored. If it moves too far and leaves the terrace behind it (the distance to the upstream edge) wider than a critical value, the increasing local supersaturation will trigger the origination of a new straight step at the initial position. Likewise, if a step segment passes over the downstream edge, it will be treated as "vanished" from the calculation. At the end of every timestep, the operations of displacement ($\Delta l = V_{st}\Delta t$), origination, and vanishment together determine the updated step distribution, which reversely alter the carbon concentration field inside the

boundary layer in the new timestep. The detailed values of the parameters used in the calculation are listed in Table 4.1.

Table 4.1 Parameters used in the simulation

Parameter	Symbol	Value	Unit
Solution density	ρ_{Si}	2.55×10^{3}	$\mathrm{kg/m^3}$
Molecular weight	M_{Si}	2.8×10^{-2}	kg/mol
Diffusion coefficient	D	1.7×10^{-8} [15]	$\mathrm{m^2/s}$
Step height	h	3×10^{-10}	m
Step kinetics coefficient	K_{St}	0.384	m/s
Volume of 4H-SiC primitive cell	v_c	2.06×10^{-29}	$\mathrm{m^3}$
Specific edge energy	$\varkappa$	1.7×10^{-9} [16]	J/m
Poisson's ratio	σ	0.142 [17]	No unit
Young's modulus	E	430 [17]	GPa
Step stiffness	β	5.8 [16]	N/m

4.3 Results and discussion

4.3.1 Effect of crystal rotation speed

The simulation model is first applied to investigate the effect of crystal rotation, the most conveniently and frequently adjusted controlling parameter, on macrostep morphology. Two cases with the same growth condition except for different rotation speeds of crystal, which are 50 and 100 rpm respectively, are studied. The growth temperature is 2173 K, while there is no rotation for the crucible. Fig. 4.3 shows the temperature and flow fields inside the solution domain under both cases, calculated by the global CFD simulation described in Sec. 4.2.1. It can be observed that higher crystal rotation speed enhances the convection inside the solution, which results in more uniform temperature distribution. Especially near the center of the seed crystal, the stronger upward flow owing to higher crystal rotation speed is expected to facilitate the carbon transport to the center area. Temperature, carbon concentration, and velocity at the boundary layer surface are then extracted from the global CFD simulation, as the boundary condition for the local CFD simulation. For the case with 50 rpm crystal rotation, the boundary layer thickness is 0.565 mm, while it is 0.400 mm for the case with 100 rpm crystal rotation. The distribution of velocity and supersaturated carbon concentration ($\Delta C = C - C_{eq}$) at the boundary layer surface is shown in Fig. 4.4. By including the azimuthal velocity, the planar flow field near the crystal surface shows a rotational pattern, indicating the dominance of azimuthal velocity, whose effect is often neglected in 2D simulation. Besides the stronger solution flow, faster crystal rotation also

results in higher supersaturation with more uniform distribution, which is preferable for a higher growth rate and flatter interface.

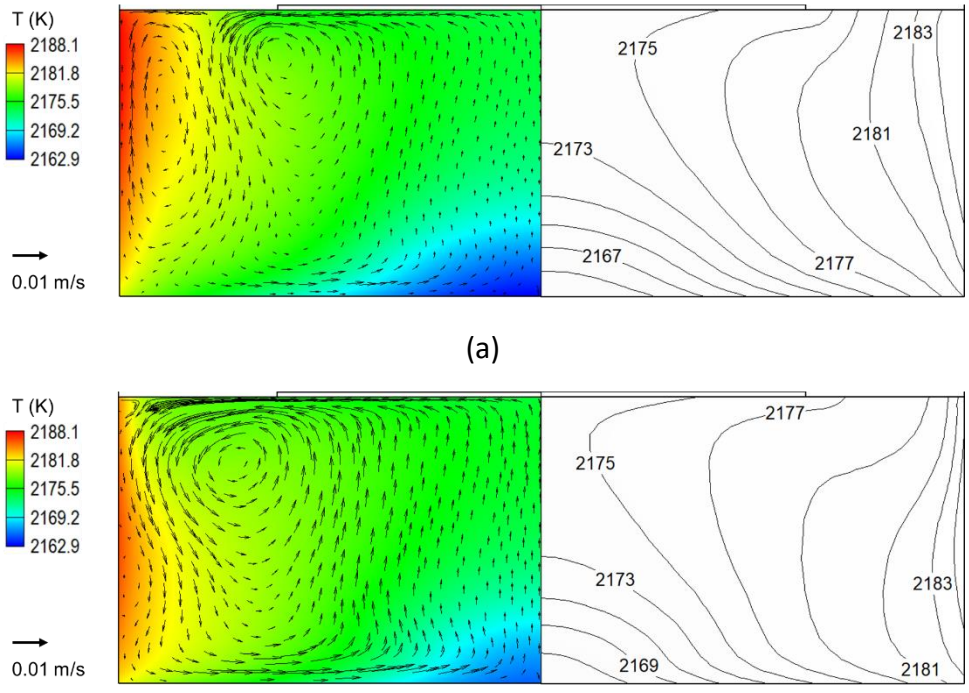

Fig. 4.3. Temperature and flow fields in the solution domain with different crystal rotation speed: (a) 50 rpm and (b) 100 rpm.

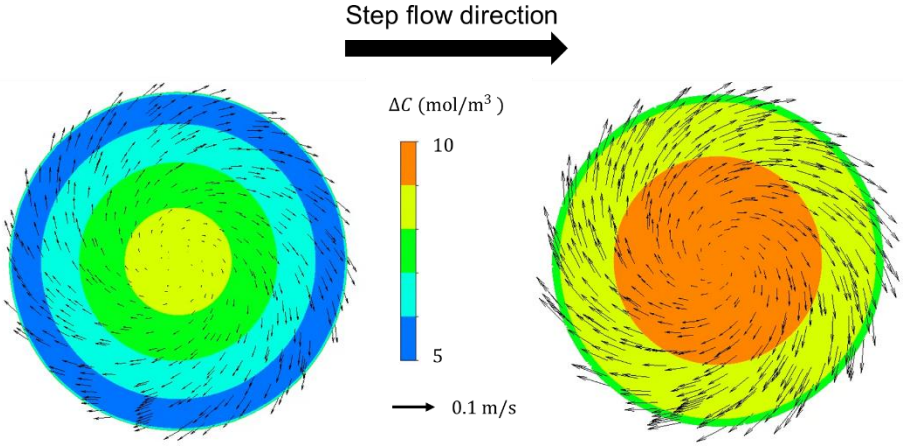

Fig. 4.4. Supersaturated carbon concentration and velocity distribution at the boundary layer surface with different crystal rotation speed: 50 rpm (left) and 100 rpm (right).

The local CFD simulation is then coupled with the surface kinetics model to describe the macrosteps movement under the respective circumstances. The evolutions of

macrostep morphologies during 80 timesteps (Δt =1000 s) are presented and compared in Fig. 4.5. It can be observed that in both cases, step bunching occurs and accumulates at the upper right area on the crystal surface, where the local solution flow direction is parallel to the step advancing direction. This parallel flow hindered the supplement of the carbon atom to the step, and the local carbon depletion induced step bunching. The bunched macrosteps move slower than the elemental steps, which further facilitates the step bunching and causes the instability of step morphology. At the lower left area of the crystal surface, where the solution flow is anti-parallel to the step advancing direction, the steps are smooth and almost no step bunching is observed. Moreover, compared with the case with relatively slow rotation (Fig. 4.5(a)), less step bunching and instability were observed when a higher crystal rotation speed was applied (Fig. 4.5(b)). It can be explained by two factors: 1. Higher crystal rotation better stirred the solution and resulted in more uniform carbon distribution near the crystal surface, which avoided the step bunching caused by supersaturation gradient; 2. The thinner boundary layer caused by higher crystal rotation enabled the solute to diffuse more easily from the bulk solution to the crystal surface, which avoided the step bunching induced by local solute depletion.

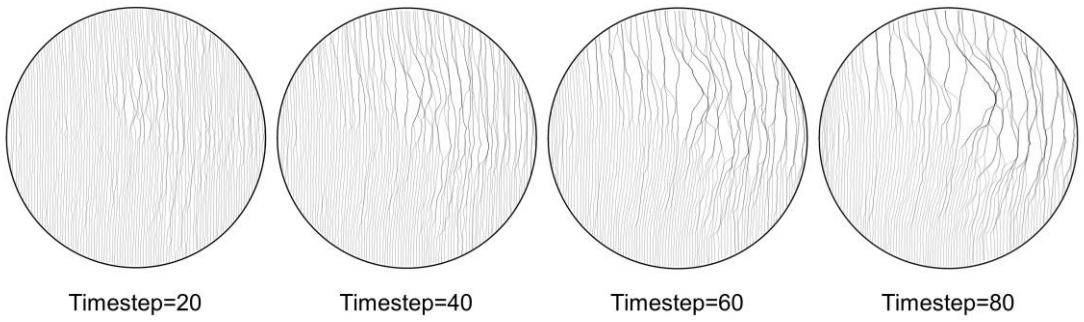

(a)

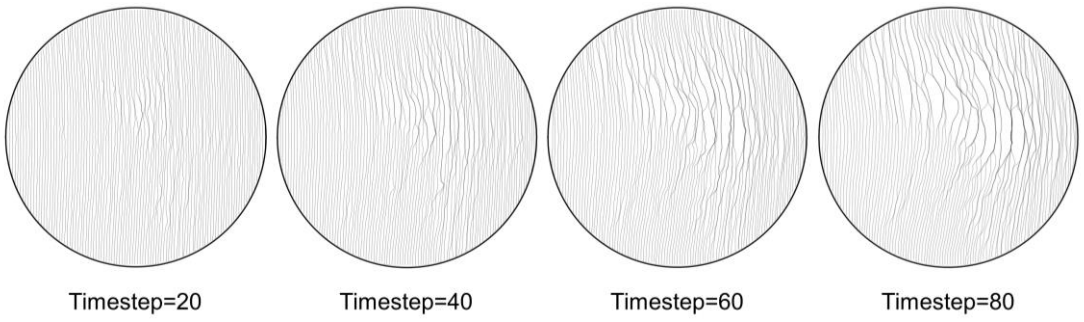

(b)

Fig. 4.5. Evolution of macrostep morphology during 80 timesteps with different crystal rotation speed: (a) 50 rpm and (b) 100 rpm. The step advancing direction is from left to right.

The simulated results were then examined in experiments with 3 hours of growth time. Fig. 4.6(a) presented the crystal grown with 50 rpm crystal rotation. The steps in the lower left area are extremely smooth, which can be barely recognized by the microscope. However, these steps are considered too low to effectively convert the defects from the seed crystal [8]. In contrast, the upper right area exhibits heavy step bunching with wide terraces, indicating the existence of high and steep macrosteps. These macrosteps are capable to achieve defects conversion, but may easily induce the formation of new defects like 2D polytype nucleation and inclusion. For the case with 100 rpm rotation speed (Fig. 4.6(b)), a similar step distribution pattern can be observed but the bunching intensity in the upper right area is lower without extremely wide terrace. Moreover, the high-speed crystal rotation yields larger smooth area on the crystal surface. These tendencies in the experiment match well with those in simulation, validating the effectiveness of the numerical model.

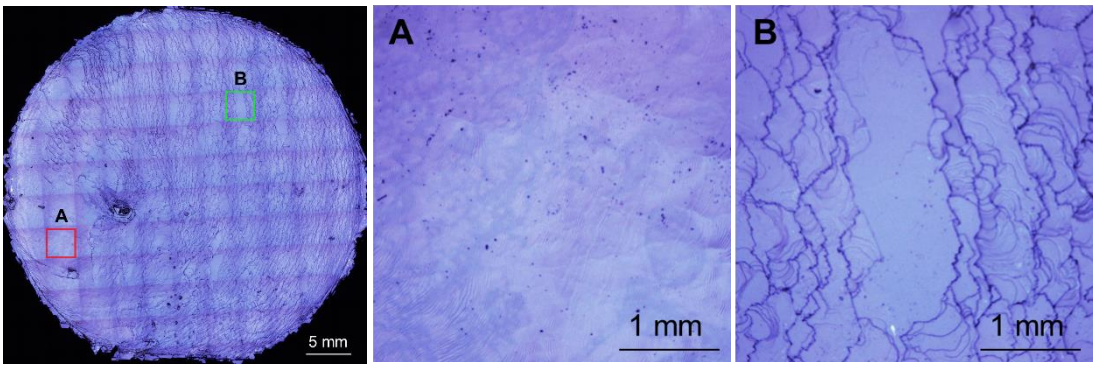

(a)

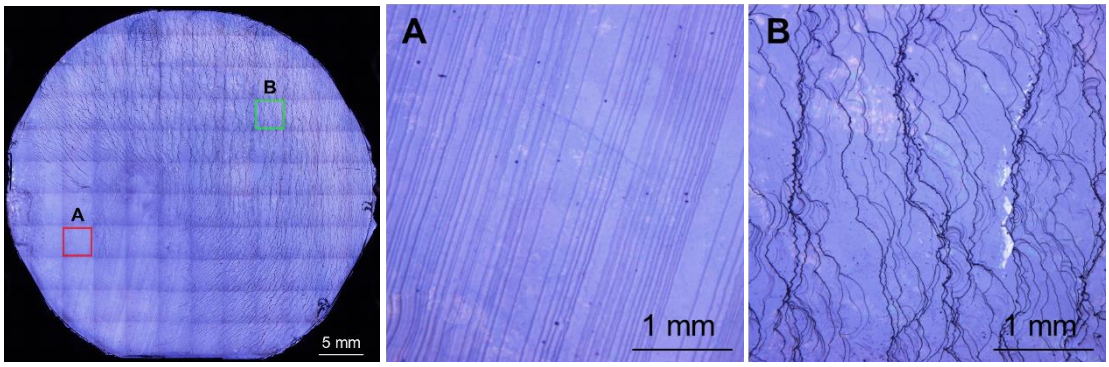

(b)

Fig. 4.6. Step morphology in experiment after 3 hours growth with (a) 50 rpm and (b) 100 rpm crystal rotation speed.

4.3.2 Effect of rotation pattern

Although increasing the crystal rotation speed results in relatively smoother step morphology, the macrostep distribution on the whole surface is still not homogeneous,

resulting in low TSDs conversion efficiency in the lower left area, as well as high inclusion density in the upper right area. This inhomogeneity can be attributed to the incompatibility between the unidirectional step advancing and axisymmetric solution flow. To yield crystal with uniformly distributed macrosteps, a more sophisticated control pattern should be designed, where the proposed simulation method can serve as a powerful tool to connect the experimental controlling parameters and the corresponding step morphology. Firstly, instead of constantly rotating the crystal in one direction, a new rotation pattern is proposed with periodically altering the rotation direction of the crystal (Fig. 4.7(a)). The crystal rotation speed is 50 rpm, while the period for keeping a rotation direction in the simulation is 20 timesteps, and the other growth parameters are the same as those in the previous section. The concept of this rotation pattern is to avoid consistent “parallel flow” underneath a certain area of the crystal surface. Moreover, it has been demonstrated that “anti-parallel flow” can reduce the macrostep height and relieve the local roughness caused by the previous non-ideal condition [11]. This new rotation pattern is tested in the simulation model and the result is shown in Fig. 4.7(b). Compared with constantly rotating the crystal in one direction (Fig. 4.5(a)), rotating in double directions yields relatively more uniform step morphology, without extremely strong bunching and wide terrace in the upper right area. This can be explained that the negative effect of the azimuthal flow in the counter-clockwise (CCW) direction can be offset by the frequent switching to the clockwise (CW) direction. However, the difference in step morphology still exists between the upstream and downstream areas of the crystal, due to the effect of radial flow underneath the crystal which is always from the center to the edge when rotating the crystal (see Fig. 4.3). Therefore the upstream area undergoes consistent anti-parallel flow, while the downstream area undergoes consistent parallel flow, although the intensity of radial flow is lower than that of azimuthal flow.

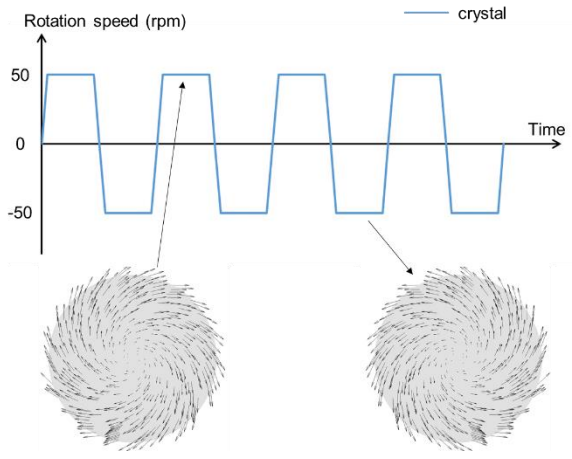

(a)

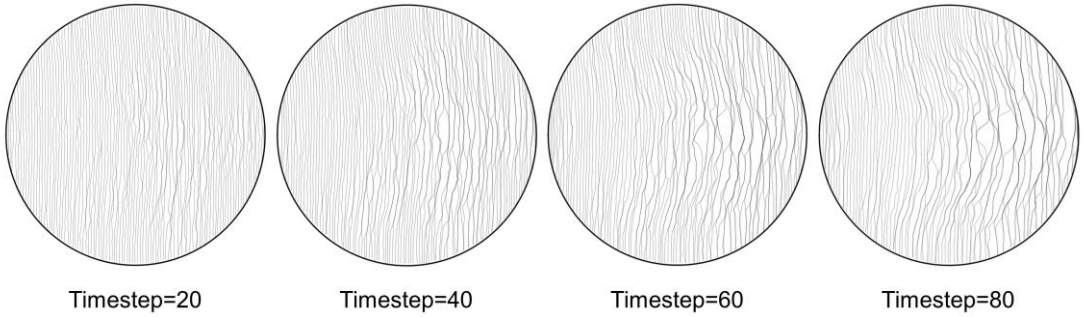

(b)

Fig. 4.7. (a) Rotation pattern 1: periodically switching crystal rotation direction. Note that the crucible was kept stationary; (b) Simulated evolution of step morphology in 80 timesteps.

To further improve the uniformity of step morphology on the whole crystal surface, a more complicated rotation pattern is proposed. This time besides crystal rotation, 40 rpm crucible rotation in double directions is also included in the period (Fig. 4.8(a)). When rotating the crucible, the solution at the bottom will be sent outwards due to the centrifugal force and consequently generate an inward radial flow from the edge to the center underneath the crystal. By frequently switching between the crystal and crucible rotation, it is expected capable to avoid the consistent parallel flow at the downstream area as shown in Fig. 4.7. This rotation pattern is named “switching flow” [18]. Likewise, the simulation model is applied to predict the step morphology under the “switching flow” pattern and the result is shown in Fig. 4.8(b). The switching between crystal rotation and crucible rotation happens every 20 timesteps. After the first 20 timesteps with crystal rotation, the downstream area shows relatively more step bunching, the same as that shown in Fig. 4.7(b). However, in the following 20 timesteps, inward flow caused by crucible rotation makes the situation reversed and results in an equal bunching level between the up and downstream area at the end of the 40th timestep. Finally, by applying the “switching flow” pattern, the uniformity of step morphology on the whole crystal surface was significantly improved where no heavy bunching and wide terrace can be observed. This morphology is expected to achieve both high TDs conversion rate, and low inclusion density. The crystal grown under the same condition in the experiment shows the same tendency (Fig. 4.8(c)), where the macrosteps with medium height are ordered straightly and smoothly on the whole crystal surface. This can be explained that for a local giant macrostep formed during parallel flow, it will be decomposed into small macrosteps in the subsequent anti-parallel flow period. Therefore, frequent switching of flow direction (both azimuthal and radial) underneath the crystal yields steps with ideal bunching level and high uniformity, which is a

promising method to grow high-quality SiC crystal on the off-axis substrate. Moreover, the effectiveness of the simulation model is further validated.

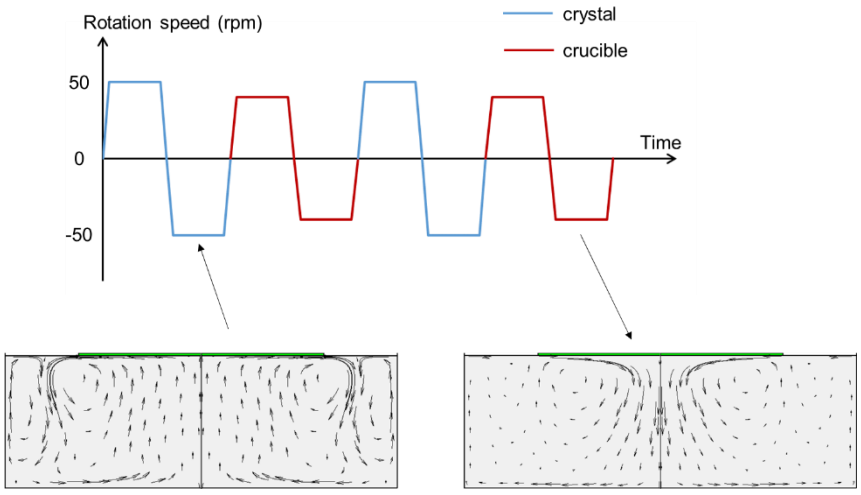

(a)

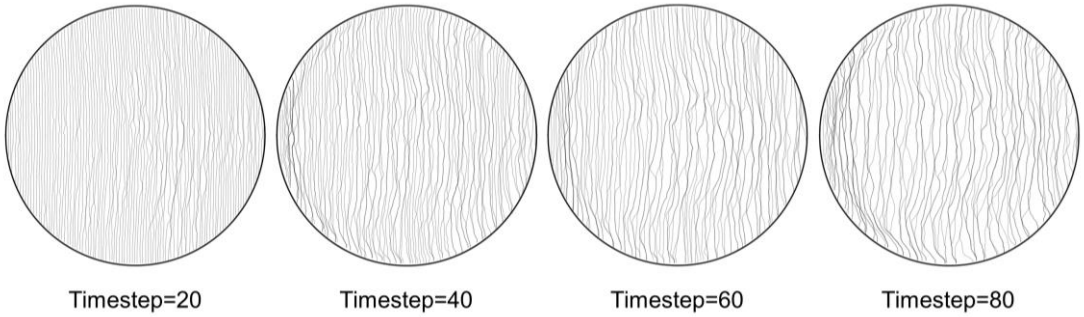

(b)

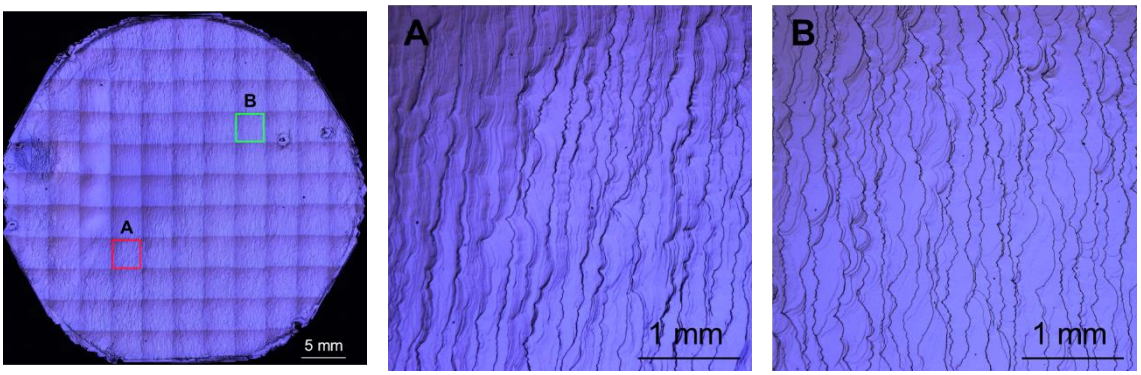

(c)

Fig. 4.8. (a) Rotation pattern 2: periodically switching crystal and crucible rotation. Note that the crucible was kept stationary during crystal rotation, and vice versa; (b) Simulated evolution of step morphology in 80 timesteps; (c) Step morphology after 3 h growth.

4.3.3 Effect of switching pattern

Based on the results in the previous section, a uniform step morphology with ideal macrostep height on the entire off-axis crystal surface could be achieved by frequently switching the flow, both in azimuthal and radial directions. However, unlike constantly rotating the crystal in one direction, the control pattern of "switching flow" is sophisticated with at least 4 independent control parameters, namely, rotation speeds of crystal and crucible, and time for rotating crystal and crucible, respectively (shown in Fig. 4.9). To further optimize the step morphology, the effect of these parameters should be understood.

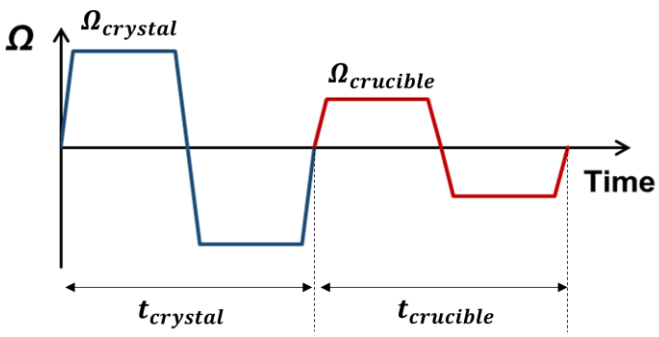

Fig. 4.9 Schematic of control pattern of "switching flow". Note that crystal or crucible rotates only in the corresponding period.

Rotation speed matching

Firstly, three simulation cases, with the same crystal rotation speed but different crucible rotation speeds, are conducted to investigate the effect of rotation speed matching in the switching flow pattern shown in Fig. 4.9. The crystal rotation speed is 50 rpm for the crystal rotation period, while the crucible rotation speeds are 20, 40 and 60 rpm, respectively, for the crucible rotation period. Fig. 4.10 shows the effect of crucible rotation on the flow field inside the solution domain. With faster crucible rotation, the radial flow from the edge to the center of the crystal is significantly intensified, which will affect the carbon transport behavior in the solution and consequently the step morphology. To further illustrate the matching between crystal and crucible rotation, the radial velocity of solution at the boundary layer surface is extracted from the 2D global simulation for each case. As can be seen from Fig. 4.11, when rotating the crucible at 20 or 60 rpm, the inward flow (from edge to center) is either too weak or too strong compared with the outward flow (from center to edge) generated by rotating the crystal with 50 rpm. This unbalance is expected to cause morphology difference between upstream and downstream areas.

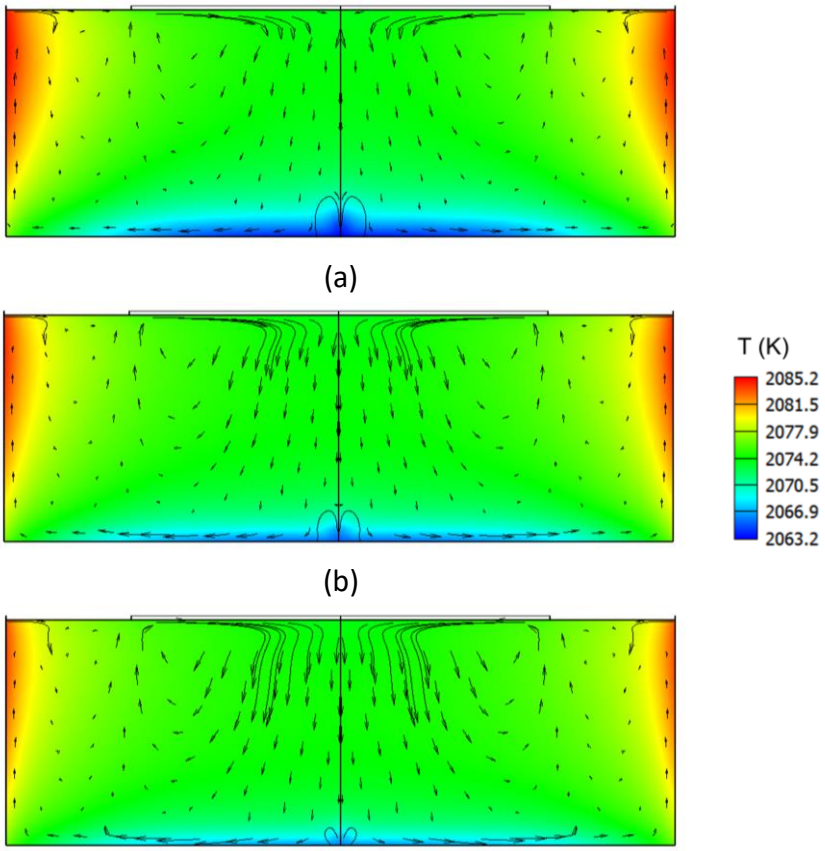

(a)

(b)

(c)

Fig. 4.10 Thermal and flow fields in solution with different crucible rotation speed: (a) 20 rpm; (b) 40 rpm; (c) 60 rpm. Note that the crystal was kept stationary.

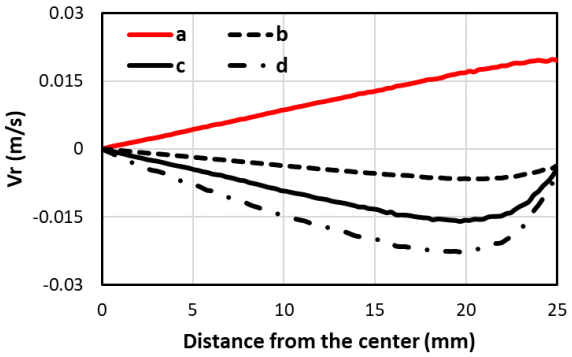

Fig. 4.11 Comparison of radial velocities with different conditions: (a) 50 rpm crystal rotation; (b) 20 rpm crucible rotation; (c) 40 rpm crucible rotation; (d) 60 rpm crucible rotation.

The three “switching flow” patterns are then simulated to compare the step development. As seen in Fig. 4.12(a), the combination of strong outward flow and weak

inward flow yields unbalanced step distribution, where the upstream area is smoother than the downstream area. The distribution is exactly the opposite in the case where inward flow is dominant (Fig. 4.12(c)). Only the combination of 50 rpm crystal rotation and 40 rpm crucible rotation results in a uniform step distribution with a medium bunching level all over the crystal surface (Fig. 4.12(b)). This indicates that a good matching between inward and outward flow is required when designing the "switching flow" pattern.

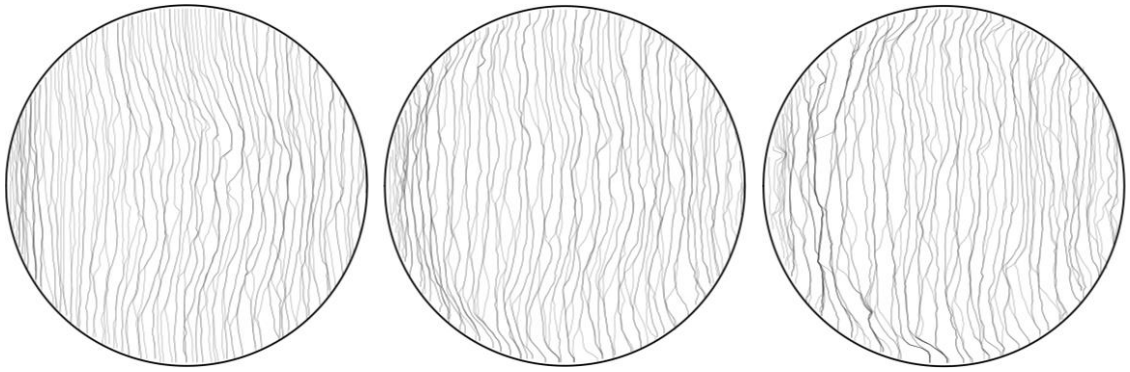

(a) (b) (c)

Fig. 4.12 Step morphology after 80 timesteps with different "switching flow" pattern: (a) $\Omega_{crystal}$=50 rpm, $\Omega_{crucible}$=20 rpm; (b) $\Omega_{crystal}$=50 rpm, $\Omega_{crucible}$=40 rpm; (c) $\Omega_{crystal}$=50 rpm, $\Omega_{crucible}$=60 rpm

Switching frequency

Another parameter that determines the "switching flow" pattern is the switching frequency between inward and outward flow, in other words, the duration of rotating crystal and crucible. To investigate the effect of this factor on step morphology evolution, two cases are compared with the same rotation speeds ($\Omega_{crystal}$=50 rpm, $\Omega_{crucible}$=40 rpm) but different switching frequencies. In the slow-switching case, $t_{crystal}$=$t_{crucible}$=20 timesteps, while in the fast-switching case, $t_{crystal}$=$t_{crucible}$=4 timesteps. The step morphologies after 80 timesteps for both cases are shown in Fig. 4.13. The fast-switching case yields smoother surface morphology and lower step bunching level. This can be explained that the surface roughness caused by step bunching increases almost exponentially under the consistent parallel flow condition (see in Fig. 4.5(a) and Fig. 4.7(b)). Through fast switching the flow direction, the slightly bunched macrosteps can be frequently de-bunched to a relatively low level. However, in the case of slow switching, the macrosteps may be over-developed during the local parallel flow period and the de-bunching effect in the following anti-parallel period is therefore limited. This result indicates that the step bunching level can be freely

controlled by adjusting the switching frequency between different solution flow directions underneath the crystal.

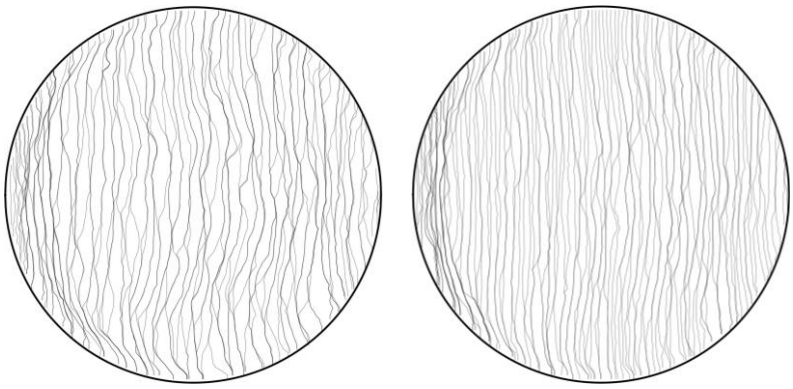

(a) (b)

Fig. 4.13 Step morphology after 80 timesteps with (a) slow switching and (b) fast switching.

4.4 Conclusion

In this chapter, a simulation method is proposed, which can predict and visualize the evolution of macrosteps morphology on the entire crystal surface during solution growth of SiC. The simulation method consists of three parts, namely 1. a 2D global CFD model to predict the thermal, flow, and mass fields in the system under certain control parameters; 2. a 3D local CFD model to simulate the carbon transport inside the boundary layer underneath the crystal; 3. a kinetics model to calculate the step advancing velocity coupling with the carbon concentration near the surface.

The simulation method is firstly applied to investigate the effect of crystal rotation speed on step morphology. The result shows that with consistently rotating the crystal in one direction, the step morphology in the upper right area of the crystal is rough, while that in the lower right area is smooth, due to the co-effect of radial and azimuthal flow underneath the crystal surface. Moreover, higher rotation speed yields better surface morphology with less bunching at upper right area, owing to the thinner boundary layer and more uniform carbon distribution near the crystal. The tendencies shown in the simulation results match well with those in experiments.

The simulation method is then utilized to design a more sophisticated control pattern, corresponding to uniform step morphology and medium step height on the entire crystal surface. The result shows that by frequently switching the flow direction in both azimuthal and radial directions, the severe step bunching at a certain location can be avoided. A so-called “switching flow” pattern, including periodically rotating the crystal or crucible, is regarded as the promising method to achieve ideal step morphology. The

simulation results suggest that a good matching between crystal and crucible rotation speed yields a more homogeneous step distribution, while high-frequency switching results in smoother morphology with lower bunching level.

The above results indicate that the step morphology on an off-axis crystal is controllable. The proposed simulation method can serve as a powerful tool for designing the sophisticated control pattern, and explaining the phenomena of step behavior in a macroscope. This method can also be applied to other crystal growth from solution.

References

[1] H. Tsuchida, R. Takanashi, I. Kamata, N. Hoshino, E. Makino, J. Kojima. *J. Cryst. Growth* 2014, 402, 260-266.

[2] S. Xiao, S. Harada, K. Murayama, M. Tagawa, T. Ujihara. *Cryst. Growth Des.* 2016, 16, 6436-6439.

[3] C. Zhu, S. Harada, K. Seki, H. Zhang, H. Niinomi, M. Tagawa, T. Ujihara. *Cryst. Growth Des.* 2013, 13, 3691-3696.

[4] J.P. Van Der Eerden. *Electrochim. Acta* 1986, 31, 1007-1012.

[5] A.A. Chernov. *J. Cryst. Growth* 1992, 118, 333-347.

[6] H. Daikoku, M. Kado, A. Seki, K. Sato, T. Bessho, K. Kusunoki, H. Kaidou, Y. Kishida, K. Moriguchi, K. Kamei. *Cryst. Growth Des.* 2016, 16, 1256-1260.

[7] Y. Yamamoto, S. Harada, K. Seki, A. Horio, T. Mitsuhashi, T. Ujihara. *Appl. Phys. Express* 2012, 5, 115501.

[8] X. Liu, C. Zhu, S. Harada, M. Tagawa, T. Ujihara. *CrystEngComm* 2019, 21, 7260-7065.

[9] F. Durand, J.C. Duby. *J. Phase Equilib.* 1999, 20, 61-63.

[10] J.A. Burton, R.C. Prim, W.P. Slichter. *J. Chem. Phys.* 1953, 21, 1987-1991.

[11] X. Liu, Y. Dang, K. Suzuki, C. Zhu, W. Yu, S. Harada, M. Tagawa, T. Ujihara. *J. Cryst. Growth* 2022, 578, 126425.

[12] I.V. Markov. *Crystal growth for Beginners: Fundamentals of Nucleation, Crystal Growth and Epitaxy, 3rd ed.*, World Scientific, New Jersey, 2016.

[13] V.I. Marchenko, A.Y. Parshin. *Sov. Phys. JETP* 1980, 52, 129-131.

[14] J. Tersoff. *Phys. Rev. Lett.* 1995, 75, 2730-2733.

[15] J. Lefebure, J. Dedulle, T. Ouisse, D. Chaussende. *Cryst. Growth Des.* 2012, 12, 909-913.

[16] E. Pearson, T. Takai, T. Halicioglu, W.A. Tiller. *J. Cryst. Growth* 1984, 70, 33-40.

[17] M. Bauccio. *ASM Engineering Materials Reference Book, 2nd ed.*, Material Park, OH: ASM International, 1994.

[18] C. Zhu, T. Endo, H. Lin, H. Koizumi, S. Harada, M. Tagawa, T. Ujihara. *19th International Conference on Crystal Growth and Expitaxy (ICCGE-19)*, 2019.

5. Conclusion

This study aimed to improve the solution growth method for producing high-quality 4H-SiC crystals with large thickness. We focused on the three unstable phenomena that make the growth deviate from the well-designed initial condition during long-term growth. These phenomena hinder the crystal from growing larger. Three numerical models were constructed to investigate the instabilities of crucible configuration, solution composition, and step morphology, respectively. Accordingly, optimized or improved approaches were proposed to enable longer growth time with better crystal quality. Here, the knowledge obtained in each chapter is summarized below.

Chapter 1 introduced the basic background of this study, including the superiority of SiC, the advantage of the solution growth method to produce SiC crystals, and the current problems limiting the competitivity and prevalence of the solution growth method. Moreover, the basic concepts of the numerical models utilized in the following chapters were introduced.

In chapter 2, the instability of crucible configuration due to single crystal growth, crucible dissolution, and polycrystals precipitation was investigated. A global 2D CFD model was built to simulate these unsteady factors in the solution growth system of SiC. It was found that the original control recipe with fixed parameters was incapable of growth over 50 h, due to both quality and safety problems. To overcome this, a machine learning-based optimization approach was established to design a time-dependent recipe with a 100-timestep sequence. In each timestep, machine learning models were trained to instantly provide an accurate prediction of the unsteady changes and were combined with the optimization algorithm to determine the most suitable control parameters adaptive to the environment. Compared with the original recipe, the optimized dynamic recipe achieved 30% thicker single crystal, flatter crystal surface, and 50% longer available growth time. This discovery demonstrated the importance of dynamic adaptive control for long-term SiC solution growth and other material fabrication process with unsteady features. Furthermore, the application of transfer learning was discussed to further enhance the efficiency of the optimization approach.

In chapter 3, the instability of solution composition due to the evaporation of Al was investigated, since Al plays an important role as both p-type dopant and surface stabilizer in solution growth of SiC. A 2D global CFD model was built to simulate the evaporation, transportation, and reaction of Al during the long-term growth process, with the solution composition of $Si_{0.58}Cr_{0.4}Al_{0.02}$. The detailed transport path of Al was determined through

thermodynamics analysis. To better preserve the Al in solution during long-term growth and enhance the composition stability, a so-called “fin” structure was proposed. The simulation result showed that the existence of the fin structure had little effect on the thermal and flow condition for SiC crystal growth in the solution, but could significantly suppress the transport and consumption of Al vapor in the gas phase. By applying the fin structure, after 20 h growth, the Al concentration left in the solution was about 1.7 times higher than that in the original case. The simulated result was subsequently validated by experiments. Compared with the original case, the improved case with the fin structure could effectively eliminate the spontaneous nucleation particles and yield higher steps on the crystal surface. The result indicates the importance of evaporation suppression during long-term growth.

In chapter 4, the instability of step morphology due to step bunching was investigated. Since solution growth is a diffusion-limiting process, and the step behavior depends largely on solution flow near the crystal surface, a simulation method was constructed to predict and visualize the evolution of macrosteps morphology on the entire crystal surface coupled with mass and flow field in the solution domain. The simulation method consists of three parts, namely a 2D global CFD model of the entire growth system, a 3D local CFD model of the boundary layer, and a kinetics model of the steps on the surface. The simulation method was first applied to investigate the effect of crystal rotation speed on step morphology. The result shows that consistently crystal rotating in a single direction yields non-uniform distribution of step morphology, and higher rotation speed results in relatively smooth surface morphology with less bunching. The tendencies shown in the simulation results match well with those in experiments. The simulation method is then utilized to design a more sophisticated control pattern, corresponding to uniform step morphology and medium step height. By frequently switching the flow direction in both azimuthal and radial directions, the severe step bunching at a certain location can be avoided. The results indicate that the step morphology on an off-axis crystal is controllable during long-term growth, while the simulation method proposed can serve as a powerful tool to design the control pattern.

Above all, the three factors enabling long-term stable solution growth of SiC are, dynamic thermal and flow control, less mass exchange between the liquid and gas phase, and avoiding consistent local solution flow direction parallel to the step movement.

Appendix A: Training process and performance of transfer learning

In section 2.4, a transfer learning approach was introduced to accelerate the optimization of the time-dependent control recipe. In this appendix, the training process, transfer method determination, and the performance of transfer learning are introduced in detail for a better understanding of transfer learning.

A.1 Training process

Table A1 shows the lower and upper limits of each control parameter when preparing the training data. T is the temperature at the monitoring point, according to which the heating power is adjusted. Higher T results in more carbon dissolving from the crucible and consequently accelerates crystal growth. ΔH is the crucible position relative to the induction coil, which determines the distribution of Lorentz force and induction heating in the solution domain. The centrifugal force caused by the rotation of crystal ($\omega_{crystal}$) and crucible ($\omega_{crucible}$) influences the flow pattern, and consequently the carbon transport path. The representative plots of raw data are plotted to characterize the crystal growth process. The model predicting the growth rate of the single crystal is taken as an example. Fig. A1 (a-e) shows the relationships between the inputs of the model (control parameters as well as the radial coordinate) and the output (single crystal growth rate) in timestep 1. It should be noted that the interval of the crucible position value is 10 mm when preparing training data, because the spatial discretization of the geometric model is time-consuming for CFD simulation. It can be concluded that the growth rate increases with growth temperature, the absolute value of crystal rotation speed, and crucible position. Moreover, the edge of the crystal tends to grow faster than the center area.

Fig. A1 (f-j) show the same representative plots in timestep 2. The relationships between the inputs and output are similar to those in time step 1. This indicates the existence of similar features between the source domain (timestep 1) and the target domain (timestep 2), which is the prerequisite to applying transfer learning.

Table A1. Training data range

Parameter	Lower limit	Upper limit

Temperature, $T\ (K)$	2073	2273
Crucible position, $\Delta H\ (mm)$	50	150
Crystal rotation speed, $\omega_{crystal}\ (rpm)$	-50	50
Crucible rotation speed, $\omega_{crucible}\ (rpm)$	0	20

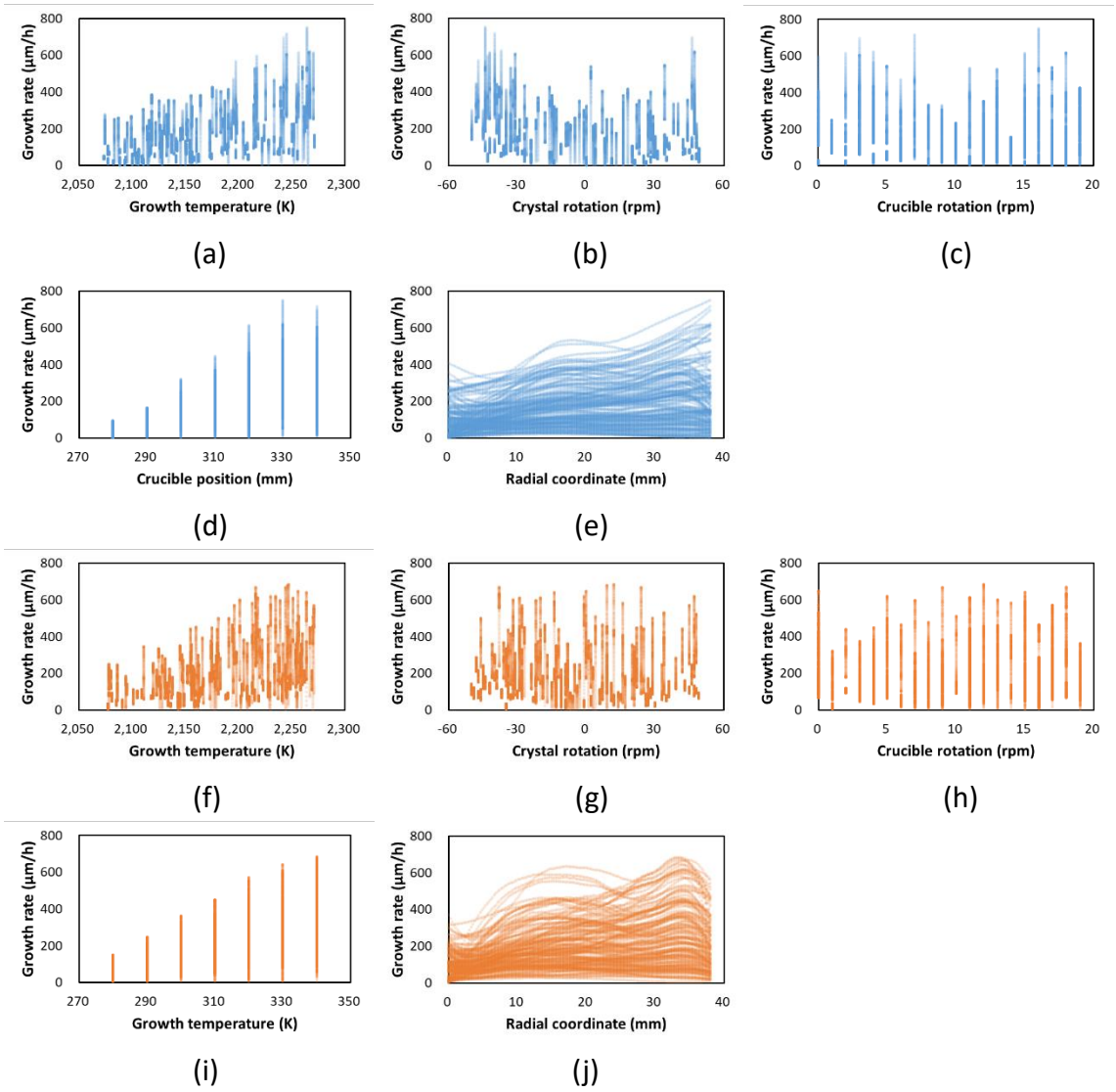

Fig. A1. (a-e) Relationships between the inputs and output of the neural network in timestep 1; (f-j) Relationships between the inputs and output of the neural network in timestep 2. The neural network that predicts the single crystal growth rate is taken as an example.

Fig. A2(a) shows the learning curve of the source neural network in timestep 1 using sufficient data (100%). The model is trained from scratch and the learning process converges after more than 400 epochs. The learning curve of the transferred

model with 20% amount of data is shown in Fig. A2(b). Here “fine tuning” is selected as the transfer method. The initial value of the mean average error is relatively small, indicating the successful inheritance of knowledge from the source model. The training is quickly stopped after about 25 epochs since the concept of transfer learning is to slightly adjust the weights and bias based on the source model and further training will result in overfitting due to lack of data. The transferred model shows good performance in predicting the growth rate (Fig. A2(d)).

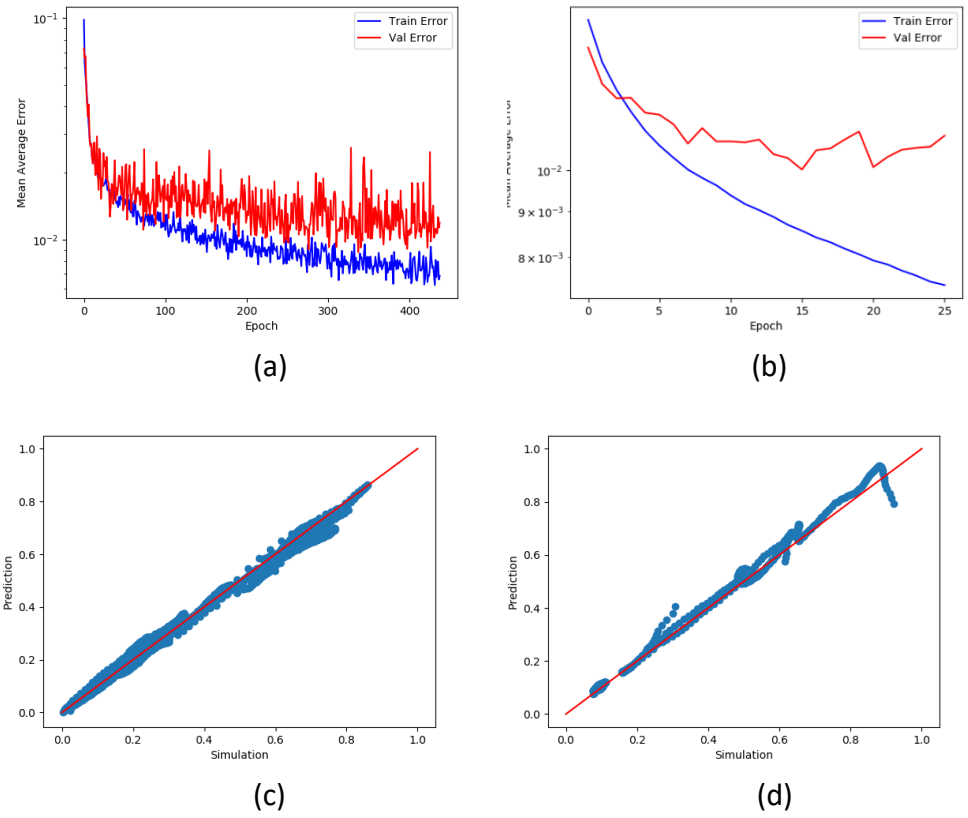

Fig. A2. The learning curves and training results of (a, c) the source model in timestep 1, and (b, d) the transferred model trained with 20% data in timestep 2. The neural network predicting the seed growth rate is taken as an example.

A.2 Determination of transfer learning method

To investigate the effect of the transfer learning method on model performance, six different models are constructed and trained with different strategies, including all possibilities of “frozen featurizer” and “fine tuning”, to predict the growth rate (V_g) on the single-crystal surface in the second timestep (timestep length Δt =1 h). 90 simulation cases (60%) are prepared and split into training and test sets in a ratio of 9:1. Due to the

relatively small amount of training data, 10-fold cross-validation is applied. The values of the MAE for all 10 folds are shown in Fig. A3.

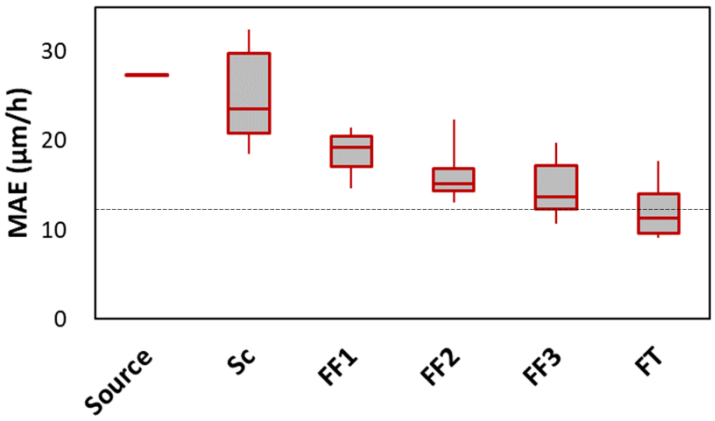

Fig. A3. Performance of various models trained with 60% of data in the updated timestep. "Source" refers to direct application of the source model without updating, "Sc" refers to training from scratch without any transfer, "FF n" refers to freezing the first n shallower layers using the frozen-featurizer method, and "FT" refers to fine tuning. The black dashed line shows the performance of the source model in the initial timestep for reference.

According to Fig. A3, although the geometric difference between the initial timestep and the updated timestep is quite small (~0.1 mm), the source model is not capable of directly predicting the new growth rate. Moreover, all of the transfer learning methods effectively improve the model performance compared with the trained-from-scratch model. Among them, fine tuning shows the best performance, which is at the same level as that for the source model trained with the whole dataset in the initial timestep. In the cases of crucible dissolution rate (V_d) and polycrystal precipitation rate (V_p), fine tuning also presents better performance than other transfer learning methods. Therefore, fine tuning is selected as the only transfer learning method in the rest part of the discussion.

A.3 Effect of time step length

In the current simulation, the evolution of the geometric model is governed by

$$\Delta l = V \Delta t \qquad \text{(Eq. A-1)}$$

where Δl is the displacement of the interface, V is the growth, dissolution, or precipitation rate, and Δt is the time step length, which directly determines the geometric difference in the solution domain between the initial time step and the updated time step. We previously discussed the high data efficiency of transfer learning

when the geometric difference between two timesteps is not large (Δt =1 h). To test the sensitivity of the transferred model to timestep length and find the criterion where the transferred model may fail to inherit the features, transfer learning is applied in different cases with Δt values of 1, 5, 10, 20, and 50 h. The performance of the transferred models is plotted in Fig. A4(a). For the models trained with 100% and 60% of the data, accuracy is mostly independent of Δt, and the MAE values are relatively low, even for a large Δt (50 h). The model trained with 20% of the data has low MAE values when Δt is not large, but loses accuracy when Δt =50 h. To explain this result, the geometries of the solution domain as well as the thermal distribution and flow pattern under the same control parameters after 1, 20, and 50 h are shown in Fig. A4(b-d). Compared with the other two cases, the flow pattern and thermal distribution change significantly for Δt =50 h due to the large displacement of boundaries, which is considered to have greatly affected the corresponding features between inputs and outputs. For transferred models trained with relatively more data, this large change can be adjusted and rectified to fit the new feature space. However, the model trained with only 20% of the data might be incapable of adjusting for this large change. Note that time step lengths of 20 and 50 h are too long for practical unsteady simulation; they are applied here only for testing the limitation of transfer learning. The results therefore show that the transferred model trained with 20% of the data is capable of predicting the unsteady changes in practical applications.

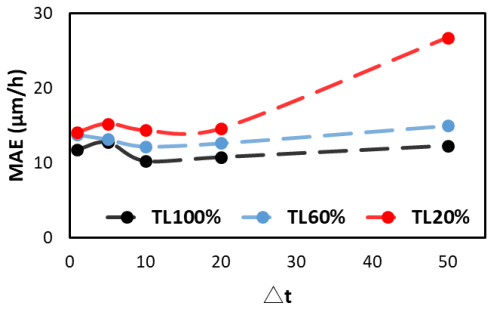

(a)

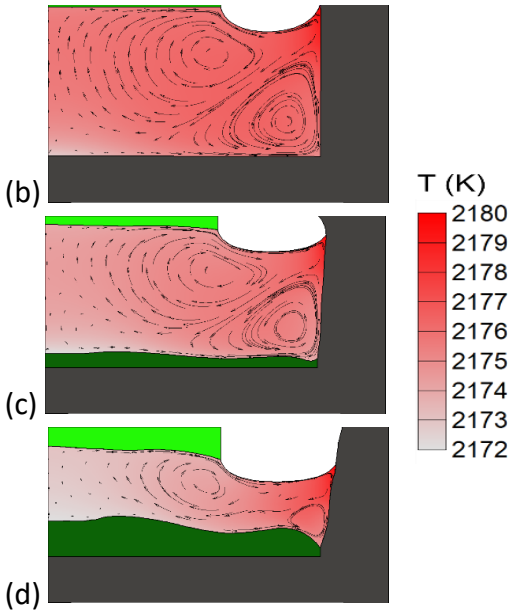

Fig. A4. (a) Effect of time step length on performance of transferred models trained with various amounts of data. (b-d) Temperature and velocity fields in updated solution domain with time step length of 1, 20, and 50 h, respectively.

Appendix B: Turbulence, devil or angel?

In the main body of this dissertation, when conducting the 2D global or 3D local CFD simulation, the flow inside the solution domain was always assumed as steady state. Therefore, the Reynolds-averaged approach was employed to represent the transport equation for the mean flow quantities, and to save computation resource. However, when expanding the system for growing 6-inch crystal, the effect of turbulence becomes nonnegligible, because of the relatively low-frequency magnetic field applied (3k Hz), the large size of the crucible (over 200 mm in diameter), and the high rotation speed of both crystal and crucible (up to 100 rpm). For example, when rotating both the crystal and crucible at 50 rpm in the 6-inch growth system, the dimensionless numbers representing the effect of Lorentz force, Marangoni force, buoyancy force, and the centrifugal force caused by crystal and crucible rotation are listed in Table B1. The dimensionless numbers indicate the existence of turbulence, dominated by the inducted Lorentz force.

Table B1. Dimensionless numbers describing the effects of different forces in a 6-inch growth system (values of parameters are listed in Table B2)

Force	Expression [1, 2]	Value
Lorentz force	$EM = F_{E,max}R_{cru}^3/(\rho\upsilon^2)$	6.7×10^{10}
Marangoni force	$Re_\sigma = \sigma_T \Delta T_{sur} R_{cru}/(\rho\upsilon^2)$	8.9×10^5
Buoyancy force	$Gr = g\beta\Delta T_{sol}R_{cru}^3/\upsilon^2$	8.9×10^7
Centrifugal force by crystal rotation	$Re_{cry} = 2\pi\Omega_{cry}R_{cru}R_{cry}/60\upsilon$	1.2×10^5
Centrifugal force by crucible rotation	$Re_{cru} = 2\pi\Omega_{cru}R_{cru}^2/60\upsilon$	1.7×10^5

Table B2. Values of parameters used for calculating the non-dimensional numbers

Parameter	Symbol	Value	Unit
Max Lorentz force	$F_{E,max}$	1.5×10^5	N m^{-2}
Radius of crystal	R_{cry}	7.5×10^{-2}	m
Radius of crucible	R_{cru}	1.1×10^{-1}	m
Solution density	ρ	2.6×10^3	kg m^{-3}
Viscosity	υ	3.3×10^{-7}	m^2 s^{-2}
Surface tension coefficient	σ_T	2.5×10^{-4}	N m^{-1} K^{-1}
Temperature difference at free surface	ΔT_{sur}	2.3	K
Temperature difference in solution	ΔT_{sol}	6	K
Thermal expansion coefficient	β	1.4×10^{-4}	K^{-1}

Turbulence has been discussed in the melt growth of crystalline silicon as an important research topic for decades [3]. In most cases, it was considered to be unstable and harmful since the strong fluctuation caused by turbulence results in undesirable growth interface and compositional striations in grown crystal, which lead to inhomogeneous material and electronic properties. Therefore, several approaches were proposed to suppress the turbulence and fluctuation in the melt, including crystal/crucible rotation [1], magnetic fields [4], and additional electric currents [5].

Nevertheless, the effect of turbulence is not this intuitive when talking about crystal growth from solution. On one hand, similar to that in melt growth, the fluctuation of temperature and supersaturation may disturb the crystallization front and cause uncontrolled nucleation. On the other hand, the turbulent flow may enhance the momentum, heat and mass transport. The enhanced transport is expected to improve the homogeneity of solute distribution and thusly benefit the step development on the crystal surface. In this appendix, the effect of turbulence is discussed from these two aspects.

B.1 Disadvantage

To study the unsteady features caused by turbulence, the large eddy simulation (LES) technique is used. Details of this method can be found somewhere else [6]. A local 3D geometric model is constructed to simulate the momentum, heat and mass transport only in the solution domain. The boundary conditions of temperature at the crystal surface, solution free surface and crucible wall, as well as the source terms for Lorentz force (F_E) and Joule heat are extracted from the 2D global simulation result. The timestep is 0.1 s. The schematic of the calculation configuration and grids are shown in Fig. B1.

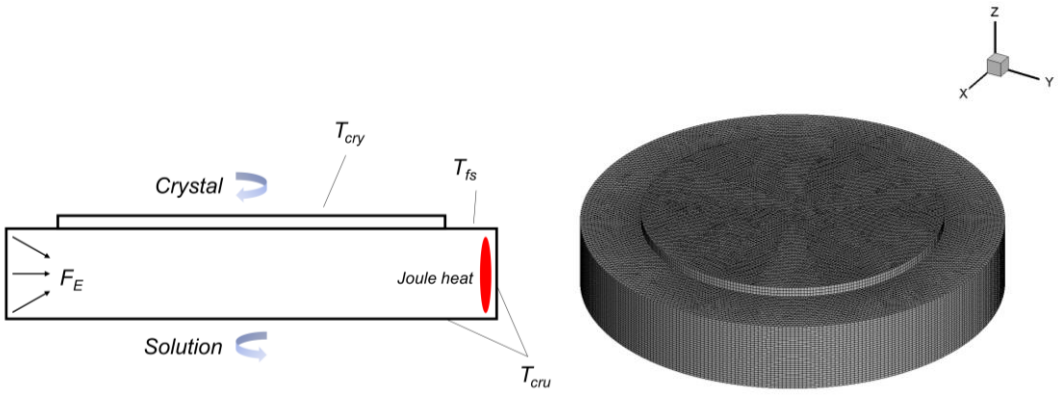

(a) (b)

Fig. B1. The schematic of (a) model configuration, and (b) spatial discrete grids for calculation. The total grids number is ~0.9 million.

To investigate the effect of turbulence intensity on the grown crystal, two cases with the same condition except for the rotation speeds are conducted. In case 1, the rotation rate of the crystal and crucible are 0 and 20 rpm, while in case 2 they are 50 and 50 rpm. Here the rotation speed is selected as the variable because it is the most convenient parameter to modify in the practical growth system and the previous study demonstrated that faster crucible rotation could suppress the temperature fluctuation caused by turbulence [7].

The transient temperature distributions of the two cases are compared in the cross-section of the solution domain (Fig. B2) and horizontal plane 0.3 mm underneath the crystal surface (Fig. B3). For case 1, the temperature and flow fields exhibit an obvious asymmetric feature, indicating the existence of strong fluctuation in the liquid phase. In contrast, this asymmetric feature is eliminated by the high rotation rate of the crucible in case 2, where the growth condition is relatively steadier.

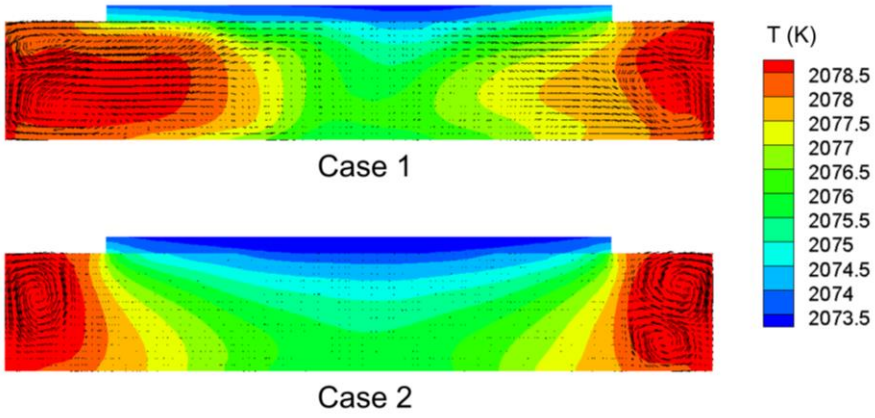

Fig. B2. Transient temperature and flow fields in the cross section of solution domain.

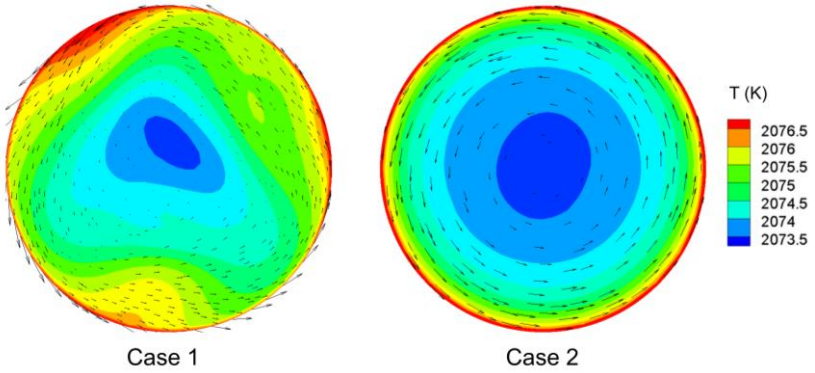

Fig. B3. Transient temperature and flow fields in the XY direction near the crystal surface.

To further evaluate the effect of crucible rotation on suppressing the fluctuation, the supersaturation at a monitoring point (0.6 mm away from the center, 0.3 mm under the crystal surface) is recorded within 100 s calculation. As shown in Fig. B4, due to the fast rotation of the crucible, the strong supersaturation fluctuation can be converted into relatively weak fluctuation but with a higher frequency.

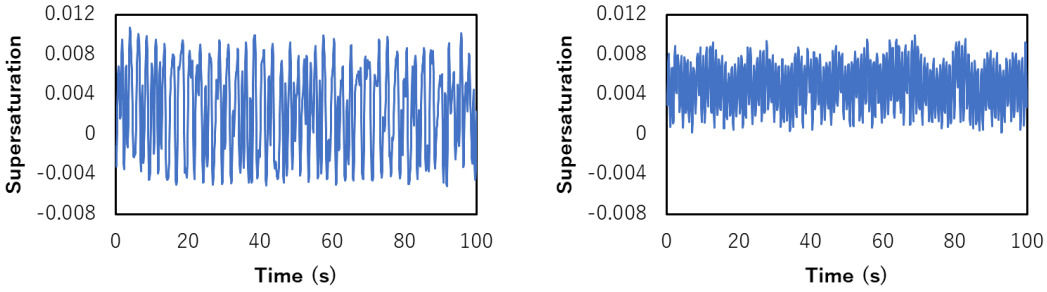

(a) (b)

Fig. B4. Time-dependent supersaturation recorded at the monitoring point in 100 s for (a) case 1, and (b) case 2.

The crystals grown under the two conditions are presented in Fig. B5. The crystal grown in case 1 has several spontaneous nucleation particles attached to the surface, which is normally attributed to disturbing the step flow and introducing new dislocations. The particles are of various sizes, and are therefore considered to consistently originate from the 3D nucleation in solution during the growth process. In contrast, the crystal grown in case 2 shows a clean surface without the particles. Note that the gray circle on the surface is the residual solution left when pulling up the crystal from the solution after growth, other than the particle. This difference can be explained by the classic nucleation theory, where the 3D nucleation rate J in the solution can be expressed as [8]:

$$J = Ne^{-\Delta G^*/kT} \quad \text{(Eq. B-1 a)}$$

$$\Delta G^* = \frac{f v^2 \gamma^3}{(\Delta\mu)^2} \quad \text{(Eq. B-1 b)}$$

where N represents the collision frequency of the molecules, ΔG^* the variation of Gibbs free energy, f the morphological factor, v the molecular volume, γ the interfacial energy, and $\Delta\mu$ the driven force of crystallization. In the case with strong turbulence (case 1), the value of N is larger due to the stirring and collision between eddies. Moreover, the supersaturation can reach a higher value owing to the strong fluctuation (Fig. B4(a)), providing large driven force. Therefore, the large N and $\Delta\mu$ result in frequent 3D nucleation inside the solution. These nucleated particles are transported

by convection and consequently attached to the crystal surface. In case 2, the 3D nucleation in solution is suppressed by relatively weak turbulence.

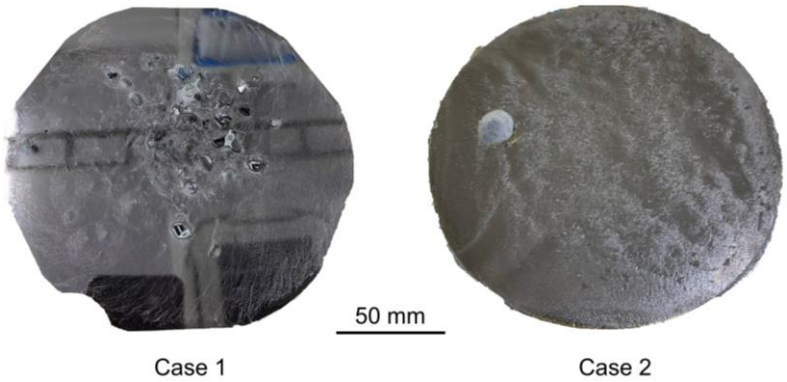

Fig. B5. Crystals grown under the conditions of case 1 (left) and case 2 (right).

B.2 Advantage

The analysis in the previous section suggested that the crystal grown under weak turbulence condition is better with less 3D spontaneous nucleation. However, when having a closer look at the crystal surface, the tendency is the opposite (Fig. B6). On the surface of the crystal in case 1, arrayed macrosteps can be observed, indicating a step flow growth mode. In contrast, on the crystal in case 2, step flow can barely be observed. Instead, dendritic growth is dominant with clear boundaries between growth domains. This morphology is normally caused by severe step instability, and will result in inclusion, polytype and other quality problems. This comparison suggests that besides 3D nucleation in solution, turbulence may also positively influence the step morphology on the crystal surface.

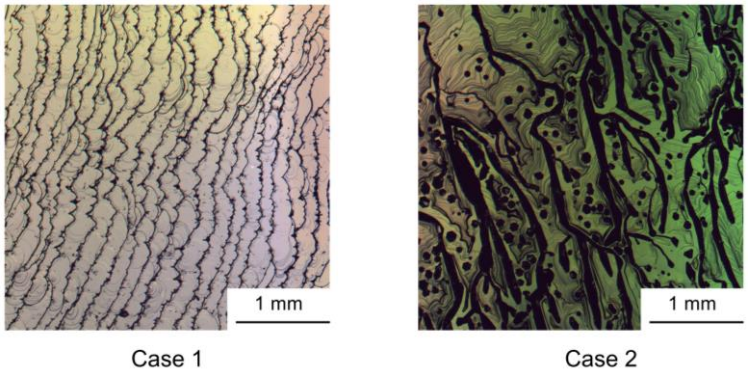

Fig. B6. Crystals grown under the conditions of case 1 (left) and 2 (right).

The simulation method proposed in Chapter 4 is utilized to investigate the effect of turbulence on step morphology. The time-dependent fluctuation of temperature, velocity and carbon concentration near the crystal surface are extracted from the LES

simulation of case 1 shown in the previous section, and set as the boundary condition for the local simulation inside the stagnant layer. In the comparison case, the time-averaged value without fluctuation is set as the boundary condition. Fig. B7 shows the step development for both cases. The result illustrates that the fluctuation of supersaturation caused by turbulence does not affect the overall step morphology distribution, but will lead to local zig-zag-shaped steps especially at the edge of the crystal, where the fluctuation is stronger. This zig-zag shape is considered harmful for the crystal quality since it will result in further instability of steps, and consequently the inclusion [9, 10].

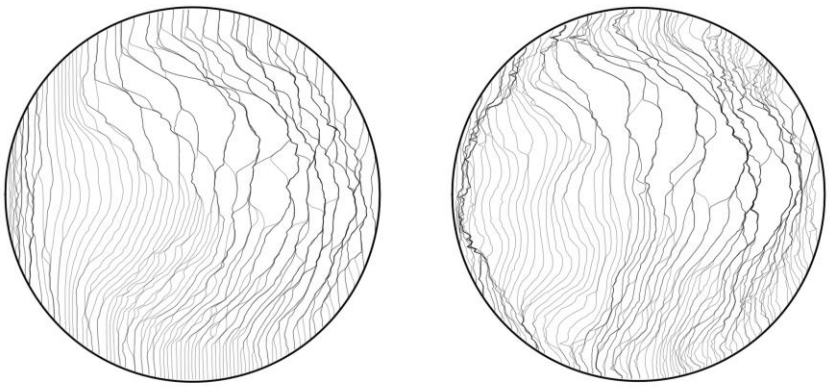

Fig. B7. Step development after 500 timestep ($\Delta t = 1000\ s$) under the time-averaged (without fluctuation) and the time-dependent (with fluctuation) boundary condition.

However, besides fluctuation, another feature of turbulence should also be involved into consideration, which is the enhancement of mass transport. The eddies change the transport mechanism from the molecular to convective even within the stagnant layer, and this transport is much faster than that by molecular collisions [11]. Due to the interaction of eddies of various sizes, the original molecular diffusion coefficient can be rectified as an effective diffusion coefficient [12]:

$$D_{eff} = D + D_{turb} \quad \text{(Eq. B-2 a)}$$

$$D_{turb} = \frac{\mu_{turb}}{0.9} \quad \text{(Eq. B-2 b)}$$

where μ_{turb} is the turbulent viscosity, the value of which can be obtained from the LES. The effective diffusion coefficient at the boundary layer surface is plotted in Fig. B8(a). Compared with the constant molecular diffusion coefficient, the effective diffusion coefficient is much larger, especially at the edge area of the crystal, where turbulence is stronger. Liu et al. have demonstrated in numerical simulation that a small ratio between

step kinetics coefficient (Kst) and solute diffusion coefficient (D) is preferable for a stable step development for solution growth of SiC [13]. Therefore, this turbulence-facilitated solute transport is expected to have an essential impact on the morphological stability on the growth front. The simulation of step development is again conducted with this enhanced diffusion coefficient, and the result exhibits more uniform step distribution on the entire crystal surface as well as less step bunching (Fig. B8(b)).

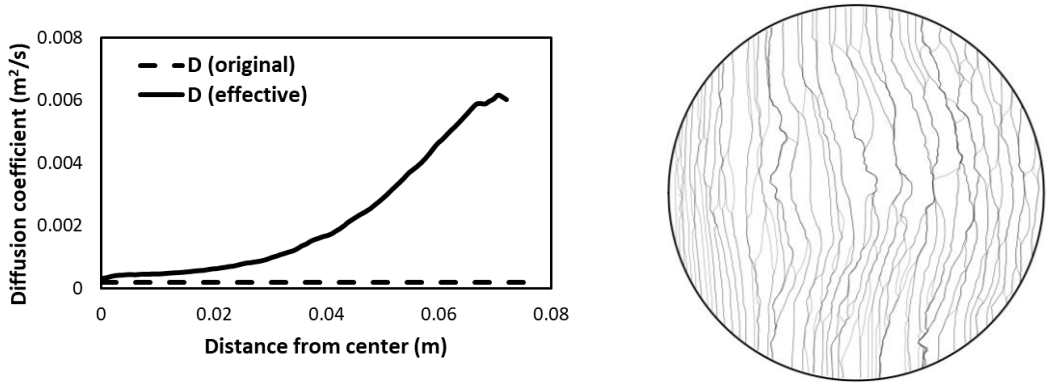

(a) (b)

Fig. B8. (a) Comparison of the original and effective diffusion coefficient; (b) Step morphology after 500 timesteps under the enhanced diffusion.

B.3 Discussion and conclusion

The above result can be explained that solution growth of SiC is a diffusion-limiting process, where a sufficient and fast carbon supply is necessary to eliminate the instability caused by steps interaction. Chernov et al. reported in solution growth of KDP crystal that an increasing turbulent flow rate, even in a parallel direction with step advancing, resulted in flatter and smoother height profile of the crystal surface, corresponding to less step bunching level [11]. These tendencies match well with that shown in Fig. B8(b).

Above all, a tentative conclusion regarding the effect of turbulence on solution growth of SiC can be made: the fluctuation of supersaturation leads to the occurrence of 3D nucleation particles and perturbation of step shape, while the enhanced diffusion enables more stable step development. Therefore, in practical growth experiment, a lower supersaturation value (to avoid frequent spontaneous nucleation and step zig-zag amplitude), and turbulence with sufficient intensity are recommended.

References

[1] C. Wu, Y. Li. *Sci. China Technol. Sci.* 2010, 53, 2477-2488.

[2] T. Yamamoto, Y. Okano, T. Ujihara, S. Dost. *J. Cryst. Growth* 2017, 470, 75-88.

[3] K. Kakimoto, B. Gao. *Handbook of Crystal Growth, second ed., Elsevier, Boston* 2015, 845-870.

[4] D. Vizman. *Handbook of Crystal Growth, second ed., Elsevier, Boston* 2015, 909-950.

[5] K. Kakimoto, A. Tashiro, T. Shinozaki, H. Ishii, Y. Hashimoto. *J. Cryst. Growth* 2002, 243, 55-65.

[6] J. Ding, L. Liu. *Int. J. Heat Mass Transf.* 2019, 142, 118463.

[7] A. Popescu, M. Bellmann, D. Vizman. CrystEngComm 2021, 23, 308-316.

[8] I.V. Markov. *Crystal Growth for Beginners: Fundamentals of Nucleation, Crystal Growth and Epitaxy, 3rd Edition, World Scientific, New Jersey* 2016.

[9] A.A. Chernov. *J. Cryst. Growth* 1992, 118, 333-347.

[10] N. A. Booth, A. A. Chernov, P.G. Vekilov. *J. Mater. Res.* 2002, 17, 2059-2065.

[11] A.A. Chernov. *J. Cryst. Growth* 2005, 275, 1-18.

[12] A.D. Smirnov, V.V. Kalaev. *J. Cryst. Growth* 2008, 310, 2970-2976.

[13] X. Liu, Y. Dang, K. Suzuki, C. Zhu, W. Yu, S. Harada, M. Tagawa, T. Ujihara. *J. Cryst. Growth* 2022, 578, 126425.

List of Publications

Journal Paper

1. **Y. Dang**, C. Zhu, M. Ikumi, M. Takaishi, W. Yu, W. Huang, X. Liu, K. Kutsukake, S. Harada, M. Tagawa, T. Ujihara. *"Adaptive process control for crystal growth using machine learning for high-speed prediction: application to SiC solution growth"*. CrystEngComm 2021, 23, 1982-1990.
2. **Y. Dang**, C. Zhu, X. Liu, W. Yu, X. Liu, K. Suzuki, T. Furusho, S. Harada, M. Tagawa, T. Ujihara. *"Numerical investigation of solute evaporation in crystal growth from solution: A case study of SiC growth by TSSG method"*. Journal of Crystal Growth 2022, 579, 126448.
3. **Y. Dang**, K. Kutsukake, X. Liu, Y. Inoue, X. Liu, S. Seki, C. Zhu, S. Harada, M. Tagawa, T. Ujihara. *"A transfer learning-based method for facilitating the prediction of unsteady crystal growth"*. Advanced Theory and Simulations 2022, 5, 2200204.
4. **Y. Dang**, X. Liu, C. Zhu, Y. Fukami, S. Ma, X. Liu, K. Kutsukake, S. Harada, T. Ujihara. *"Modeling of the macrostep morphology during long-term solution growth of SiC"*. (finished).
5. W. Yu, C. Zhu, Y. Tsunooka, W. Huang, **Y. Dang**, K. Kutsukake, S. Harada, M. Tagawa, T. Ujihara. *"Geometrical design of a crystal growth system guided by a machine learning algorithm"*. CrystEngComm 2021, 23, 2695-2702.
6. X. Liu, **Y. Dang**, K. Suzuki, C. Zhu, W. Yu, S. Harada, M. Tagawa, T. Ujihara. "*Solvent design aiming at solution property induced surface stability: A case study using SiC solution growth"*. Journal of Crystal Growth 2022, 578, 126425.
7. X. Liu, **Y. Dang**, H. Tanaka, Y. Fukuda, K. Kutsukake, T. Kojima, T. Ujihara, N. Usami. *"Data-driven optimization and experimental validation for the lab-scale mono-like silicon ingot growth by directional solidification"*. ACS Omega 2022, 7, 6665-6673.

Conference

1. **Y. Dang**, C. Zhu, W. Yu, W. Huang, M. Ikumi, S. Harada, M. Tagawa, T. Ujihara. The 81st Japanese Society of Applied Physics Autumn Meeting, 2020. (Oral presentation).
2. **Y. Dang**, C. Zhu, M. Ikumi, W. Yu, W. Huang, S. Harada, M. Tagawa, T. Ujihara. The 49th Japanese Conference of Crystal Growth (JCCG-49), 2020. (Oral presentation).
3. **Y. Dang**, C. Zhu, X. Liu, X. Liu, S. Harada, T. Ujihara. 2nd International Symposium on Modeling of Crystal Growth Processes and Devices (MCGPD-2021), 2021. (Oral presentation).

4. **Y. Dang**, C. Zhu, M. Ikumi, M. Takaishi, W. Yu, W. Huang, X. Liu, S. Harada, M. Tagawa, T. Ujihara. 13th European Conference on Silicon Carbide and Related Materials (ECSCRM-2021), 2021. (Poster presentation).

5. **Y. Dang**, X. Liu, C. Zhu, W. Yu, K. Suzuki, T. Furusho, S. Harada, M. Tagawa, T. Ujihara. The 50th Japanese Conference of Crystal Growth (JCCG-50), 2021. (Oral presentation).

6. **Y. Dang**, X. Liu, Y. Fukami, S. Ma, C. Zhu, S. Harada, T. Ujihara. 2022 Material Research Society Spring Meeting, 2022. (Oral Presentation).

7. **Y. Dang**, X. Liu, Y. Fukami, S. Ma, C. Zhu, S. Harada, T. Ujihara. 19th International Conference on Silicon Carbide and Related Materials (ICSCRM 2022), 2022. (Oral Presentation).

8. **Y. Dang**, X. Liu, Y. Fukami, S. Ma, C. Zhu, S. Harada, M. Tagawa, T. Ujihara. The 83rd Japanese Society of Applied Physics Autumn Meeting, 2020. (Oral presentation).

Award

1. 「講演奨励賞」 in the 49th Japanese Conference of Crystal Growth (JCCG-49), 2020.

2. “Best paper presentation award” in 2nd International Symposium on Modeling of Crystal Growth Processes and Devices, 2021.

Acknowledgement

We are living in a world with various instabilities: the pandemic showing no sign of termination after 2-year raging, the economic and even military conflicts between countries, the assassination of the former prime minister of a highly civilized country, etc. The PhD study under this circumstance should have been tough. However, there were a lot of people with whose help I was able to focus on only the instabilities in the solution growth of SiC.

First of all, I would like to express my great gratitude to my supervisor Prof. Toru Ujihara. Before being accepted as a PhD student in his lab, I declined another PhD position with a fair scholarship, but I never regret this decision. During my 3 years staying, I was always impressed by his erudition, kindness, and optimism. Under his supervising, I had great freedom to do whatever I am interested in and good at, and never needed to worry about making mistakes. Without his continuous encouragement and support, the research would never be this smooth and enjoyable. Besides research, he is also a role model in life, who always dares to jump outside the comfort zone and face the bigger challenge. I will never forget we drank in a small Japanese restaurant talking about dreams, which is a sweet memory.

I would also like to give my appreciation to associate professor Shunta Harada. Like an opposite side of Prof. Ujihara, he pointed out the shortcomings of my research and manuscripts, making me realize the gap between my work and masterpiece. His rigorous guidance and honest critique were the driven force for me to pursue the better.

Regarding completing this dissertation, I would like to give special thanks to assistant professor Can Zhu for his in-depth discussion and sharing the knowledge on crystal growth. Many parts of this dissertation were inspired by his ingenious experiment ideas. His precise attitude towards experiments cannot be learned from textbooks. The same thanks should also be given to assistant professor Xin Liu. He is an expert in crystal growth simulation. Every time I had new ideas regarding simulation, he was always the first one I went to for consulting. Moreover, the contribution of Dr. Xinbo Liu should not be overlooked. My academic background was not in material science, but he was always there willing to explain to me the complicated crystal growth theories. The idea of chapter 4, which is my favorite chapter, was inspired through daily discussion with him.

I am extremely grateful to Prof. Koichi Kakimoto, Prof. Yasunori Okano, Prof. Makoto Kobashi, and Prof. Noritaka Usami for being my review committee. Their valuable comments with no doubt helped to improve this dissertation.

I would also like to thank Dr. Kentaro Kutsukake, Dr. Tomoaki Furusho, Dr. Koki Suzuki, Dr. Wancheng Yu, and Mr. Yukihisa Takeuchi for sharing their knowledge and experience from various fields. Also, thank all my colleagues, especially Mr. Peiyang Cai, Miss Huiqin Zhou, Mr. Shuyang Ma, Mr. Yoshiki Inoue, Mr. Yuma Fukami, Mr. Motoki Ikumi, and Dr. Fumihiro Fujie, for their insightful discussion and daily companionship. Particular thanks should be given to Miss Hinako Funo, Miss Uka Iwashima, and Miss Tomoko Shoji. Their kind help made everything easier.

My PhD study and life were financially supported by Epson International Scholarship Foundation, Institute of Materials and Systems for Sustainability, Interdisciplinary Frontier Next-Generation Researcher Program of the Tokai Higher Education and Research System, and Leadership Development Program for Space Exploration and Research.

Finally, I would like to thank Lidong Zhang for 3 years accompanying. You make me able to see the world from a more comprehensive perspective. I am a person who keeps worrying about the uncertainty in life, but you always ease my anxiety with your special wisdom and optimism.

I have no idea how to appreciate and pay back my parents, who raised me and made me who I am. Every tiny achievement I make is inseparable from their support and encouragement. I am forever indebted to them and will step forward with their wishes and infinite love.